



**Petrology and Geochronology of Cordierite Bearing Gneisses  
from the Wannu-/Highland Complex Boundary, Sri Lanka**

**Master Thesis  
by  
Nikolaus Lechner**

Thesis Submitted in Partial Fulfillment of the Requirements for the Degree of  
Master of Science

Supervisor

Univ.-Prof.Mag Dr.rer.nat. Christoph A. Hauzenberger

Institute for Earth Sciences Graz, May 2020

---

## **Acknowledgement**

First, I want to personally thank my supervisor, Prof. Dr. Christoph A. Hauzenberger for his support, guidance and advice through this thesis. Special thanks go to Dominik Sorger who supported me with professional advice and helped me handling the microprobe whenever he could. Furthermore, I would like to thank Prof. Dr. Rohan Fernando for guiding us through the wilderness of Sri Lanka, Prof. Dr. Kurt Stüwe who always had time to solve a problem with me, John Booth without who collecting samples would have been half as much fun and successful, Anton Pock without who I would still work on thin sections and of course Marcel Masten who accompanied me during my studies from the beginning on as a colleague and friend.

---

## Abstract

The Sri Lankan basement is subdivided into the Highland Complex (HC), Wannai Complex (WC) and Vijayan Complex (VC) mainly based on Nd-model ages from Milisenda et al. (1988, 1994) and underwent amphibolite to granulite facies metamorphism during the Pan-African orogeny ~ 600 - 500 Ma ago. While the boundary between VC and HC is well known due to differences in metamorphic grade and a thrust/shear contact, the boundary between the WC and HC is still matter of discussion. The HC probably represents a deeper crustal level than the WC which is overprinted by up to UHT conditions in the central HC (Sajeev et al., 2010). Parts of the WC/HC boundary area may have also experienced UHT conditions but clear evidence is still missing. For this study cordierite bearing garnet-biotite gneisses were collected from the WC/HC boundary area from south-western Sri Lanka. This rock type occurs less frequent compared to the dominant meta-granitoides, garnet-sillimanite gneisses, charnockitic gneisses and basic granulites/amphibolites and are regarded as an own unit. Symplectitic cordierite and biotite growth around garnet indicates decompression by the reaction  $\text{Melt} + \text{Grt} + \text{Qtz} + \text{Sil} = \text{Crd} + \text{Sp} + \text{Bt}$ . Previous in-situ monazite dating was recently performed in this area e.g. by Wanniarachchi & Akasaka (2016), documenting 4 age groups, 1788 – 1766 Ma, 676 - 559 Ma, 533-507 Ma and 481 - 434 Ma. However, age data for this rock type are rare in southwestern Sri Lanka and more age data are needed in combination with petrological data to unravel the metamorphic evolution of this unit. Based on mineral assemblages, textures and EPMA mineral analyses, P-T conditions of  $850 \pm 50$  °C and  $6 \pm 1$  kbar are proposed during metamorphism of the cordierite bearing unit. In-situ EPMA Th-U-Pb monazite dating was done based on textural arguments: (1) monazite inclusions in garnet yield a weighted mean age of  $572 \pm 2$  Ma, which is interpreted to represent the age of main metamorphism in the HC, which was documented by Sajeev et al. (2010) with a similar result of  $569 \pm 5$  Ma. He found a metamorphic overprint at approximately 550 Ma (zircon rims:  $551 \pm 7$  Ma, monazite rims:  $547 \pm 7$  Ma) which is probably also present here, but not well constrained. (2) Monazites in the matrix cluster around  $565 \pm 3$  Ma and  $534 \pm 2$  Ma age. The older age is close to the age found in monazites enclosed in garnet and thus represent the age of

---

metamorphism in the HC, while the younger age represents the timing of cordierite formation and the LP/HT metamorphic event seen in southwestern Sri Lanka.

---

## Zusammenfassung

Das proterozoische Basement von Sri Lanka ist, basierend auf Nd - Modellalter von Milisenda et al. (1988, 1994) in den Highland Complex (HC), den Wannii Complex (WC) und den Vijayan Complex (VC) unterteilt, und erlebten während der panafrikanischen Orogenese vor ~ 600 - 500 Ma eine amphibolit- bis granulitfazielle Metamorphose. Während die Grenze zwischen dem VC und dem HC aufgrund von Unterschieden im metamorphen Grad und einem sichtbaren Scherkontakt bekannt ist, ist die Grenze zwischen WC und HC immer noch umstritten. Der HC stellt wahrscheinlich ein tieferes Krustensegment dar als der WC, welches durch bis zu UHT- (Ultra-hoch-Temperatur) Bedingungen im zentralen HC metamorph überprägt wurde (Sajeev et al., 2010). Der Grenzbereich zwischen WC und HC erlebte möglicherweise auch eine Metamorphose mit UHT Bedingungen, jedoch fehlen dafür eindeutige Beweise. Für diese Studie wurden Proben von Cordierit führende Granat-Biotit-Gneise aus dem WC / HC-Grenzgebiet im Südwesten Sri Lankas gesammelt. Dieser Gesteinstyp kommt im Vergleich zu den vorherrschenden Metagranitoiden, Granat-Sillimanit-Gneisen, charnockitischen Gneisen und basischen Granuliten / Amphiboliten seltener vor und wird als eigene Einheit angesehen. Symplektitisches Cordierit- und Biotitwachstum um Granat weist auf eine Dekompression durch die Reaktion Schmelze + Grt + Qtz + Sil = Crd + Sp + Bt hin. Frühere In-situ-Monazit-Datierungen wurden in diesem Bereich kürzlich von Wanniarachchi & Akasaka (2016) durchgeführt, welche 4 Altersgruppen, 1788 - 1766 Ma, 676 - 559 Ma, 533 - 507 Ma und 481 - 434 Ma dokumentieren. Es gibt nur wenige Altersdaten für diesen Gesteinstyp im Südwesten von Sri Lanka und um mehr über die metamorphe Entwicklung dieser Einheit zu verstehen sind mehr petrologische und geochronologische Daten nötig. Basierend auf Mineralparagenese, Texturen und EPMA-Mineralanalysen werden P-T-Bedingungen von  $850 \pm 50$  ° C und  $6 \pm 1$  kbar für die Metamorphose der Cordierit führenden Gneisen vorgeschlagen. In-situ EPMA Th-U-Pb Monazitdatierung wurde basierend auf den textuellen Gegebenheiten durchgeführt: (1) Monaziteinschlüsse in Granat ergeben ein Alter von  $572 \pm 2$  Ma (gewichtetes Mittel), welches mit dem Alter der Hauptphase des Metamorphismus im HC von Sajeev et al., (2010) korreliert ( $569 \pm 5$  Ma). Die von Sajeev et al., (2010) als

---

metamorphe Überprägung interpretierte Zirkon und Monazittränder mit einem Alter von  $551 \pm 7$  Ma und  $547 \pm 7$  Ma weisen auf weitere metamorphe Ereignisse hin, welche jedoch in den Daten dieser Studie nicht auseinandergelöst werden konnten. (2) Monazite in der Matrix weisen zwei Altersgruppen auf:  $565 \pm 3$  Ma und  $534 \pm 2$  Ma. Während die ältere Gruppe dem Alter der Monazite in Granaten sehr ähnlich ist und somit das Alter der Metamorphose des HC repräsentiert, steht die jüngere Gruppe für ein jüngeres, Cordierit-bildendes niedrig Druck/hoch Temperatur Ereignis im Südwesten Sri Lankas.

---

## Content

Acknowledgement.....	ii
Abstract.....	iii
1. Introduction .....	9
1.1 Geological Overview .....	9
1.1.1 Wanni Complex.....	12
1.1.2 Highland Complex.....	12
1.1.3 Vijayan Complex .....	13
1.1.4 Kadugannawa Complex .....	14
1.2 Gondwana Linkage .....	14
1.3 Field Relations and Data Acquisition.....	16
1.4 Local Geology.....	16
2. Methods .....	22
3. Petrography .....	23
4. Whole Rock Chemistry .....	27
5. Mineral chemistry.....	34
5.1 Garnet.....	34
5.2 Biotite.....	44
5.3 Feldspar.....	47
5.3.1 Plagioclase.....	47
5.3.2 K-feldspar.....	47
5.3.3 Feldspar exsolutions .....	49
5.4 Cordierite .....	51
5.5 Oxides .....	53
5.6 Orthopyroxene .....	55
6. Th-U-Pb Monazite Dating.....	56
6.1 Introduction.....	56
6.2 Method.....	59
6.3 Chemical Composition of Monazite .....	60
6.4 Monazite Texture .....	69

---

6.5	Description of Monazite Bearing Samples.....	75
6.5.1	Sample S4 .....	75
6.5.2	Sample S5 .....	76
6.5.3	Sample S21 .....	77
6.5.4	Sample S23 .....	78
6.5.5	Sample S41 .....	78
6.5.6	Sample SL8 .....	79
6.6	Age Results .....	80
7.	Estimates by Conventional Thermobarometry .....	83
7.1	Metamorphic Evolution .....	83
7.2	Garnet-Cordierite Thermometer .....	83
7.3	Two Feldspar Thermometry .....	84
7.4	Ti in Biotite Thermometer.....	84
7.5	GASP Barometer .....	84
7.6	Multi Equilibrium Thermobarometry .....	85
8.	P-T Pseudosection Modelling .....	86
8.1	Introduction.....	86
8.2	P-T Pseudosections.....	88
8.2.1	Sample S4 .....	88
8.2.2	Sample S5 .....	90
8.2.3	Sample S23 .....	92
8.2.4	Sample SL8 .....	94
9.	Discussion.....	96
10.	References .....	98

# 1. Introduction

## 1.1 Geological Overview

Sri Lanka represents a former part of the Late-Neoproterozoic Gondwana supercontinent and was located in the center of the Africa-India-Madagascar and East-Antarctica collage in the eastern part of the supercontinent providing therefore important insights into Precambrian evolution and growth of continental crust (Santosh et al., 2014). The high-grade metamorphic Precambrian basement of Sri Lanka is subdivided into three (four) major units, primarily based on Nd-model ages but also on U-Pb Zircon ages and structural interpretations (Figure 1): The Highland Complex (HC) in central Sri Lanka, the Wannai Complex (WC) in the west and northwest and the Vijayan Complex (VC) in the east and southeastern part of the island (Kröner et al. 1987; Milisenda et al. 1994; Kehelpannala 2003; Osanai et al. 2006). The fourth, the Kadugannawa Complex (KC), is postulated as a separate unit by some authors e.g. (Cooray, 1994) but is discussed to be part of the WC by later authors e.g. (Kröner et al., 2013). The northwestern part of Sri Lanka is covered by Miocene to Quaternary sediments.

(Liew et al., 1994; Milisenda et al., 1988) recognized three provinces with different Nd-model ages: Samples from the central granulite belt of the HC yield ages from 2.2 - 3.4 Ga, hornblende-biotite gneisses of the VC yield ages between 1.0 and 1.8 Ga and ages from amphibolite to granulite grade metapelites and charnockitic gneisses from the WC range from 1.1 to 2.0 Ga. The KC, considered as being part of the WC is interpreted as a layered intrusion within the WC and shows similar geochronological data. U-Pb ages from detrital Zircons dated by (Hözl et al., 1994) are consistent with the Nd-model ages and confirms their liability which was doubted by several Authors. Burton and O'Nions (1990) for example argued that high grade metamorphism fractionates Sm-Nd isotopes and therefore questioned the eligibility of this method. Kleinschrodt et al., (1991) argued that the related field data are not sufficient and regarded the WC and HC as one complex. Nd and U-Pb age data on the other hand confirm an age contrast between the HC and the WC (and VC) (Hözl et al., 1994). Furthermore, Pb isotopic data show

a significant difference between the WC and HC, supporting the theory of a separated pre-metamorphic history (Liew et al., 1994). While the boundary between the VC and the HC is well defined by a thrust/shear contact and correlates with the mapped ages (Kröner et al., 1994), the boundary between the HC and the WC is still matter of discussion. The HC is considered to represent a deeper crustal level than the WC although there is no clear structural break and the contact has been overprinted by a long lasting metamorphic event (Kleinschrodt, 1994). Yielding new geochronological and P-T data in the southeastern part of the suggested boundary area is part of this thesis and is meant to help confine the area of the assumed boundary. In addition, new precise U-Th-Pb data from monazite aims to solve the question if this boundary area has experienced a polymetamorphic evolution.

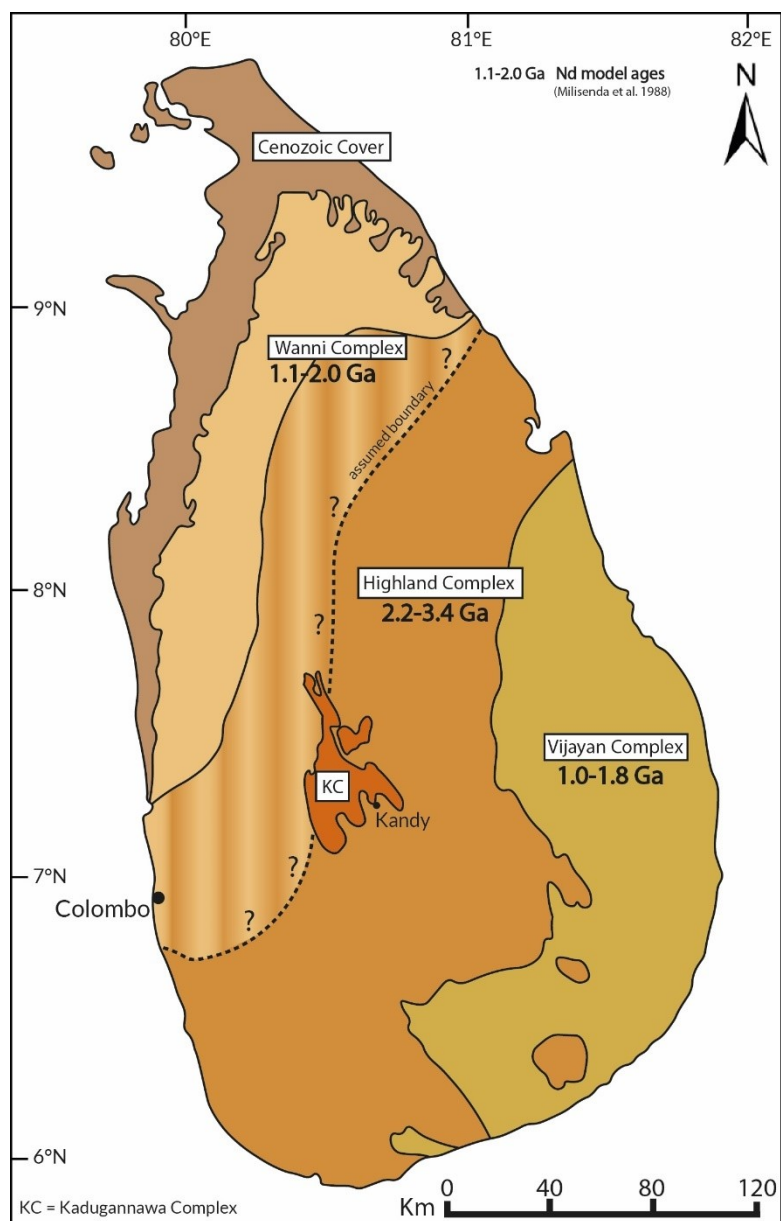


Figure 1: Simplified geological overview of Sri Lanka showing the four basement complexes Wannai Complex, Highland Complex, Vijayan Complex, Kadugannawa Complex and Cenozoic cover sediments. Striped area and question marks mark the inferred boundary area between the Highland and Wannai Complex. Map after Cooray (1994).

### 1.1.1 *Wanni Complex*

The Wanni Complex (WC) consists mainly of upper amphibolite to granulite facies meta-igneous rocks which show a widely varied range of photoliths: granites, granodiorites, monzonites, tonalities, charnockitic gneisses and enderbitic gneisses. The less frequent metasedimentary rocks are garnet-sillimanite gneisses, cordierite gneisses, quartzites and calc-silicates and occur in the eastern and southeastern part, near to the inferred boundary to the Highland complex (Cooray, 1994; Mathavan et al., 1999). Santosh et al. (2014) classified the meta-igneous rocks as volcanic-arc related, formed by intermediate to felsic arc and mafic subduction related magmatism using trace element, rare-earth-element (REE) patterns and discrimination diagrams. Peak metamorphic conditions for the WC are estimated at around 700-830 °C and 5 - 7 kbar (Raase et al., 1994). The emplacement age of local granitoid intrusives in the WC falls between 770-1100 Ma (Kroner et al., 1993; N. Baur et al., 1991). Un-metamorphosed carbonatites with up to 1m large apatite crystals are found in the northern-central part. The charnockitic body emplacement (primary zircon crystallization ages by Kröner et al. (1992) is dated at 1 Ga, followed by a thermal event at 570 Ma related to the Pan-African orogeny (He et al., 2016). Hölzl et al., (1994) suggested a timeframe for the granulite facies metamorphic event between ~590 and ~540 Ma. This is based on a monazite U-Pb age of 541 Ma and U-Pb zircon lower intercept ages of  $592 \pm 146$  Ma and ~560 Ma for metapelites and granites, respectively. The exact date of the granulite metamorphosis can vary for different localities but they all took place within the period of the Pan-African orogeny (~610 -500 Ma) (Kröner et al., 1993; Baur et al., 1991).

### 1.1.2 *Highland Complex*

The Highland Complex (HC) is the most investigated complex due its preservation of ultra-high-temperature (UHT) rocks and associated mineral assemblages, including sapphirine (Dharmapriya et al., 2015; Kelsey et al., 2004; Sajeew et al., 2004). It shows a vast diversity of lithologies represented by predominantly metasedimentary and meta-igneous granulite facies rocks including quartzites,

marbles, calcsilicates, pelitic gneisses, charnockitic gneisses and orthogneisses (Cooray, 1994; Mathavan et al., 1999; Santosh et al., 2014; Braun & Kriegsman, 2003). Regional granulite facies metamorphism affected the whole 2 - 3.4 Ga old complex 610 - 550 Ma ago during the Pan-African orogeny locally to ultra-high temperature conditions up to 900 - 1150°C and 9 - 12.5 kbar in the central HC (Osanai et al., 2006; Sajeev & Osanai, 2004; Sajeev et al., 2007). The UHT event was dated precisely by Sajeev et al., (2010) using U-Pb zircon ages at  $569 \pm 5$  Ma with a following post peak isothermal decompression at  $551 \pm 7$  Ma. This interpretation of two generations of metamorphic zircon growth at the respective older and younger event is based on different Th/U ratios.

However, a vast part of the HC underwent metamorphism from 700 – 750 °C and 4.5 - 6 kbar in the southwestern part to 800 - 900 °C and 8 - 10 kbar in the central part of the HC, defining a P-T gradient (Kriegsman, 1994, 1995; Malaviarachchi et al., 2011; Raase et al., 1994) . A clockwise P-T path includes a phase of isobaric cooling after peak metamorphic conditions, recorded in metapelites, calcsilicates and intermediate to mafic granulites followed by decompression (Raase & Schenk, 1994; Mathavan et al., 1999; Dharmapriya et al., 2015). The chemical variety of the meta-igneous rocks ranges from granitic, granodioritic, monzonitic, tonalitic, charnockitic to enderbitic composition (Pohl & Emmermann, 1991).

### 1.1.3 *Vijayan Complex*

The Vijayan Complex (VC) consists mainly of upper amphibolite grade meta-igneous rocks including calc-alkaline granitoid gneisses, augen-gneisses and some amphibolites related to mafic dykes (Pohl, J. R., & Emmermann, 1991). Protolith emplacement was dated on magmatic zircons at 1100 – 1000 Ma (Hölzl et al., 1994; Kröner et al., 2013). The hornblend-biotite bearing gneisses, considered as meta-granitoids show predominantly granodioritic and granitic but also dioritic and leucogranitic compositions. Granulite grade metamorphism was reported by (Kröner et al., 2013; Petschnig, 2015) and affected the VC more extensive than previously thought. Based on U-Pb zircon ages, metamorphism occurred probably between 591 Ma and 456 Ma and is therein similar to the HC and WC (Kröner et al., 1987; Hölzl et al., 1994). P-T conditions for the VC are less

constrained than in the HC due to missing suitable mineral assemblages for P-T calculations. Based on field investigations and thin-section studies Petschnig, (2015) postulates that most parts of the VC underwent granulite facies metamorphism followed by partly retrogression to amphibolite facies. Peak P-T conditions obtained by classical geothermobarometry, feldspar thermometry and P-T modelling using PerpleX of several unique samples from different parts of the Vijayan Complex give up to 900 – 930 °C and 8.4 - 8.9 kbar.

#### 1.1.4 *Kadugannawa Complex*

The Kadugannawa Complex (KC), often named 'Arenas', is basically a double plunging synform in and around Kandy and consists of upper-amphibolite to granulite facies rocks (Cooray, 1994; Kroner et al., 1993). Based on the Nd-model ages, the KC is considered to be part of the WC (Kröner et al., 2003; Kehelpannala, 1997). In contrast, recent studies suggest that the KC is representative for a Neoproterozoic disrupted arc magma chamber at the eastern part of the WC and related to the Lützow-Holm-Complex in east Antarctica (He et al., 2016; Santosh et al., 2014)

## 1.2 **Gondwana Linkage**

Within eastern Gondwana (Figure 2), Sri Lanka was located at a triple junction of three orogenic belts, the Irumide Belt, the Mozambique Belt and the Lützow-Rayner Belt, all formed during the Pan-African orogeny (~600-500 Ma). Isotopic ratios and REE patterns of granitic gneisses, mafic rocks and serpentinites show typical characteristics for an subduction related arc setting, which is consistent with the concept that the Pan-African orogeny is a result of the closure of a late Proterozoic ocean and the assembly of a number of different continental blocks and terranes (He et al., 2016; Kriegsman, 1995; Collins et al., 2005; Fritz et al., 2013). This leads to the conclusion, along with geochronological data, that the Mesoproterozoic VC (1.0-1.8 Ga) and the Paleoproterozoic to Mesoproterozoic

WC (1.1-2.0 Ma) formed separately and collided with the older Archean to Paleoproterozoic HC during the late Neoproterozoic- Cambrian (Pan-African Orogeny) (Santosh et al., 2014).

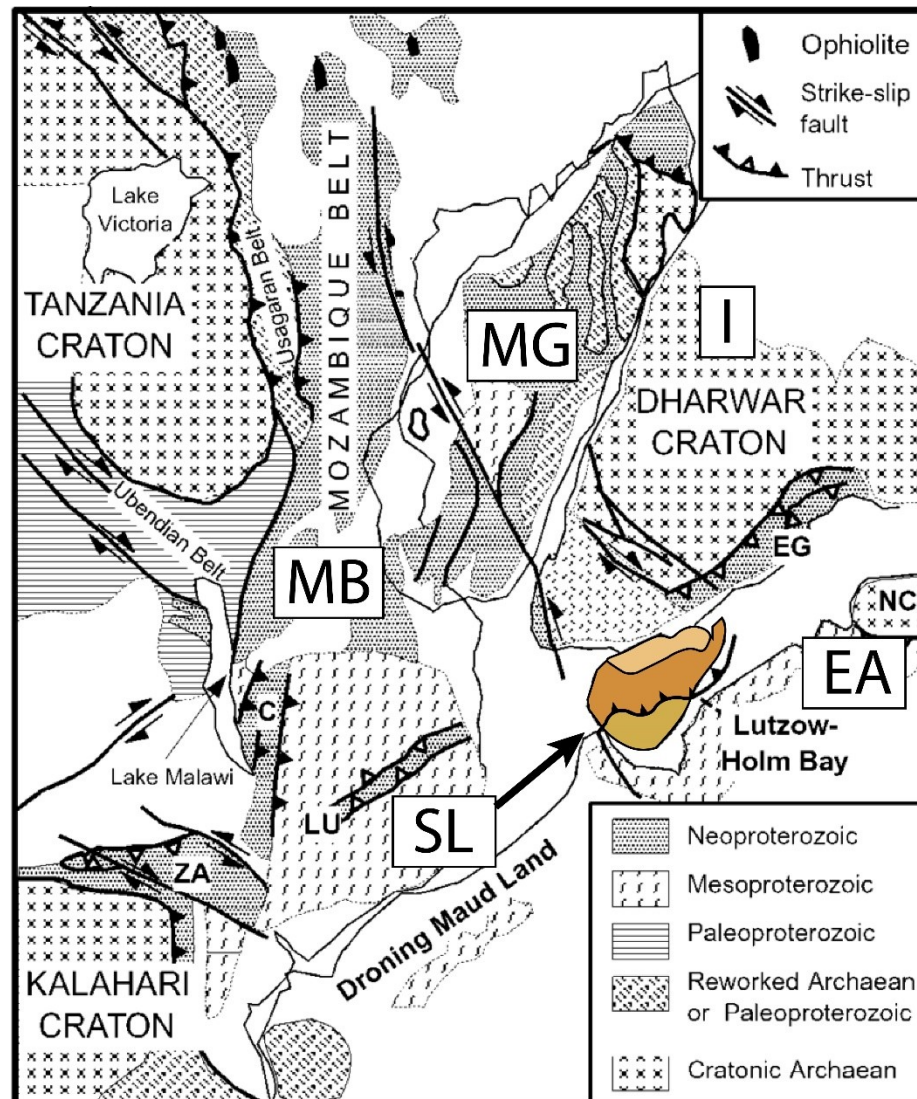


Figure 4: Reconstructed map of eastern Gondwana and former relation between Sri Lanka (SL), India (I), East-Antarctica (EA) Madagascar (MG) and the Mozambique-Belt (MB). Colored areas in Sri Lanka as in Figure 1 from north to south: Wannu Complex, Highland Complex and Vijayan Complex with the thrust/shear contact at the Highland Complex – Vijayan Complex boundary. Map after Hauzenberger et al., (2007).

### 1.3 Field Relations and Data Acquisition

Over 180 samples were collected during a field trip in 2018 from the Highland and Wannu Complexes, Sri Lanka and almost 200 samples by Paul Petschnig and Christoph A. Hauzenberger in 2015. After careful examination of thin sections with optical microscope and additional mineral analyses obtained by electron probe microanalyzer (EPMA), 32 turned out to contain cordierite from which 20 are from 2018 and 12 from 2015 (Table 1). The majority of samples was taken at quarries due to dense vegetation in central or flat areas overlain by thick weathered soils in northern Sri Lanka and along some roadsides. Sample locations are shown in Figure 6.

### 1.4 Local Geology

The cordierite bearing garnet-biotite gneisses investigated in this study occur as intercalated layers between the dominating felsic to intermediate orthogneisses, banded orthogneisses and minor charnockitic bodies (Figure 3 A). Migmatitic textures are found at a meter (Figure 4 A, B) to centimeter scale (Figure 4 B) throughout the whole WC, with plagioclase, k-feldspar and quartz rich leucosomes and biotite rich melanosomes. As shown in Figure 5 A, B and Figure 3 D, cordierite occurs in blueish layers along with garnet and biotite in undeformed and deformed gneisses, adjacent to feldspar rich layers. Less abundant cordierite is found in felsic graphite bearing garnet-sillimanite gneisses locally called “khondalites” (Figure 3 C) or large garnet bearing granulites from the southwestern WC, near Colombo. Although structural data are incomplete, acquired structural data match with the east dipping trend observed in western and southwestern Sri Lanka (Braun et al., 2003).

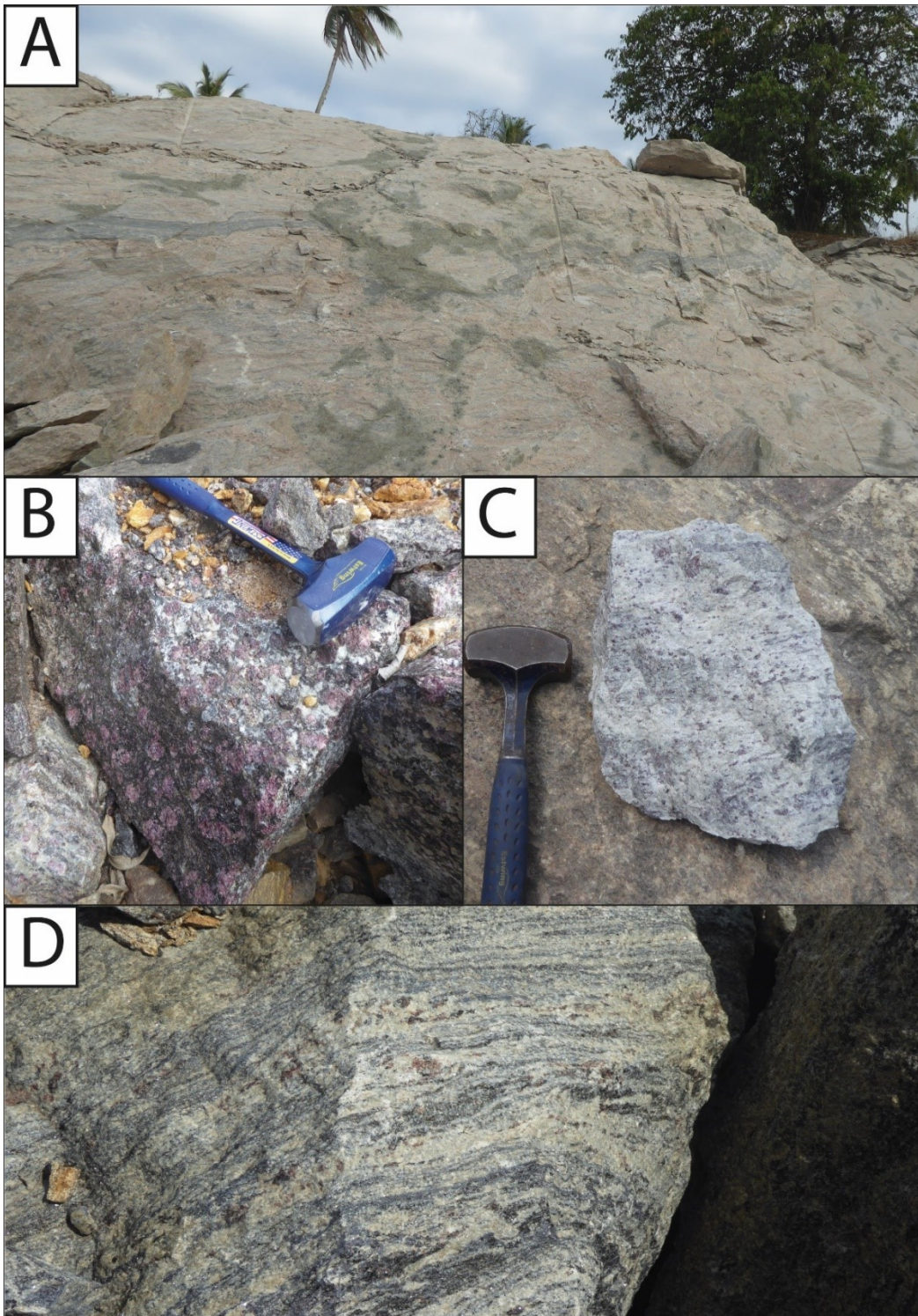


Figure 7: Pictures of outcrops and hand specimen from the Wannu-Complex. A.) Charnockitic gneiss body with “arrested” charnockites (dark patches) which probably formed through interactions with fluids. B.) cordierite bearing granulite with large garnet porphyroblasts. C.) garnet-cordierite-sillimanite gneiss with occasional small amounts of graphite (“Khondalite”). D.) typical banded garnet-cordierite gneiss, the bluish-gray layers contain cordierite along with garnet.

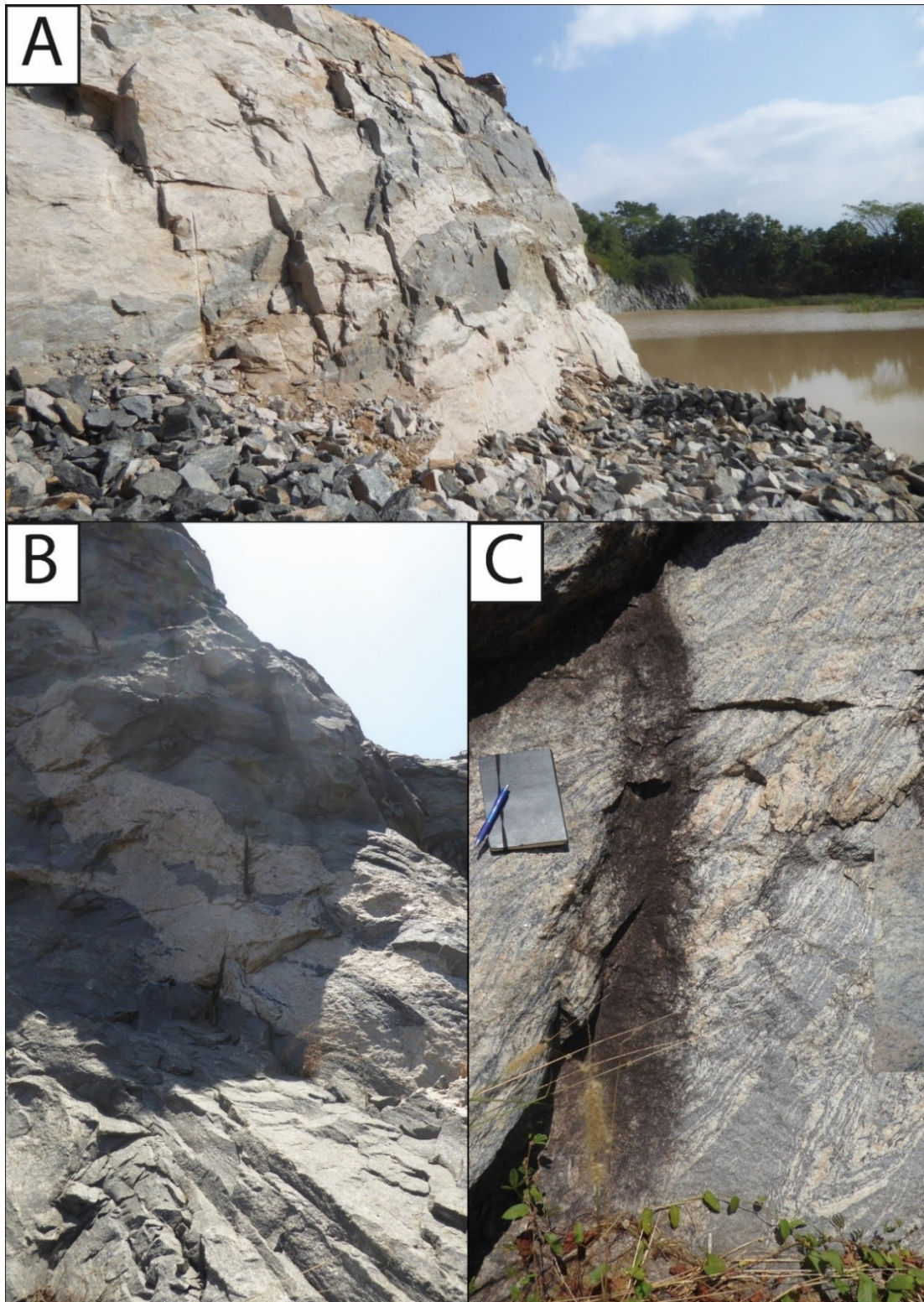


Figure 8: A.) Meter scale Banded migmatitic cordierite gneiss with only minor amounts of garnet. Dark melanosomes contain abundant cordierite and biotite. B.) predominantly mafic migmatitic gneiss with large meter-scale leucosomes. C.) Cm-scale banded and deformed migmatitic cordierite bearing gneiss.

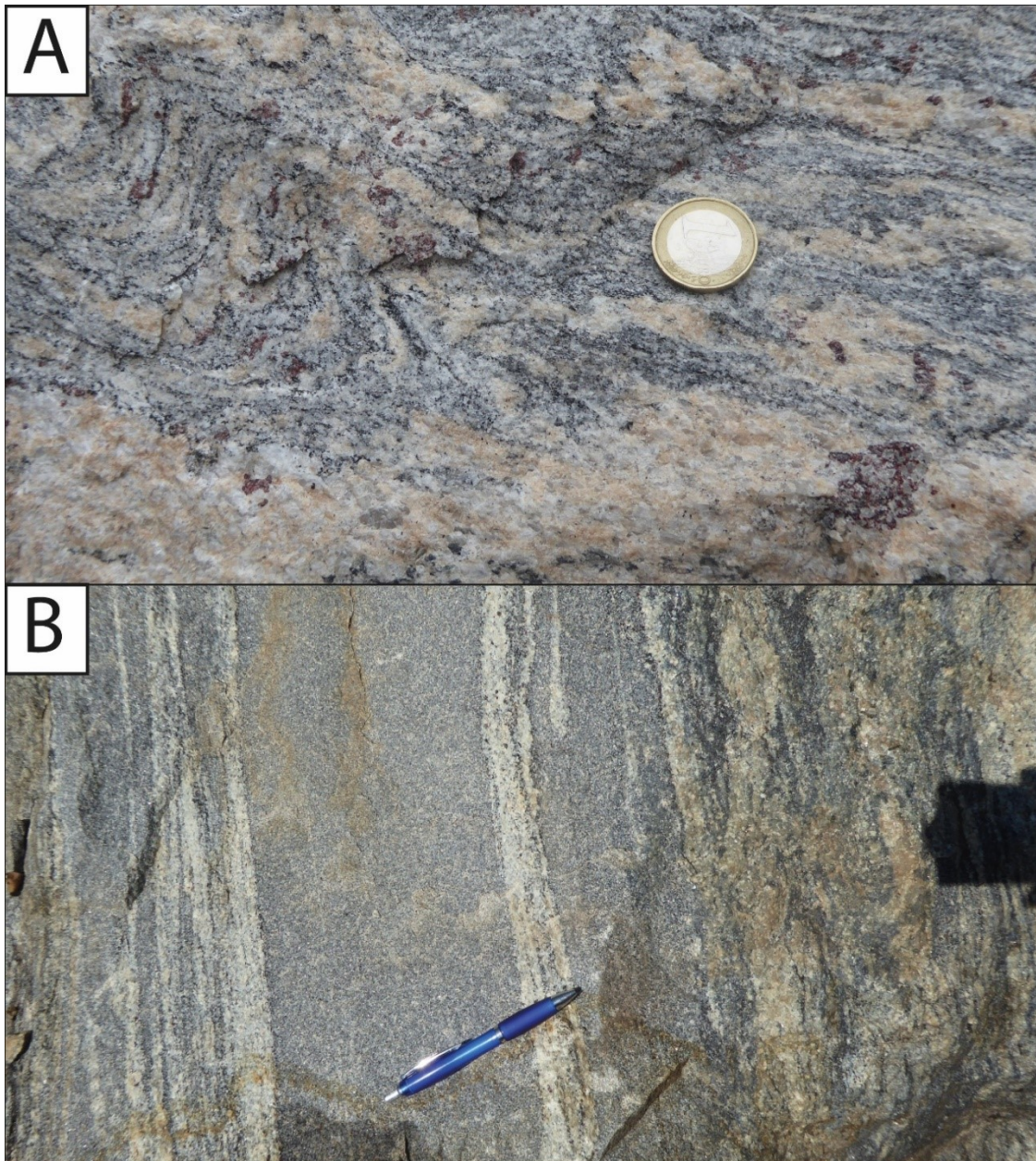


Figure 9. A.) Close pictures of a banded and deformed garnet-cordierite gneiss. Cordierite occurs in the blush layers, the bright layers consist mainly of plagioclase, k-feldspar and quartz. B.) On the left side a fine grained cordierite gneiss with gradually increasing grain size, deformation and increasing presence of small garnet towards the right side.

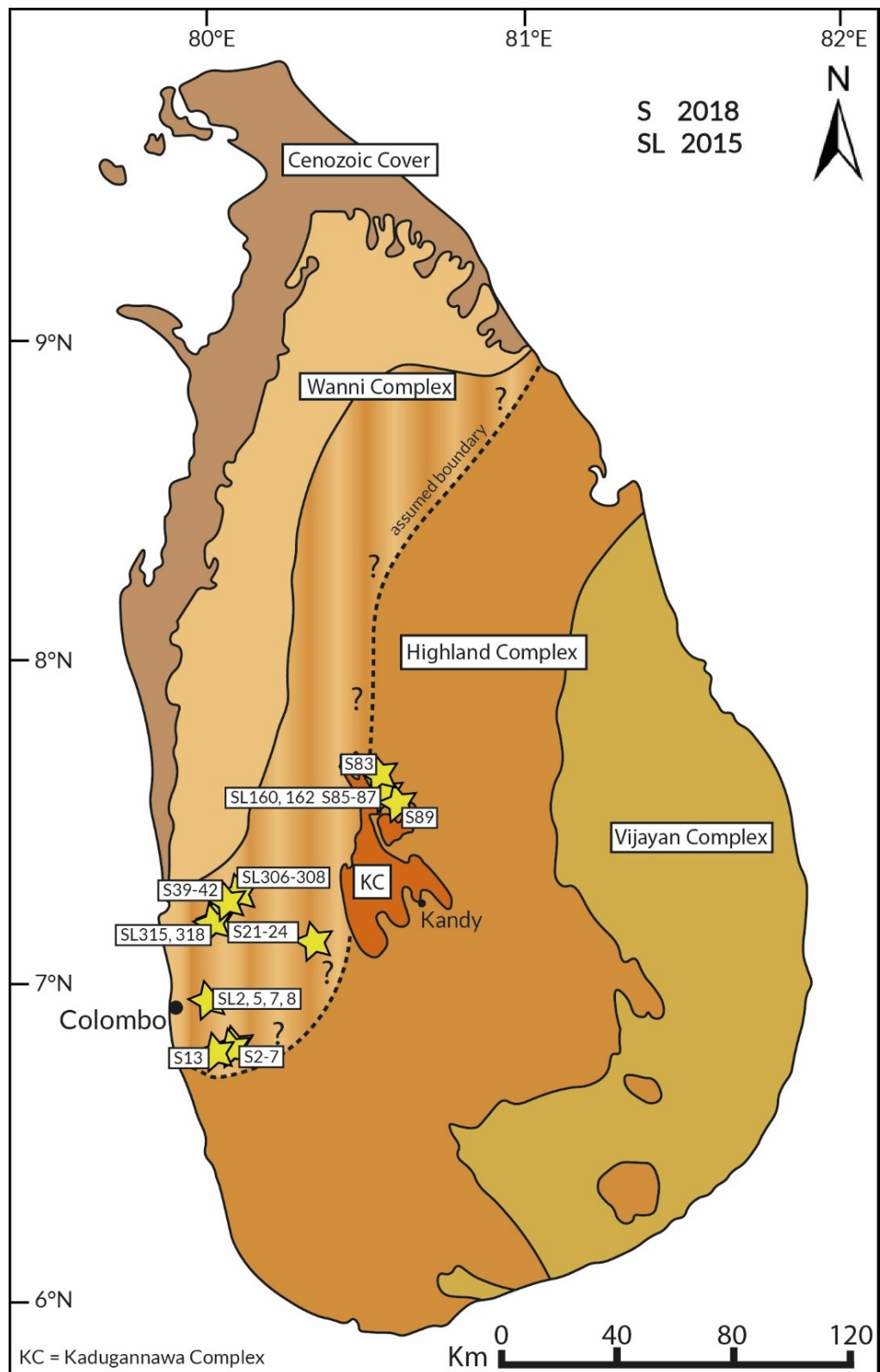


Figure 12. Sample locations, marked by yellow stars and their respective sample names. Map after Cooray (1994).

Table 2: List of all cordierite bearing samples including location, lithology and GPS data.

Sample	Lithology	°N	°E
S2	Grt-Bt migmatite	6.819100	80.060233
S3	Grt-Bt-Crd migmatite	6.819100	80.060233
S4	Leucosome	6.819100	80.060233
S5	Grt-Bt-Crd migmatite	6.819100	80.060233
S6	Grt-Bt-Crd migmatite	6.819100	80.060233
S7	Grt-Bt-Crd migmatite	6.819100	80.060233
S13	Bt-Crd migmatite	6.813967	79.998183
S21	Grt-Bt-Crd migmatite	7.250533	80.046917
S22	Grt-Bt-Crd migmatite	7.250533	80.046917
S23	Grt-Bt-Crd migmatite	7.250533	80.046917
S24	Grt-Bt-Crd migmatite	7.250533	80.046917
S39	Bt-Crd migmatite	7.295783	80.082600
S40	Grt-Bt-Crd migmatite	7.295783	80.082600
S41	Grt-Bt-Crd migmatite	7.295783	80.082600
S42	Grt-Bt-Crd migmatite	7.295783	80.082600
S83	Bt-Crd migmatite	7.564050	80.570083
S85	Bt-Crd migmatite	7.556717	80.603550
S86	Bt-Crd migmatite	7.556717	80.603550
S87	Bt-Crd migmatite	7.556717	80.603550
S89	Bt-Crd migmatite	7.551717	80.616467
SL2	Bt-Crd migmatite	6.951950	79.963950
SL5	Bt-Crd migmatite	6.951950	79.963950
SL7	Leucosome	6.951950	79.963950
SL8	Grt-Bt-Crd migmatite	6.951950	79.963950
SL29	Grt-Bt-Crd migmatite	7.115567	80.309150
SL160	felsic granulite	7.556650	80.603400
SL162	Bt-Crd migmatite	7.556650	80.603400
SL306	Grt-Bt-Crd migmatite	7.305183	80.101817
SL307	Grt-Bt-Crd migmatite	7.305183	80.101817
SL308	charnockitic gneiss	7.305183	80.101817
SL315	Bt-Crd migmatite	7.250533	80.047500
SL318	Leucosome	7.250533	80.047500

## 2. Methods

Mineral chemistry was determined using a JEOL JXA-8530FPlus HyperProbe Electron Probe Microanalyzer (EPMA) at the Department of Petrology and Geochemistry, NAWI Graz Geocenter (University of Graz) equipped with an energy-dispersive (ED) and five wavelength-dispersive (WD) spectrometers. Polished thin sections (30-40µm thickness) were coated with carbon. Beam settings were 15kV acceleration voltage and 10nA probe current. Beam diameter was 1µm for garnet, orthopyroxene ilmenite and magnetite/spinel, 2 µm for k-feldspar, 3 µm for plagioclase and cordierite and 4 µm for biotite. EDX was used for phase determination only, all quantitative analyses were conducted with WD spectrometers. Following standards were used: Diopside NMNH117733 (Jarosewich et al., 1980), garnet NMNH87375 (Jarosewich et al., 1980), fluorapatite NMNH104021 (Young et al., 1969), plagioclase NMNH115900 (Steward et al., 1966), gahnite NMNH145883 (Jarosewich et al., 1980), Ilmenite NMNH96189 (Jarosewich et al., 1980) and chromite NMNH117075 (Jarosewich et al., 1980).

Element distribution mappings for garnet (Mg, Fe, Ca, Mn, Y, P) and ilmenite (Fe, Ti, Mn) were generated with 15 kV acceleration voltage, 60ms dwell time and 200nA probe current with a beam diameter of 1 µm.

Whole rock compositions were determined using X-Ray Fluorescence. A representative amount of sample (>50 g) was crushed and grinded to fine powder using a swing mill made of tungsten carbide. All samples were dried for at least 10h at ~105 °C. Loss on ignition (LOI) was determined by heating ~1 g of sample in a ceramic beaker at ~1030° for 1h followed by cooling at room temperature (~20 °C) for 1h in an exsiccator. 7 g Lithium-tetraborate (Li<sub>2</sub>B<sub>4</sub>O<sub>8</sub>) and 1 g of sample were mixed (with an average deviation of 0.0001g) to generate a glass bead at ~1300 °C. Analyses were conducted with a Bruker Pioneer S4 WDXRF at the NAWI Graz Geocenter – Institute of Earth sciences, University of Graz, using more than 100 international reference standards.

For trace element and rare earth element determination, two garnet profiles were measured using Laser-ablation inductively coupled plasma mass spectrometry (LA-ICP-MS). Analyses were conducted with an Agilent 7500cx quadrupole mass spectrometer and samples were ablated using an ESI NWR 193 Laser

at the NAWI Graz Central Lab for Water, Mineral and Rocks, University of Graz and Graz University of Technology.

Mineral formulae, mineral endmembers and geothermobarometric calculations were conducted using Petrological Elementary Tool (PET) for Mathematica by (Dachs, 1998).

### 3. Petrography

According to mineral assemblage and texture, there are several types of cordierite bearing gneisses that can be observed in the WC. In the following section the samples are grouped and described accordingly.

1.) Garnet-biotite-cordierite gneisses with the mineral assemblage Grt+Crd+Bt+Plg+Kfs+Qtz+Sil+Mag+Sp (e.g. sample S2-S5) contains large symplectitic garnet porphyroblasts (Figure 8 C) with quartz, plagioclase and minor biotite in the garnet core and sillimanite in the mantle/rim as inclusions, along with monazite, zircon and minor ilmenite. Garnets reach up to 5mm in size, cordierite in the matrix as well as around garnet up to 2mm. Sillimanite occurs exclusively as inclusion in the garnet mantle and rim. K-feldspar is present as exsolution lamellae in anti-perthites or mesoperthites in the matrix along with cordierite-quartz intergrowth (Figure 7 A). Moderate amounts of large biotite are found around garnet as product of symplectite formation and in the matrix. Melt textures like myrmekites are well documented. Magnetite-hercynite intergrowth is commonly observed in samples with elevated whole rock FeO content (6-8 wt%) and occurs usually in and around garnet symplectites. Textural observations indicate the pressure decompression reaction:



Reaction 1 can be observed in almost all rock types containing garnet.

2.) Displaying a similar mineral assemblage (Grt+Crd+Bt+Plg+Kfs+Qtz+Sil+Mag+Sp) but different texture, this rock type contains large symplectitic garnet porphyroblasts with quartz, plagioclases and minor biotite in the garnet core and sillimanite in mantle/rim as inclusions, along with monazite, zircon and minor. Garnet is up to 2mm in size in a medium grained plagioclase/quartz matrix. K-feldspar is occasionally present in garnet symplectites which is restricted to a few more mafic samples (e.g. sample S21). Sillimanite is absent in the matrix. In contrast to e.g. sample S2 - S5 this rock type recorded several stages of the garnet-breakdown, shown in Figure 8 A and B: 1.) Thin cordierite corona (10  $\mu\text{m}$ ) around idiomorphic to- hyp-idiomorphic garnet. 2.) hyp-idiomorphic to xenomorphic garnet surrounded by medium sized cordierite- and abundant biotite and magnetite/spinel. 3.) Almost complete consumption of garnet by abundant cordierite biotite and magnetite with hercynite exsolution (Figure 7 E, F). Biotite and oxides are significant more frequent in rocks with higher FeO (6 - 8 wt%) content.  $X_{\text{Fe}}$  of cordierite increases the more garnet is consumed.

3.) Restricted only to one sample location (Figure 6) samples S40-S42 contain the mineral assemblage Grt+Crd+Plg+Kfs+Bt+Qtz+Mag+Sp+Opx with partial consumed grains of orthopyroxene. Large perthites, anti-perthites, mesoperthites, quartz and moderate amounts of cordierite are typically defining the matrix (Figure 7 B, C). Xenomorphic garnet is present in small amounts. Quartz is partial recrystallized as small grains around myrmekitic textures. Special for this rock-type is the occurrence of orthopyroxene and perthites with a ~90/10 k-feldspar/plagioclase ratio.

4.) This rock type represents leucosomes with the garnet absent mineral assemblage Crd+Plg+Kfs+Bt+Qtz+Mag+Sp (e.g. sample S84-89, S6). In contrast to all other rock types, microcline with typical twinnings occurs in an equigranular matrix along with plagioclase, quartz and cordierite. Abundant magnetite shows occasionally intergrowth with Mg-spinel. Biotite is less frequent than in garnet-bearing parageneses (Figure 8 D).

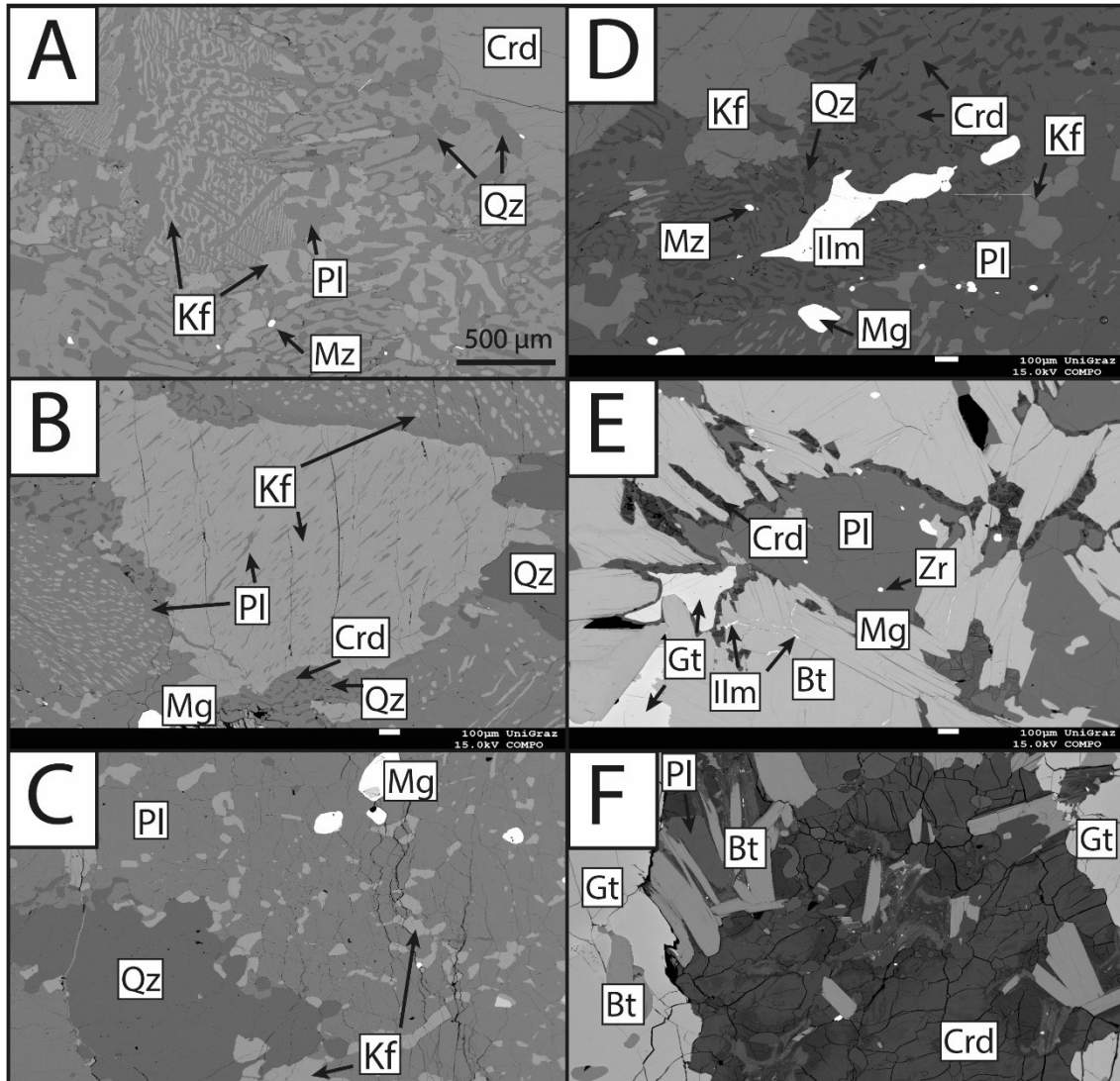


Figure 15: Back scattered electron (BSE) pictures. A.) S4: mesoperthites varying in size adjacent to quartz/cordierite intergrowth. Monazites and zircons are frequently distributed in the cordierite/quartz matrix. B.) S41: Perthite consisting of ~90% k-feldspar and ~10% plagioclase adjacent to antiperthites with a ratio of ~30/70 and quartz/cordierite intergrowth. Two-feldspar thermometry could be applied on this samples, which contains suitable perthites and antiperthites in contrast to all other samples. C.) S42: Plagioclase/k-feldspar/quartz matrix with frequently distributed magnetite. D.) S39: Ilmenite with hematite exsolutions (see mapping Figure 23) in a cordierite/quartz matrix. E.) SL8: Remains of symplectitic garnet surrounded by a fine cordierite corona. The abundant biotite inhibits fine ilmenite exsolutions and is along with cordierite most likely the product of the garnet breakdown. F.) S5: This sample with a basic chemistry display fibrous textures including cordierite, biotite and small grains of ilmenite as shown in the central part of the picture. Like in (E), the cordierite and biotite are the product of advanced garnet breakdown. Gt=garnet, Bt=biotite, Crd=cordierite, Pl=plagioclase, Kf=k-feldspar, Mg=magnetite, Mz=monazite, Zr=zircon.

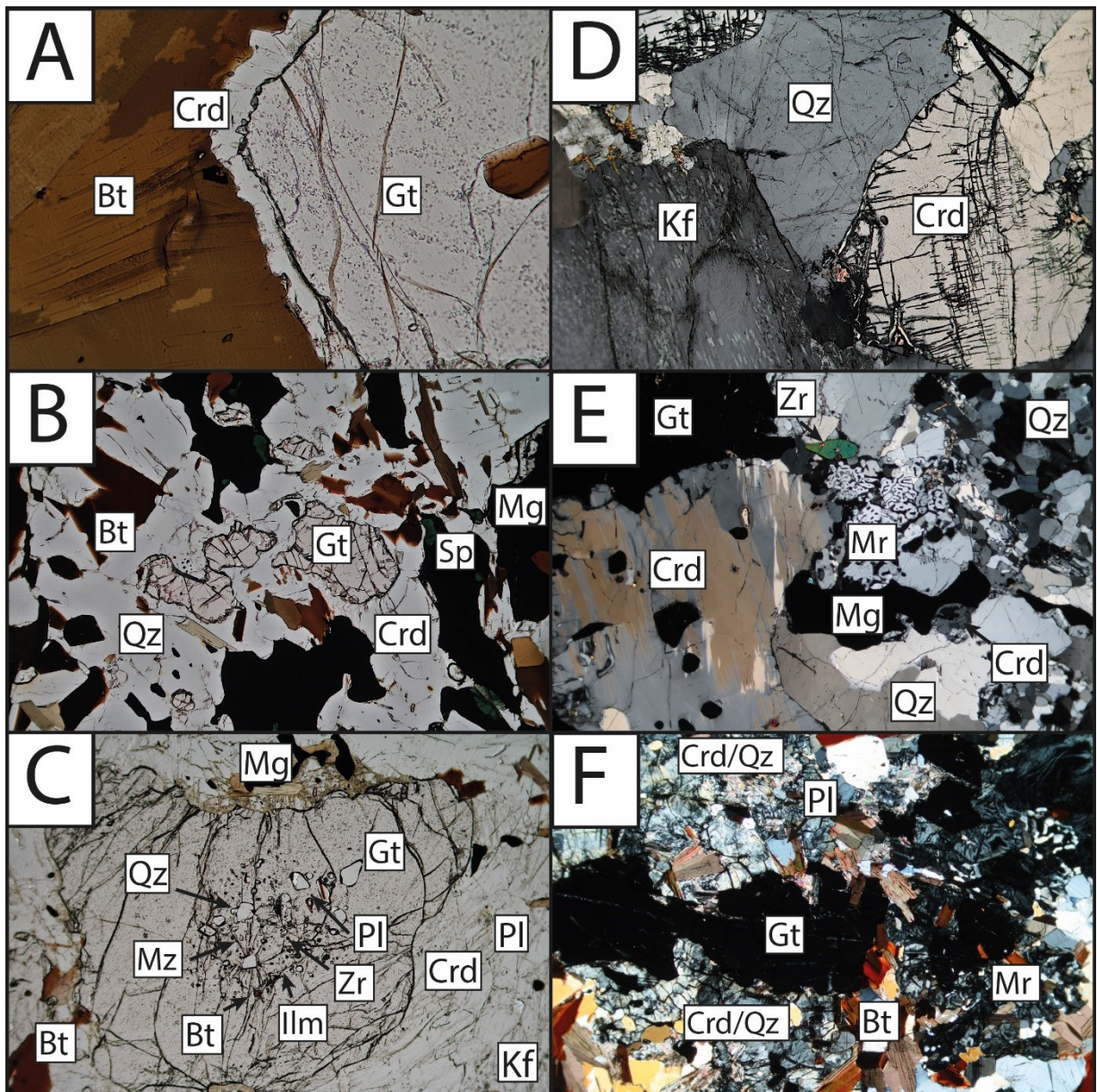


Figure 16: Photomicrographs of cordierite bearing gneisses. A.) S21 – cordierite corona around garnet. B.) S23 – advanced garnet breakdown surrounded by cordierite, quartz and magnetite symplectites. C.) S2- poikilitic garnet with beginning breakdown reaction at the rim D.) S6 – large equigranular cordierite-quartz- k-feldspar matrix. E.) S4 – Matrix with varying grainsize due melt textures and recrystallized quartz F.) S5 – Decomposing garnet in fine, partly fibrous matrix with quartz-cordierite intergrowth and extensive melt textures. Mineral abbreviations: Gt=garnet, Bt=biotite, Crd=cordierite, Pl=plagioclase, Kf=k-feldspar, Mg=magnetite, Sp=spinel, Mz=monazite, Zr=zircon, Mr=myrmecite

#### 4. Whole Rock Chemistry

The cordierite bearing gneisses from the WC are considered to be metapelites but show a varying chemistry. The majority of samples contain 55-65 wt% SiO<sub>2</sub> although some mafic samples have significant lower values ~44-50 wt%. Partial melting, as indicated by P-T estimations and migmatitic structures lead to leucosomes with up to 75 wt% SiO<sub>2</sub> and some melanosomes with around 55 wt% SiO<sub>2</sub>. The role of melt extraction and therein changes in the protoliths composition during prograde evolution is discussed in chapter 8. Although the samples represent metapelitic rocks, some trends can be observed: decreasing trends with increasing SiO<sub>2</sub> content for Al<sub>2</sub>O<sub>3</sub>, MgO, FeO and TiO<sub>2</sub> varying between 23 -11 wt%, 4.0-0.8 wt%, 9.0 - 2.5 wt% and 1.8 - 0.1 wt%, respectively (Figure 9). CaO and Na<sub>2</sub>O show no obvious trends, although changes in Na<sub>2</sub>O can be significant (between 0.1 and 6.0 wt%) and display a slight positive trend. Y and Zn show a slight negative trend with SiO<sub>2</sub>, other trace elements (Rb, Sr, Zr and Ba) show no systematic behavior (Figure 11). Samples with low SiO<sub>2</sub> (50-44 wt%) and high Al<sub>2</sub>O<sub>3</sub> (17-24 wt%) and FeO (11-17 wt%) content typically contain high modal amounts of biotite and in some cases unusual high amounts of garnet. These rocks are most likely restites where a melt phase was extracted during high grade metamorphism. Alternatively, they could represent an original Al-enriched precursor sediment. These rocks contain 3-4 wt% Na<sub>2</sub>O and 60-69 wt% SiO<sub>2</sub>. Whole rock compositions are shown in Table 2, 3 and 4.

Felsic granulites and leucosomes with >70 wt% SiO<sub>2</sub>, Na<sub>2</sub>O between 0.15 – 0.55 wt% and K<sub>2</sub>O between 2.7 – 5.3 wt% are mainly represented by samples S85-S87 at the northern boundary with Kadugannawa Complex. The K<sub>2</sub>O/Na<sub>2</sub>O ratio is significantly higher (6-14) due to lower Na<sub>2</sub>O contents. Garnet is absent in these samples. Al<sub>2</sub>O<sub>3</sub> and FeO contents range between 10 - 13 wt% and 3.5 - 5.5 wt%, respectively. These samples may represent leucosomes and display an approximate granitic composition which is consistent with the melting behavior of metapelites.

A diverse chemistry of these metasedimentary rocks, migmatitisation and large abundances of biotite make the exact determination of the protolith difficult, although layered and banded structures along with high Al<sub>2</sub>O<sub>3</sub> content argue for a sedimentary origin.

Table 2: Representative XRF analyses for major (wt%) and trace elements (ppm).

Sample	SL8	SL7	SL318	SL315	SL308	SL307	SL306	SL2	SL162	SL160
SiO <sub>2</sub>	61.40	69.87	63.68	55.70	62.18	49.70	62.01	46.97	74.36	76.52
TiO <sub>2</sub>	0.99	0.60	0.94	1.46	0.87	0.06	0.07	1.34	0.76	0.48
Al <sub>2</sub> O <sub>3</sub>	16.91	12.61	17.30	17.78	15.84	19.09	16.48	24.67	10.02	10.77
Fe <sub>2</sub> O <sub>3</sub>	6.99	7.37	6.77	12.23	7.99	17.26	9.54	11.97	5.42	3.81
MnO	0.27	0.02	0.06	0.28	0.13	1.12	0.58	0.17	0.08	0.03
MgO	2.98	0.42	2.18	4.10	2.96	6.93	3.60	3.52	3.13	0.77
CaO	2.32	2.60	1.18	2.12	3.33	2.58	1.85	1.58	1.32	1.42
Na <sub>2</sub> O	3.00	3.24	1.60	2.50	3.17	1.81	1.90	1.87	0.22	0.46
K <sub>2</sub> O	3.97	1.11	3.99	2.44	2.22	0.90	3.00	5.91	2.93	4.14
P <sub>2</sub> O <sub>5</sub>	0.09	0.05	0.20	0.09	0.07	0.06	0.06	0.56	0.08	0.06
LOI	0.32	0.78	1.04	0.22	0.27	0.01	0.01	0.33	0.74	0.76
Sum	98.91	97.89	99.24	99.14	98.76	99.50	99.08	98.55	99.22	99.47
Ba (PPM)	1031	293	1372	605	806	272	1231	2683	518	1072
Ce (PPM)	<20	<20	145	102	80	51	33	<20	33	159
Cr (PPM)	62	57	27	100	58	<20	<20	113	57	<20
Cs (PPM)	<20	<20	<20	<20	<20	<20	<20	<20	<20	<20
Cu (PPM)	<20	22	<20	<20	<20	<20	<20	57	<20	<20
Ga (PPM)	<20	29	<20	22	<20	<20	<20	49	<20	<20
Nb (PPM)	<20	<15	<20	20	<20	<20	<20	23	<20	<20
Nd (PPM)	35	27	62	47	22	<20	<20	133	<20	57
Ni (PPM)	<20	<20	32	59	21	<20	<20	35	67	50
Pb (PPM)	23	<20	<20	<20	<20	<20	<20	36	<20	20
Rb (PPM)	192	31	89	84	49	<20	60	192	180	132
Sc (PPM)	25	<20	<20	37	<20	133	82	58	<20	<20
Sr (PPM)	304	295	242	209	337	175	250	298	86	180
Th (PPM)	21	<20	29	<20	<20	<20	<20	55	21	51
U (PPM)	<20	<20	<20	<20	<20	<20	<20	<20	<20	<20
V (PPM)	80	137	103	207	132	22	<20	218	72	39
Y (PPM)	37	<20	40	44	29	239	179	98	<20	<20
Zn (PPM)	89	166	98	150	103	82	33	211	79	<20
Zr (PPM)	266	443	311	278	185	144	125	676	262	261

Table 3: Representative XRF analyses for major (wt%) and trace elements (ppm). Continued.

Sample	S89	S87	S86	S85	S83	S7	S6	S5	S42	S41
SiO <sub>2</sub>	74.75	73.38	74.68	70.41	81.52	59.04	65.33	44.87	66.07	59.70
TiO <sub>2</sub>	0.75	0.49	0.56	0.59	0.55	0.87	0.41	1.23	0.81	0.99
Al <sub>2</sub> O <sub>3</sub>	10.72	12.82	11.79	13.78	5.77	23.15	20.03	20.96	15.92	17.36
Fe <sub>2</sub> O <sub>3</sub>	5.00	3.69	4.43	4.49	4.08	2.43	4.69	17.35	6.76	8.71
MnO	0.06	0.03	0.04	0.06	0.05	0.01	0.03	0.42	0.11	0.09
MgO	1.92	1.04	1.74	2.00	2.12	2.78	4.28	6.78	1.74	2.23
CaO	2.06	2.20	2.51	1.11	1.77	1.11	0.17	2.29	2.97	2.37
Na <sub>2</sub> O	0.46	0.58	0.40	0.46	0.15	6.07	0.51	1.62	3.22	2.62
K <sub>2</sub> O	2.71	4.01	2.84	5.34	1.44	2.56	1.59	2.67	1.82	3.96
P <sub>2</sub> O <sub>5</sub>	0.04	0.03	0.04	0.07	0.06	0.10	0.05	0.08	0.05	0.07
LOI	0.61	0.72	0.84	0.81	1.90	0.76	2.13	0.85	0.12	0.39
Sum	99.28	99.24	99.02	99.32	99.50	99.06	99.38	98.26	99.48	98.10
Ba (PPM)	573	1308	806	854	249	582	281	371	641	1832
Ce (PPM)	126	92	102	68	30	164	148	161	93	63
Cr (PPM)	73	22	28	50	41	139	44	<20	33	38
Cs (PPM)	<20	<20	<20	<20	<20	<20	<20	<20	<20	<20
Cu (PPM)	<20	<20	<20	<20	<20	<20	<20	<20	<20	<20
Ga (PPM)	<20	<20	<20	<20	<20	27	35	25	<20	<20
Nb (PPM)	<20	<20	<20	<20	<20	20	<20	24	<20	<20
Nd (PPM)	39	21	20	27	<20	60	89	78	40	20
Ni (PPM)	78	52	28	47	41	76	73	<20	<20	<20
Pb (PPM)	<20	<20	23	25	<20	<20	<20	76	<20	<20
Rb (PPM)	130	134	108	207	71	87	91	189	29	67
Sc (PPM)	<20	<20	<20	<20	<20	<20	<20	22	<20	<20
Sr (PPM)	189	169	149	170	26	156	59	112	345	397
Th (PPM)	24	<20	38	<20	<20	30	56	34	<20	<20
U (PPM)	<20	<20	<20	<20	<20	<20	<20	<20	<20	<20
V (PPM)	59	42	44	45	64	119	31	75	99	129
Y (PPM)	<20	<20	<20	<20	<20	<20	<20	95	38	30
Zn (PPM)	53	21	52	53	36	41	216	503	61	61
Zr (PPM)	196	220	247	175	175	178	106	256	299	202

Table 4: Representative XRF analyses for major (wt%) and trace elements (ppm). Continued.

Sample	S40	S4	S39	S3	S24	S23	S22	S21	S2	S13
SiO <sub>2</sub>	64.67	62.69	63.13	63.84	65.82	66.94	60.47	46.68	53.59	56.94
TiO <sub>2</sub>	0.93	0.21	0.96	0.59	0.73	0.73	1.34	1.79	1.01	1.24
Al <sub>2</sub> O <sub>3</sub>	15.39	22.33	16.56	19.05	15.44	16.28	16.71	18.05	20.90	19.78
Fe <sub>2</sub> O <sub>3</sub>	7.08	3.26	6.33	3.06	6.38	6.36	8.92	14.24	13.84	11.08
MnO	0.09	0.04	0.03	0.01	0.13	0.12	0.16	0.30	0.18	0.14
MgO	1.99	3.21	2.26	2.38	1.97	1.82	3.21	7.75	5.10	3.58
CaO	2.58	1.26	2.83	2.30	2.78	2.11	2.17	2.13	0.82	2.04
Na <sub>2</sub> O	3.13	3.30	3.25	4.69	3.36	2.16	2.20	1.90	1.39	1.94
K <sub>2</sub> O	3.01	2.40	3.32	1.93	2.08	2.55	2.57	4.40	0.78	1.52
P <sub>2</sub> O <sub>5</sub>	0.06	0.07	0.06	0.08	0.23	0.13	0.07	0.37	0.05	0.06
LOI	0.17	0.72	0.17	0.52	0.20	0.43	0.89	0.41	1.66	0.65
Sum	99.34	98.77	98.73	97.93	99.33	99.19	97.82	98.41	97.64	99.16
Ba (PPM)	1017	343	1360	219	458	1160	780	1166	111	325
Ce (PPM)	85	189	62	178	73	72	72	109	95	158
Cr (PPM)	43	<20	42	191	38	30	64	683	191	129
Cs (PPM)	<20	<20	<20	22	<20	<20	<20	<20	28	<20
Cu (PPM)	21	<20	<20	<20	268	<20	<20	<20	<20	<20
Ga (PPM)	<20	28	<20	26	<20	<20	22	26	23	28
Nb (PPM)	<20	<20	<20	<20	<20	<20	<20	25	28	<20
Nd (PPM)	43	82	<20	60	31	39	<20	33	47	65
Ni (PPM)	39	<20	<20	49	42	<20	25	108	54	59
Pb (PPM)	<20	46	23	32	<20	<20	<20	<20	<20	<20
Rb (PPM)	69	45	62	111	58	53	90	215	48	59
Sc (PPM)	23	<20	<20	<20	<20	<20	28	42	34	22
Sr (PPM)	330	115	399	166	227	261	213	148	62	202
Th (PPM)	<20	28	<20	54	<20	<20	<20	33	30	35
U (PPM)	<20	<20	<20	<20	<20	<20	<20	<20	<20	<20
V (PPM)	118	21	110	122	101	103	154	212	125	151
Y (PPM)	38	39	<20	<20	33	33	46	43	74	23
Zn (PPM)	44	77	65	75	81	72	105	213	152	118
Zr (PPM)	235	424	198	204	133	166	198	573	151	291

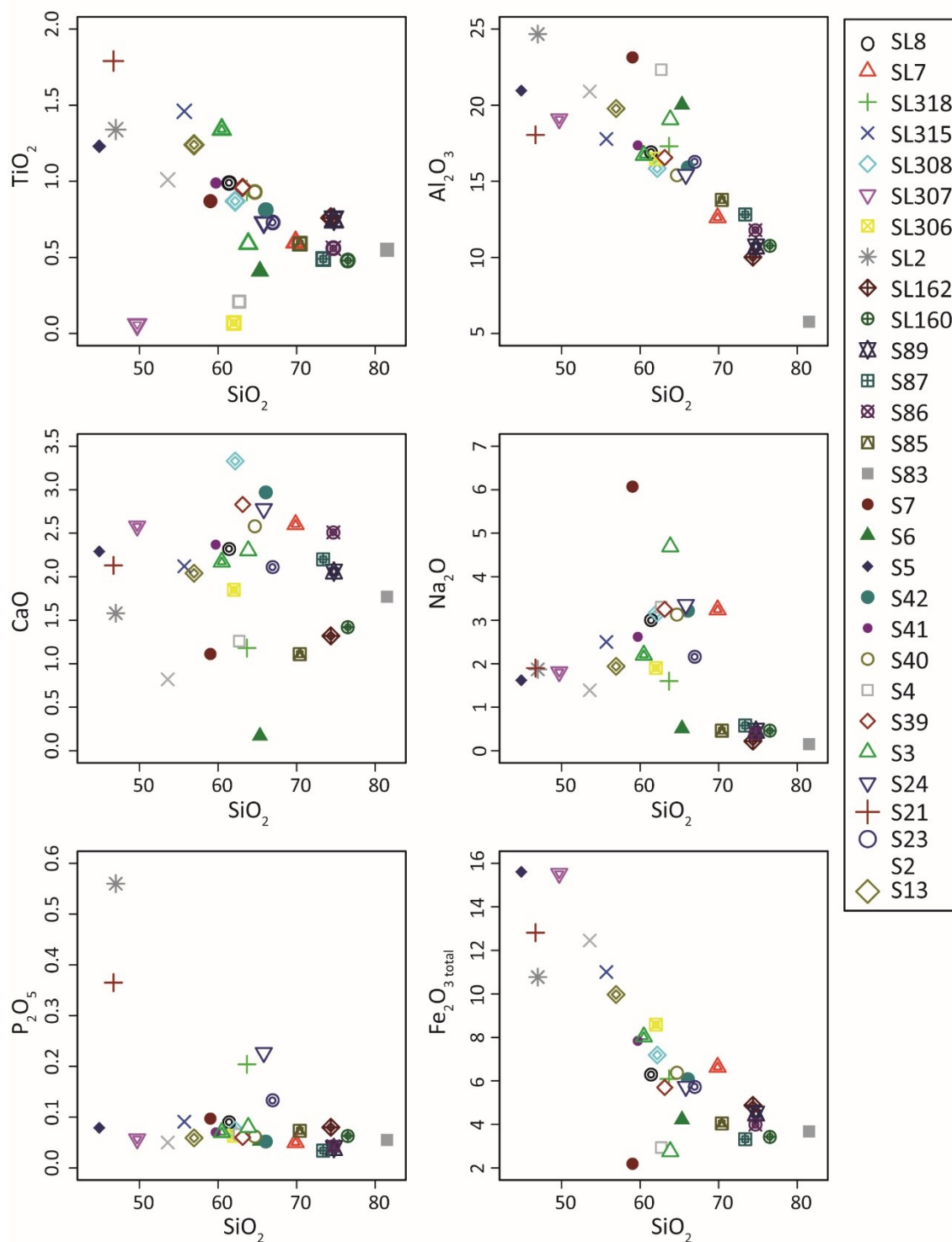


Figure 17: Major element trend (between 0.1 and 6 wt%) plots with  $\text{SiO}_2$  show decreasing trends for  $\text{TiO}_2$ ,  $\text{Al}_2\text{O}_3$ ,  $\text{MgO}$  and  $\text{FeO}$ . While  $\text{Na}_2\text{O}$  displays a slight positive trend,  $\text{CaO}$ ,  $\text{P}_2\text{O}_5$  and  $\text{K}_2\text{O}$  show now systematic behavior.

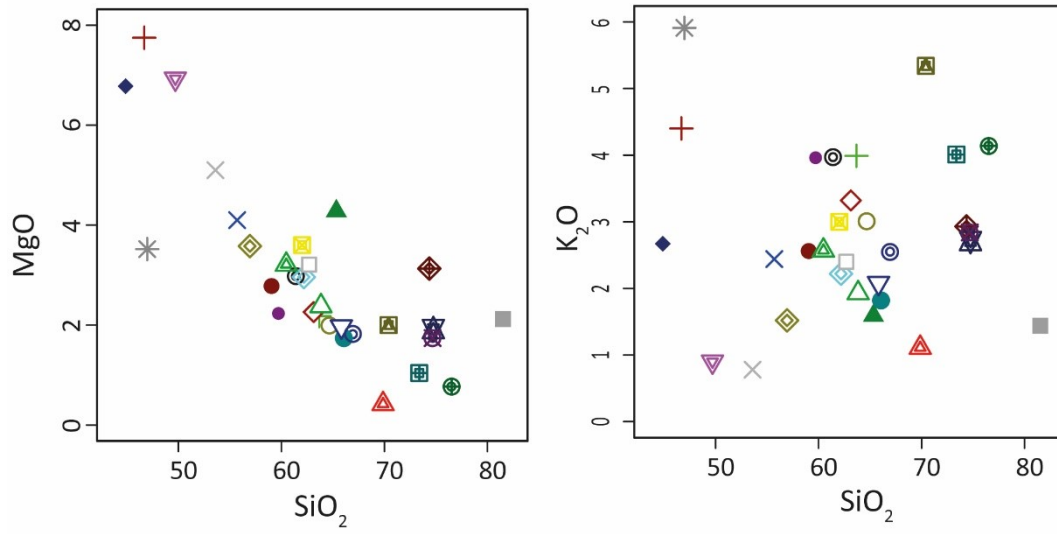


Figure 18: (Fig. 9 continued). MgO shows a systematic decrease with increasing SiO<sub>2</sub>. K<sub>2</sub>O shows no systematic behavior.

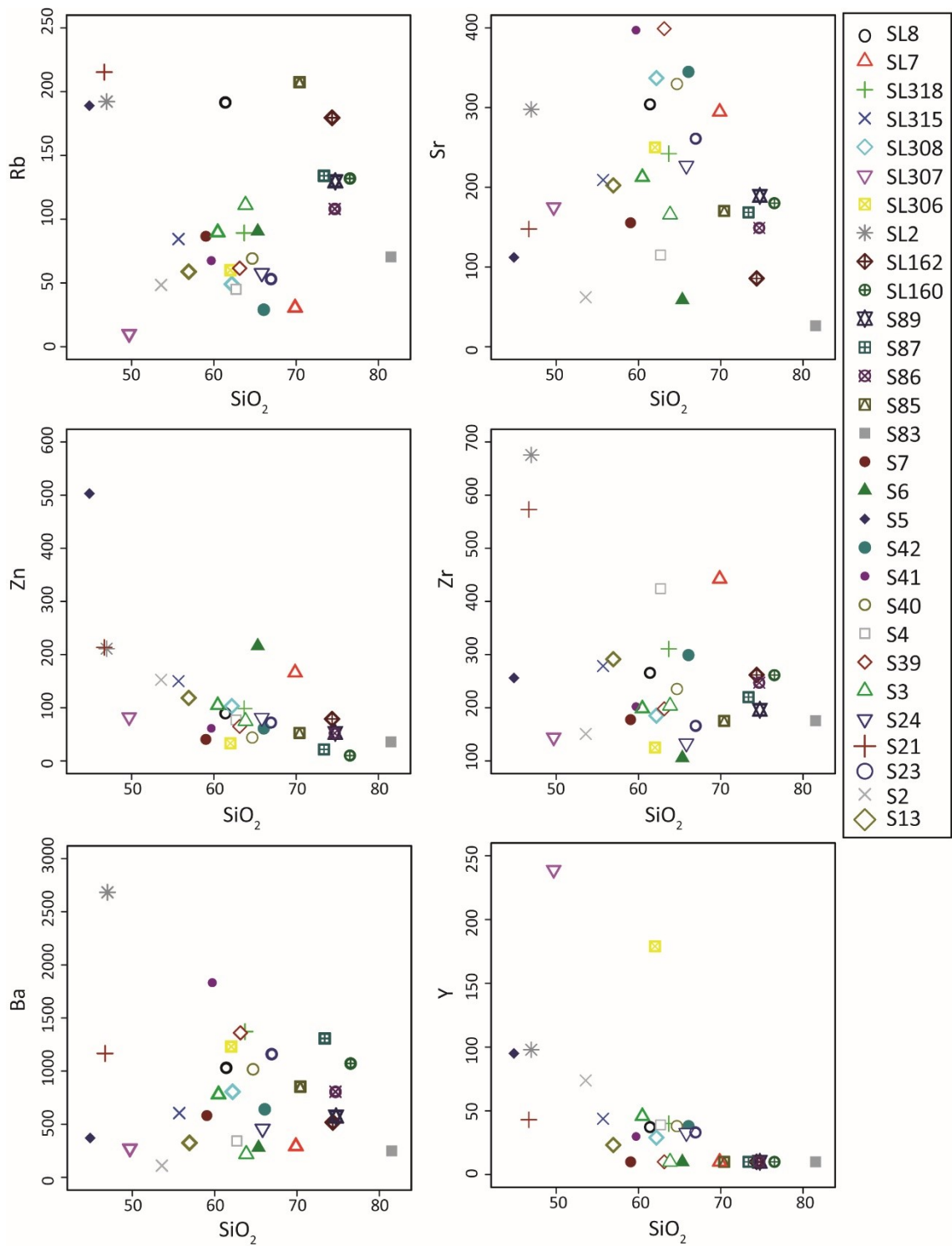


Figure 19: SiO<sub>2</sub> plot against trace elements (Rb, Sr, Zn, Zr, Ba, Y). Except Zn and Y which display a weak negative trend, no systematic behavior can be observed

## 5. Mineral chemistry

### 5.1 Garnet

Garnet occurs in 17 of the 32 examined samples with significant varying modal abundance. While garnet-biotite-cordierite bearing gneisses from the southwestern WC (Samples S4, S5) contain garnets up to 3 cm and high modal abundance (~40%), pyroxene bearing gneisses, (e.g. sample S41 - Figure 6) display only small amounts of xenomorphic garnet. Almost all garnets are at a variable degree replaced by Crd-Sp-Bt symplectites due to the decompression reaction  $Mel + Grt + Qtz + Sil = Crd + Sp + Bt$ . With minor exceptions, all garnets contain also biotite, sillimanite, plagioclase and quartz inclusions. Furthermore, accessory minerals like ilmenite, magnetite, apatite, zircon, monazite and spinel are present in garnet varying in combination, location and abundance. The relationship between core, mantle and rim inclusions in garnet is not always distinguishable, although some samples display mainly plagioclase + quartz  $\pm$  biotite inclusions in the core and sillimanite in the outer mantle or rim (Figure 12). Accessory minerals like ilmenite, magnetite, zircon, monazite, apatite, xenotime and rare hercynitic spinel can be observed in the core and mantle, ordered by decreasing abundance. There is no significant discrepancy between the chemical composition of inclusions in garnet or minerals in the matrix (e.g. biotite, Table 6) The chemical composition of garnet differs between samples although internal variation is low.  $X_{Alm}$  ( $FeO/(FeO+MgO+CaO+MnO)$ ),  $X_{Prp}$  ( $MgO/(FeO+MgO+CaO+MnO)$ ),  $X_{Grs}$  ( $CaO/(FeO+MgO+CaO+MnO)$ ) and  $X_{Sps}$  ( $MnO/(FeO+MgO+CaO+MnO)$ ) range from 0.520 - 0.731, 0.177- 0.410, 0.016-0.053 and 0.015-0.104, respectively. As shown in garnet transects (Figure 16), compositional zoning of major elements preserving a prograde history is almost absent in all garnets. Only retrograde diffusional zoning is observable in rim portions especially in contact with Fe and Mg bearing phases such as biotite (Figure 13 and Figure 14).

In some garnet mantle areas, a certain Ca enrichment can be seen (e.g. sample SL8 (Figure 15). Phosphor and Y zoning is partly inverse correlated with Ca (Figure 14 and Figure 15). Further research will be needed to interpret this pattern and relate them with a prograde history.

Table 5: Representative garnet chemistry for core and rim compositions (gtc= core, gtr = rim).

Sample Mineral	s21cgt2 grt	s5rgt2 grt	sl8gt4r grt	s41cgt1 grt	S4gtc1 grt	S23gtr2 grt	S4gtc3 grt	sl8gt4r grt	s21rgt6 grt
SiO <sub>2</sub>	38.59	37.91	36.55	38.94	38.01	38.02	38.58	36.55	38.54
Al <sub>2</sub> O <sub>3</sub>	22.23	21.68	20.87	22.25	21.95	21.84	22.34	20.87	22.09
FeO	26.83	33.14	31.79	25.53	30.46	27.40	30.58	31.79	28.26
MnO	1.70	1.01	4.49	1.59	0.89	4.64	0.90	4.49	2.21
MgO	9.70	5.88	4.34	10.60	7.97	6.49	7.95	4.34	7.84
CaO	1.13	1.34	0.99	1.06	0.57	1.76	0.58	0.99	1.25
Total	100.18	100.96	99.03	99.97	99.85	100.15	100.93	99.03	100.19
Si	2.959	2.967	2.952	2.973	2.964	2.977	2.976	2.952	2.990
Al	2.009	1.999	1.986	2.002	2.017	2.016	2.031	1.986	2.020
Fe <sub>3</sub>	0.074	0.067	0.111	0.053	0.055	0.030	0.018	0.111	0.000
Fe <sub>2</sub>	1.647	2.101	2.036	1.577	1.931	1.764	1.955	2.036	1.834
Mn	0.110	0.067	0.307	0.103	0.059	0.308	0.059	0.307	0.145
Mg	1.109	0.686	0.522	1.206	0.926	0.758	0.914	0.522	0.907
Ca	0.093	0.112	0.086	0.087	0.048	0.148	0.048	0.086	0.104
SumCat	8	8	8	8	8	8	8	8	8
Xalm	0.557	0.708	0.690	0.530	0.652	0.593	0.657	0.690	0.613
XPrp	0.375	0.231	0.177	0.406	0.313	0.254	0.307	0.177	0.303
XGr <sub>s</sub>	0.031	0.038	0.029	0.029	0.016	0.050	0.016	0.029	0.035
XSps	0.037	0.023	0.104	0.035	0.020	0.103	0.020	0.104	0.049

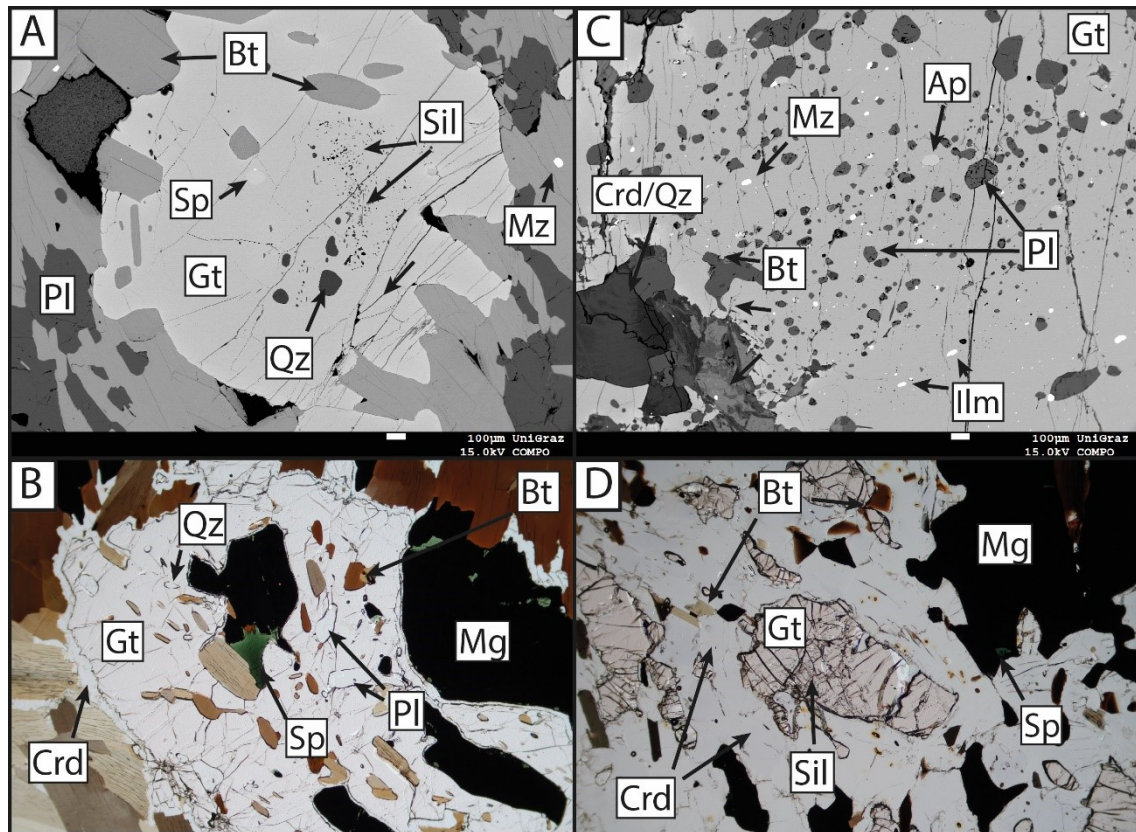


Figure 20:: A.) (SL8) BSE image of poikiloblastic garnet with Biotite, sillimanite, quartz and spinel inclusions surrounded by abundant biotite and plagioclase. B.) Photomicrograph of S21. Beginning garnet breakdown, indicated by a thin cordierite-quartz corona and abundant biotite + magnetite + spinel as product of garnet breakdown. C.) BSE image of S5. Garnet with extensive plagioclase and biotite but no quartz inclusions. D.) Photomicrograph of S23. Xenoblastic garnet after almost complete consumption leaving cordierite and magnetite with spinel intergrowth but much less abundant biotite than e.g. shown in S21. Mineral abbreviations: Gt=garnet, Qz=quartz, Bt=biotite, Crd=cordierite, Pl=plagioclase, Mg=magnetite, sil=sillimanite, Sp=spinel, Mz=monazite.

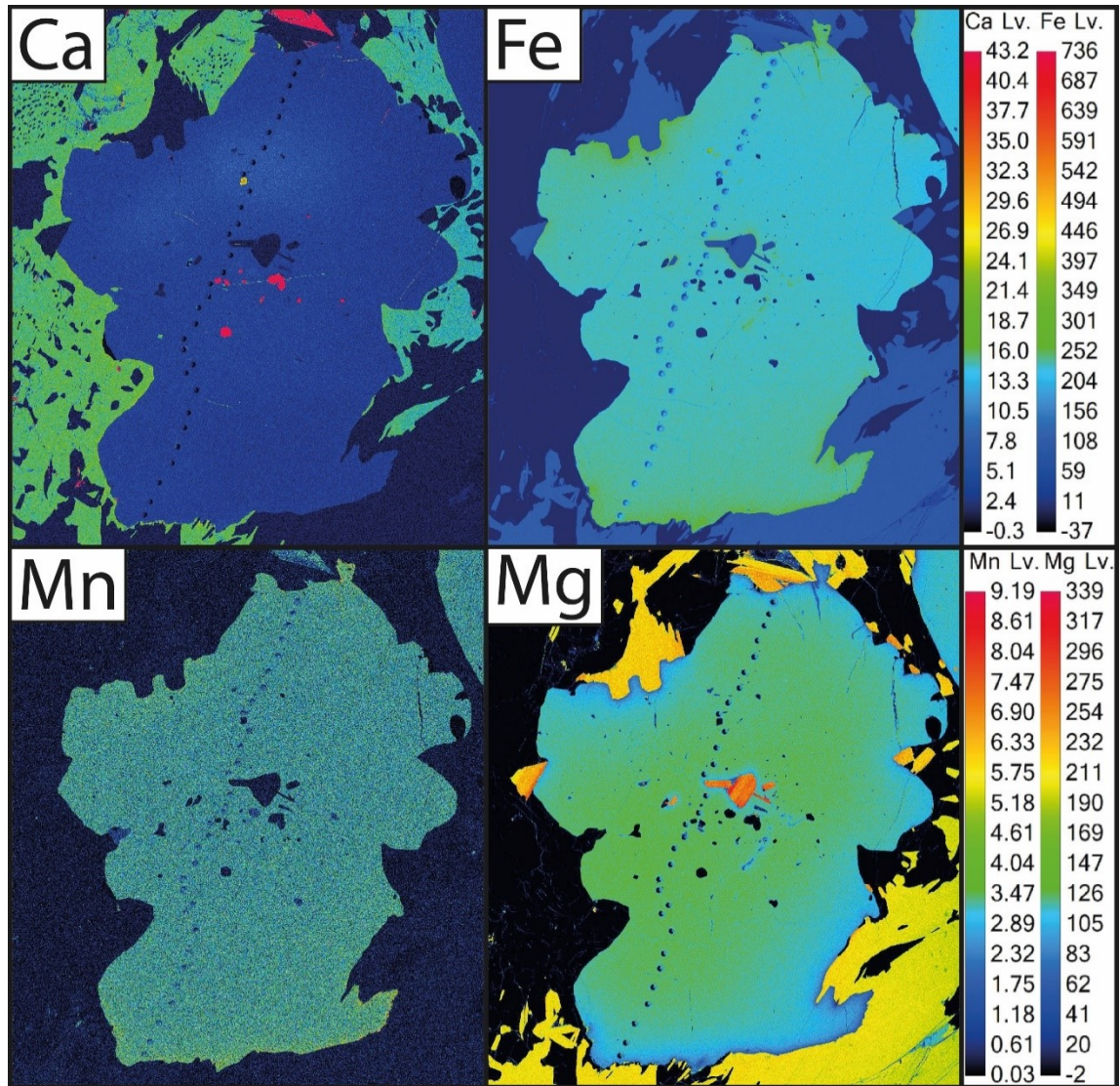


Figure 21: Elemental distribution mapping of a garnet in sample S5 for Ca, Fe, Mn and Mg. The black dotted line corresponds to the analyzed spots of an LA-ICP-MS profile (Figure 18-19). Inclusions in the garnet core are biotite, k-feldspar, plagioclase, quartz, ilmenite and apatite. Except a retrograde diffusional zoning for Fe and Mg at the contact with biotite, the garnet seems almost re-equilibrated in major elements.

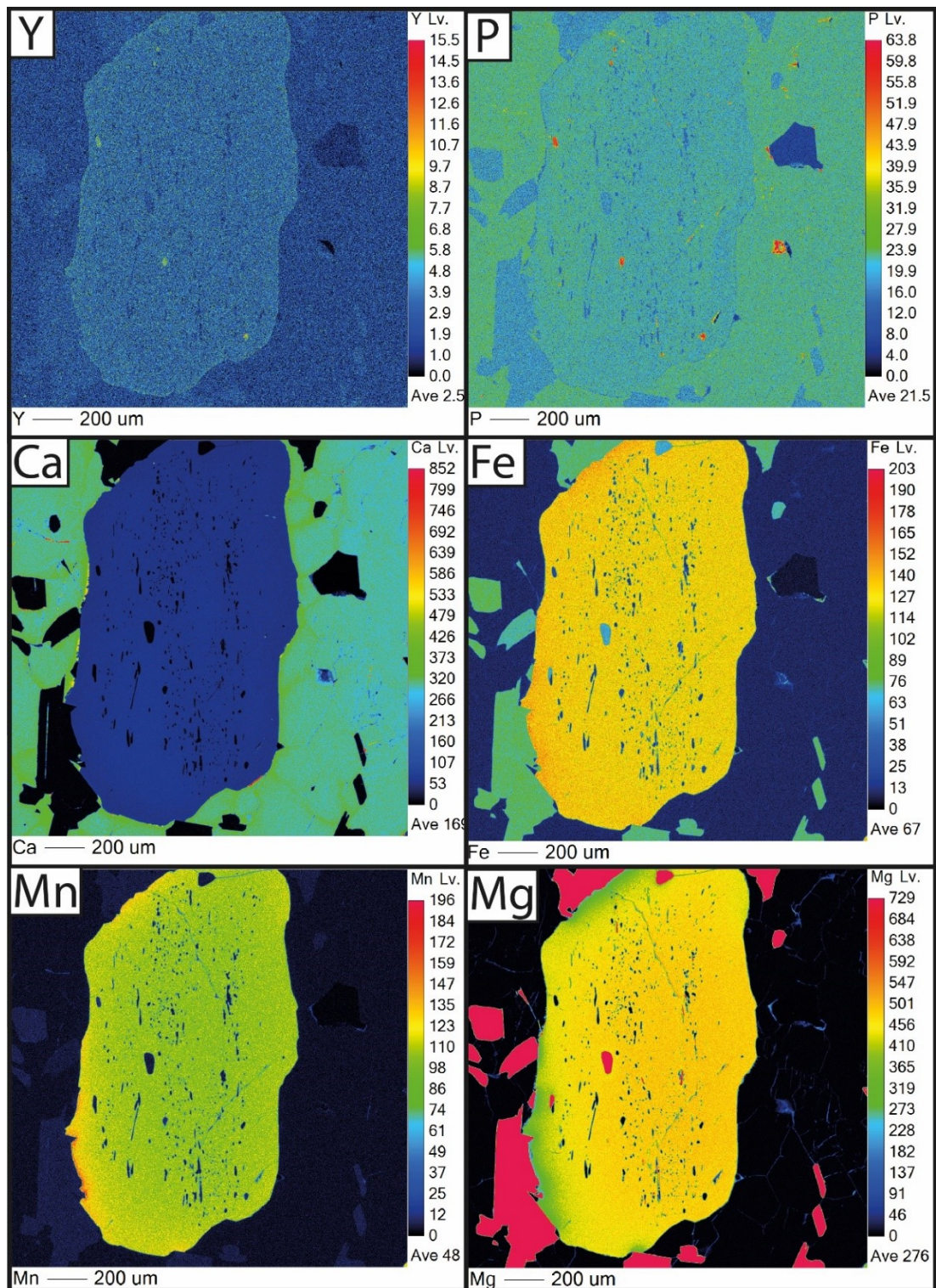


Figure 22: Elemental distribution mapping of an elongated garnet with oriented inclusions in sample SL8 for Y, P, Ca, Fe, Mn and Mg. Inclusions are sillimanite needles, quartz, biotite, magnetite, spinel monazite and zircon. A slight oscillatory like zoning for P and Y can be seen. Except the retrograde diffusional zoning of Fe and Mg in contact with biotite, a slight increase of Mn towards the rim can be observed.

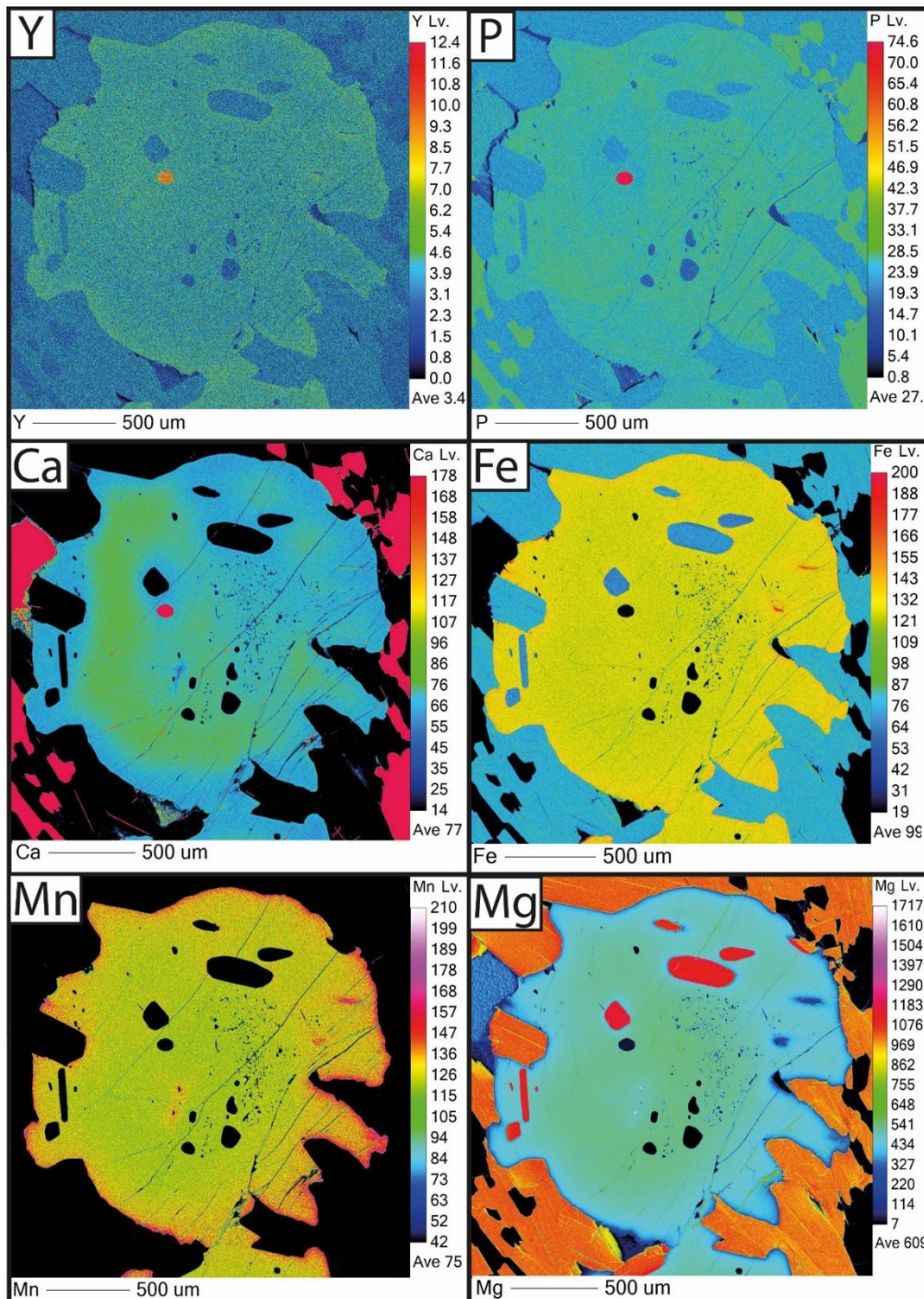


Figure 23: Elemental distribution mapping of a garnet with oriented inclusions in sample SL8 for Y, P, Ca, Fe, Mn and Mg. In contrast to most other garnets, a Ca decrease towards the rim can be observed. In the core area of the garnet, Ca decreases around inclusions with no correlation to Ca bearing phases except apatite (red dot in Ca distribution map). Indicated by the extensive amount of biotite surrounding the garnet, retrograde diffusal zoning might be the driving factor for Fe and Mg increase/decrease towards the rim, although a correlation with Ca can be observed. Mn is enriched towards the outermost rim. Y and P display a possible prograde pattern inverse related to each other, similar to Figure 14.

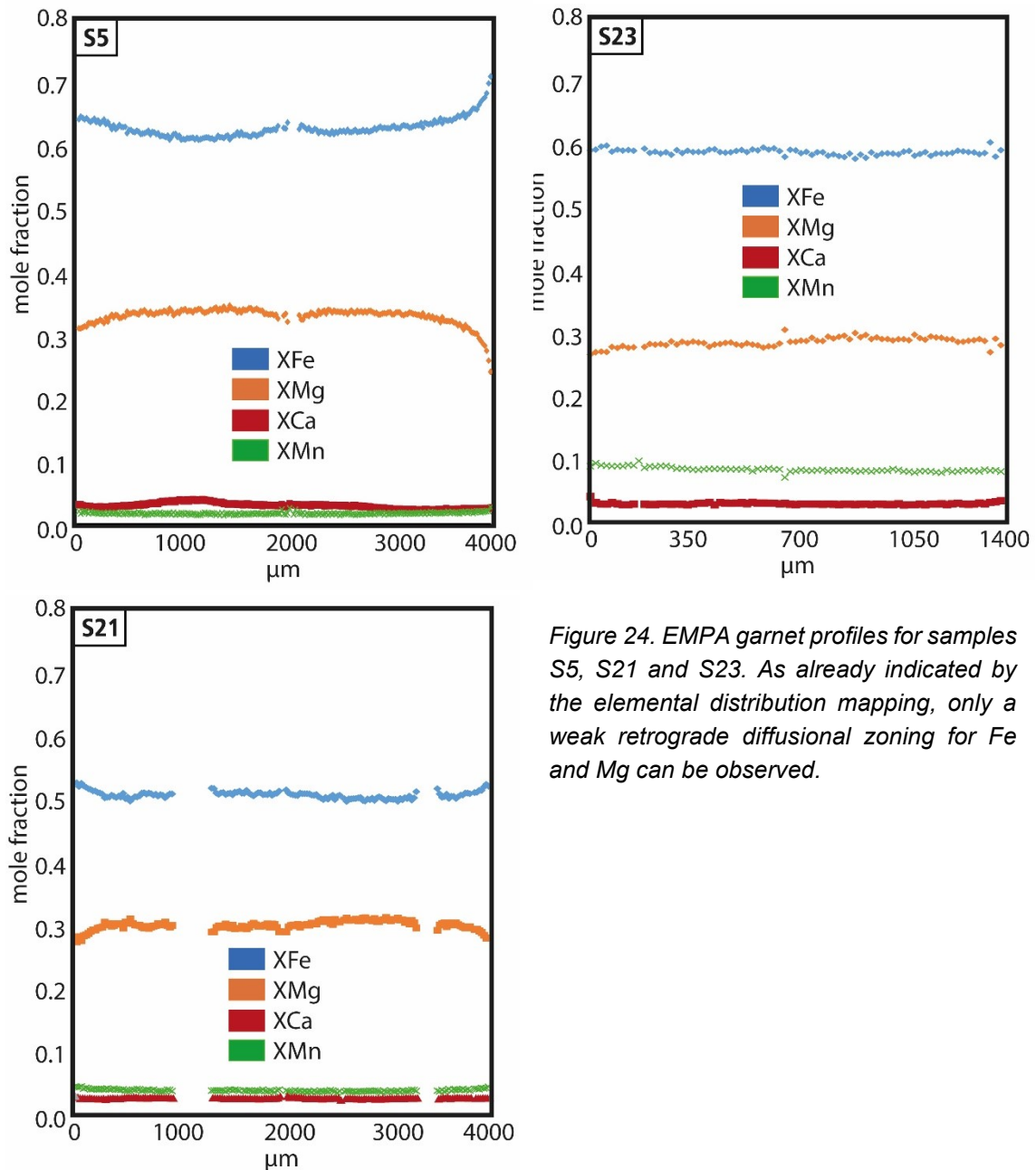


Figure 24. EMPA garnet profiles for samples S5, S21 and S23. As already indicated by the elemental distribution mapping, only a weak retrograde diffusional zoning for Fe and Mg can be observed.

Preserved rare earth element (REE) and trace element zoning patterns in garnet indicate a core, mantle and rim part. The LA-ICP-MS trace element profiles (sample S5 (Figure 13) and S21) cut through a 3,5mm and a 4mm poikiloblastic, hyp-idiomorphic and symplectitic garnet with retrograde diffusion zoning pattern at the rim. Inclusions of quartz, biotite, plagioclase, k-feldspar, ilmenite, minor apatite, zircon and monazite occur in the core area, while sillimanite, quartz and rare spinel occur in the mantle and rim parts. As shown in the chondrite normalized REE spider plot (Figure 18), heavy rare earth elements (HREE) are enriched

compared to light rare earth elements (LREE), typical for garnets. A negative Eu anomaly can be clearly observed for all garnet areas. Core, mantle and rim HREE compositions differ systematically. Garnet cores exhibit the highest concentrations in HREE, garnet mantle the lowest and the rim has values between core and mantle (Figure 17). The same feature is visible in the REE zoning patterns (Figure 18 and Figure 19). Core, mantle and rim areas indicate an enrichment in Y, Yb, Dy, and Er in the core area, depletion within the mantle area and a slight increase in the rim area again. Phosphor shows homogeneous zoning within core and mantle areas followed by an increase towards the rim. P zoning is also visible in EPMA elemental distribution maps (Figure 14 and Figure 15). Lithium does not display a clear trend. LREE show only weak zoning at partly very low concentrations (<0.1 ppm for La, Ce and Pr). The suggested core, mantle and rim cannot be correlated with major element distributions (Figure 8 -10) as Fe, Mg, Mn and mostly Ca are almost completely re-equilibrated (Figure 16).

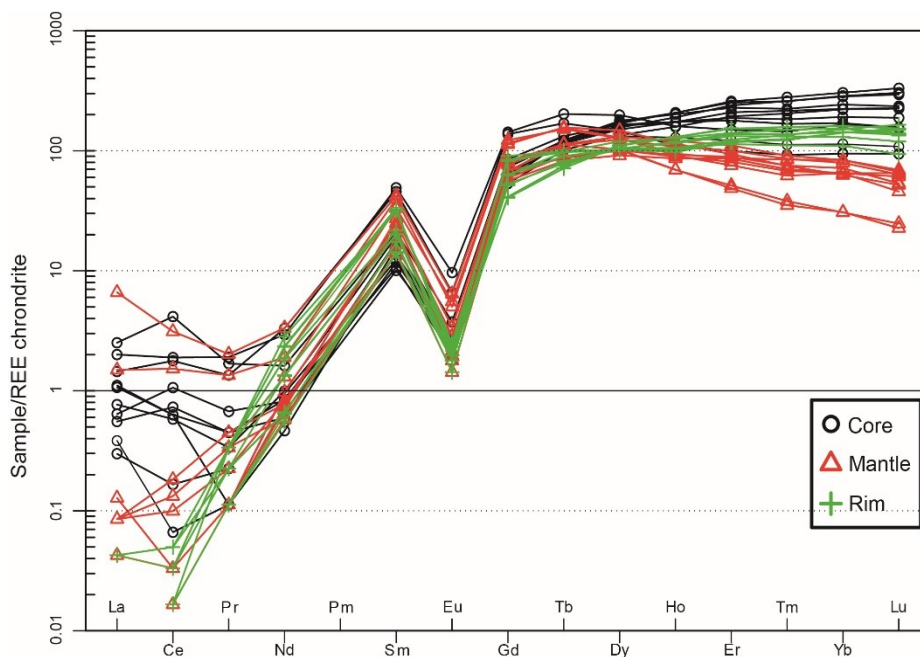


Figure 27: Chondrite normalized spider plot of REEs (sample S5). Core, mantle and rim area are represented by black, red and green colors, respectively. HREEs show a significant more distinct trend with a smaller scatter and more consistent core, mantle and rim concentrations than the LREEs.

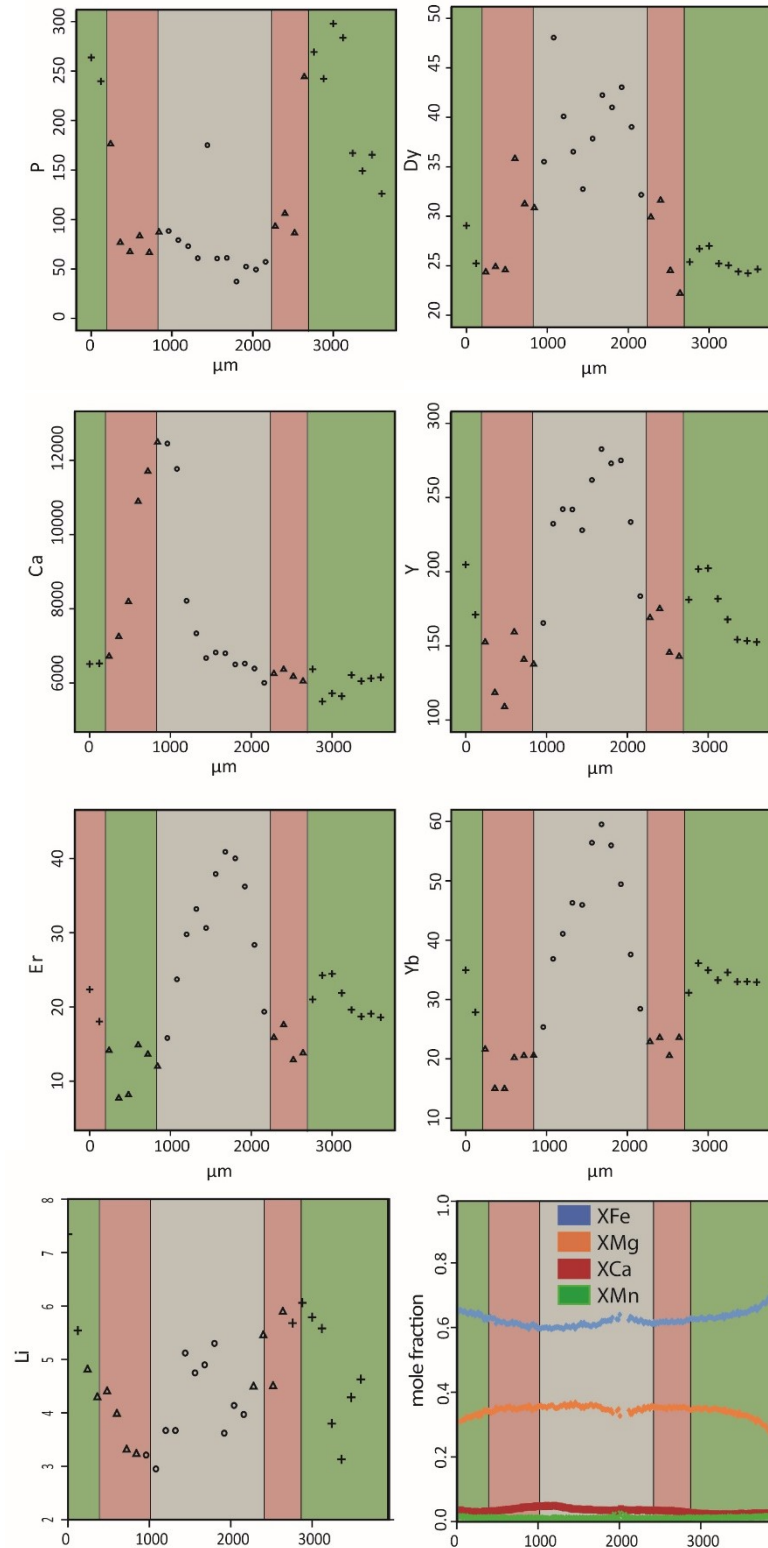


Figure 30: LA-ICP-MS profiles of garnet from sample S5 for P, Dy, Ca, Y, Er, Yb and Li and EPMA showing mole fractions of  $X_{\text{Fe}}$ ,  $X_{\text{Mg}}$ ,  $X_{\text{Ca}}$  and  $X_{\text{Mn}}$  for the respective endmembers  $X_{\text{alm}}$ ,  $X_{\text{prp}}$ ,  $X_{\text{grs}}$  and  $X_{\text{sps}}$ . Concentrations are in ppm, distance in micrometer. Grey, red and green areas indicate suggested core, mantle and rim area.

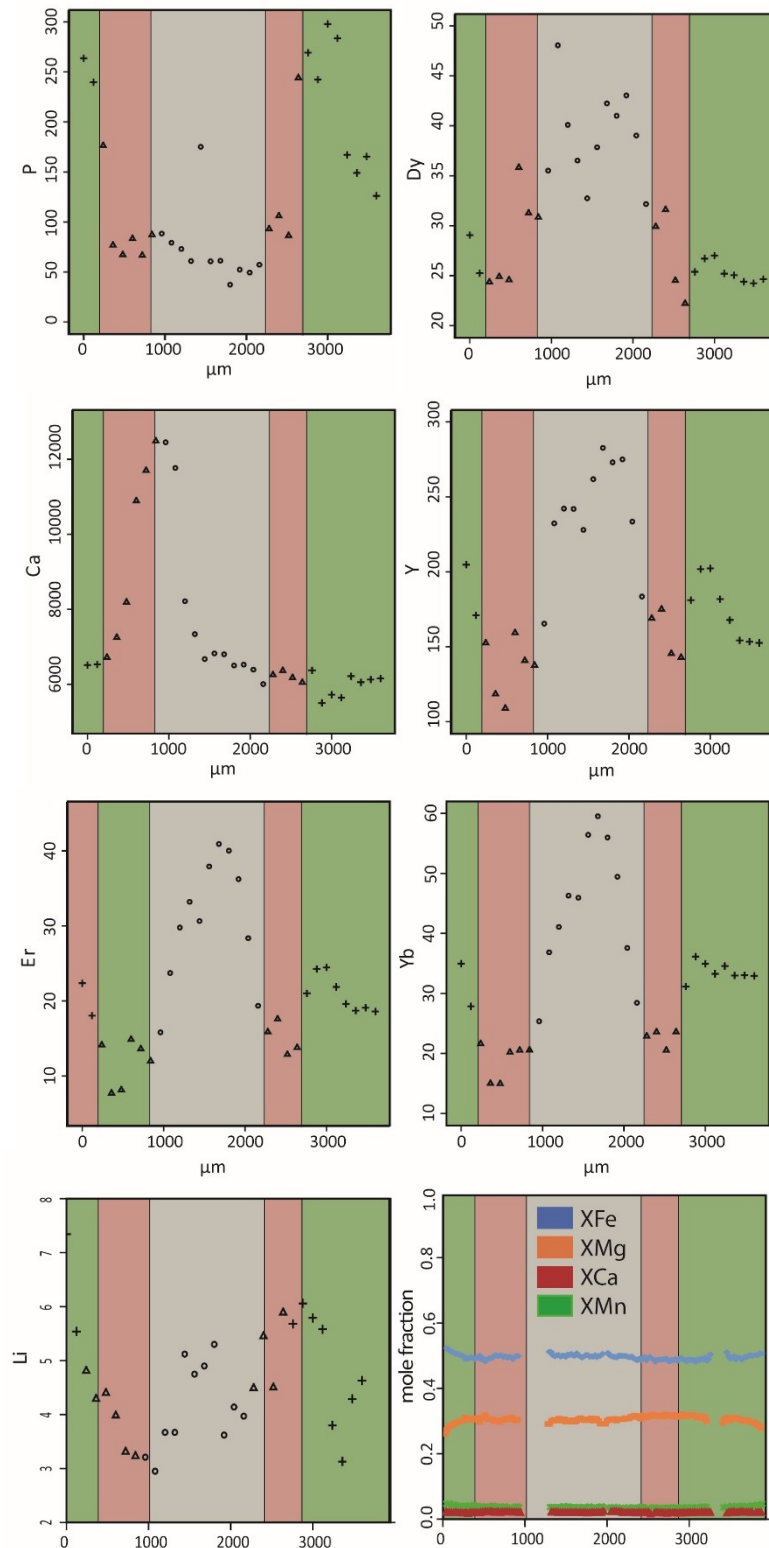


Figure 33: LA-ICP-MS profiles of garnet from sample S21 for P, Dy, Ca, Y, Er, Yb and Li and EPMA showing mole fractions of  $X_{\text{Fe}}$ ,  $X_{\text{Mg}}$ ,  $X_{\text{Ca}}$  and  $X_{\text{Mn}}$  for the respective endmembers  $X_{\text{alm}}$ ,  $X_{\text{prp}}$ ,  $X_{\text{grs}}$  and  $X_{\text{sps}}$ . Concentrations are in ppm, distance in micrometer. Grey, red and green areas indicate suggested core, mantle and rim area.

## 5.2 Biotite

Biotite is abundant in all samples (except SL160) and can be observed in layers along with garnet or within the matrix as individual flakes. Size ranges from small flakes (100  $\mu\text{m}$ ) up to 500  $\mu\text{m}$  euhedral grains. Large clusters of biotite are found around garnet symplectites usually along with magnetite, spinel and cordierite (Figure 7 E, F and Figure 8A).  $X_{\text{Ti}}$  (Ti/Mg+Fe+Al) range from 0.037 - 0.154-,  $\text{Al}^{(\text{VI})}$  (Al on octahedral site) between 0.001 – 0.35 apfu (atoms per formula unit).  $X_{\text{Mg}}$  (Mg/Ti+Mg+Fe+Al) of biotite tends to decrease with progressive garnet breakdown from 0.63 - 0.454 in garnet symplectites when almost all garnet is consumed. Biotite can be classified as phlogopite and annite following Deer, Howie, & Zussman (1992) (Figure 21). There is no significant difference between biotite which occurs as inclusion in garnet core and rim and the ones occurring in the matrix. Mineral chemistry differs from sample to sample but within one the chemical variation is only minor, as seen in Figure 20.  $\text{TiO}_2$  contents in biotite is variable and can be very high with  $\text{TiO}_2$  values of  $\sim 7.5$  wt%. As a result of the high  $\text{TiO}_2$  values biotites show commonly small (1-5  $\mu\text{m}$ ) rutile exsolution needles. Fluorine and chlorine content ranges between 0.24 - 1.58 wt% and  $<0.1$  – 0.41 wt%, respectively. Representative analyses are displayed in Table 6.

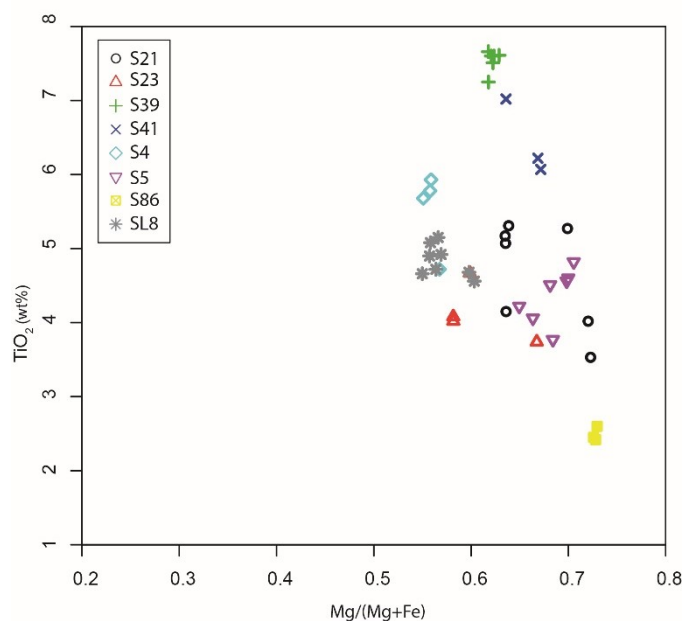


Figure 36.  $TiO_2/X_{Mg}$  plot indicates different ratios for each sample but a relatively constant chemistry within one sample. Exceptions are biotites in S5 and S41, displaying a bigger scatter although not related to their occurrence in matrix or biotite.

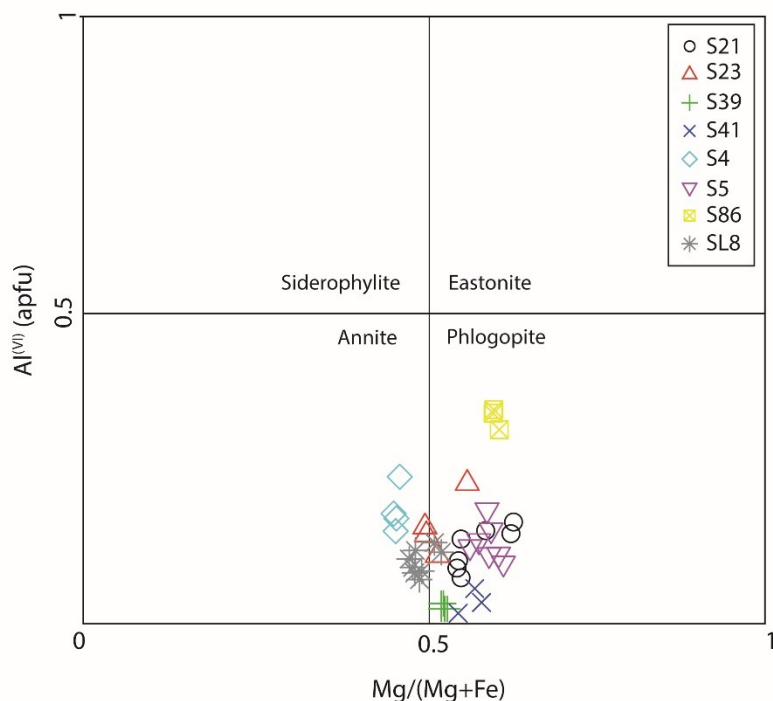


Figure 39. Biotite classification diagram after Deer et al. 1992. All analyzed biotite plot in the phlogopite field. An internal discrepancy within each sample can be observed although they clearly distinguish from each other.

*Table 6: Representative biotite chemistry for biotite as inclusion in garnet (S21bt6), in garnet contact (s5bt3 and s5bt4 in the matrix (s23bt5, s4bt3, s41cbt3 and s86bt3) and with melt texture and plagioclase intergrowth (s39bt3).*

Sample	s21bt6	s23bt5	s39cbt3	S4bt3	s5rbt3	s86rbt3	s41cbt3	s5rbt4
Mineral	bt	bt	bt	bt	bt	bt	bt	bt
SiO <sub>2</sub>	36.38	35.84	36.41	36.01	37.24	37.10	36.56	36.87
TiO <sub>2</sub>	5.27	4.67	7.51	5.93	4.82	2.42	7.02	3.77
Al <sub>2</sub> O <sub>3</sub>	16.92	15.71	15.16	16.51	15.65	18.38	14.87	15.51
Cr <sub>2</sub> O <sub>3</sub>	<0.05	<0.05	<0.05	<0.05	<0.05	<0.05	<0.05	<0.05
FeO	11.56	15.61	14.24	15.54	11.79	10.32	14.10	12.96
MnO	<0.05	0.11	<0.05	<0.05	<0.05	0.18	<0.05	<0.05
MgO	15.07	13.06	13.17	11.04	15.84	15.49	13.81	15.74
CaO	<0.05	<0.05	<0.05	<0.05	<0.05	<0.05	<0.05	<0.05
Na <sub>2</sub> O	<0.05	<0.05	<0.05	<0.05	0.17	<0.05	<0.05	<0.05
K <sub>2</sub> O	9.57	10.06	10.17	10.12	10.19	10.00	9.97	10.11
F	0.56	0.24	0.54	0.75	1.58	0.82	0.63	1.54
Cl	0.19	0.35	0.10	<0.05	<0.05	<0.05	0.12	<0.05
Total	95.52	95.65	97.30	95.90	97.28	94.71	97.08	96.50
Si	2.681	2.709	2.689	2.712	2.739	2.747	2.704	2.748
Ti	0.292	0.265	0.417	0.336	0.267	0.135	0.391	0.211
Al	1.469	1.400	1.320	1.466	1.357	1.604	1.296	1.362
Cr	0.000	0.000	0.000	0.000	0.000	0.000	0.000	0.000
Fe <sub>2</sub>	0.712	0.987	0.880	0.979	0.725	0.639	0.872	0.808
Mn	0.000	0.007	0.000	0.000	0.000	0.011	0.000	0.000
Mg	1.655	1.472	1.450	1.240	1.737	1.710	1.523	1.749
Ca	0.000	0.000	0.000	0.000	0.000	0.000	0.000	0.000
Na	0.066	0.000	0.000	0.000	0.024	0.000	0.000	0.000
K	0.900	0.970	0.958	0.972	0.956	0.944	0.941	0.961
F	0.131	0.057	0.126	0.179	0.368	0.192	0.147	0.363
Cl	0.024	0.045	0.013	0.000	0.000	0.000	0.015	0.000
SumCat	7.775	7.810	7.713	7.705	7.806	7.789	7.727	7.840
XMg	0.589	0.518	0.526	0.454	0.615	0.601	0.547	0.608
XTiM	0.104	0.093	0.151	0.123	0.094	0.047	0.140	0.073
Al(VI)	0.150	0.109	0.009	0.178	0.096	0.350	0.001	0.111

## 5.3 Feldspar

### 5.3.1 *Plagioclase*

Plagioclase is present in every sample as part of the matrix (e.g. Figure 7 C). Size range from 100  $\mu\text{m}$  up to 5 mm in leucosomes showing obvious twinning and a euhedral to subhedral shape. Plagioclase as inclusion in garnet along with quartz and  $\pm$  biotite is common in every sample. Plagioclase inclusions are restricted to the core part of the garnet except in some large xenomorphic entirely poikilitic garnets (e.g. sample S4). A third occurrence of plagioclase is as albite exsolution in perthite or mesoperthites, occurring in almost all samples (Figure 7 A, B.). Anti-perthites are less common but present in certain samples (e.g. sample S41). Myrmekitic textures and intergrowth with quartz and cordierite can be observed in the majority of samples with intergrowth diameters ranging from 10 up to 200  $\mu\text{m}$  (Figure 8 E).

The chemical composition of plagioclase ranges from  $X_{\text{alb}} = 0.581 - 0.827$ ,  $X_{\text{an}} = 0.161 - 0.405$  and  $X_{\text{or}} = 0.006 - 0.033$ .  $X_{\text{alb}} > 0.8$  values are restricted to sample S4. Another exception forms sample S86 with predominantly anorthitic plagioclase in a K-feldspar-quartz-biotite matrix along with melt textures with  $X_{\text{alb}} = 0.188 - 0.318$ ,  $X_{\text{an}} = 0.682 - 0.812$  and  $X_{\text{or}} < 0.01$ . The feldspar composition is correlated with the whole rock chemistry.  $X_{\text{alb}}$  increases with increasing  $\text{Na}_2\text{O}$  whole rock content (e.g. sample S4 - 3.3 wt%  $\text{Na}_2\text{O}$ ).  $X_{\text{an}}$  shows a similar trend. No significant chemical difference or trend for exsolution, host, inclusions in garnet or grains in the matrix can be observed. Representative analyses for plagioclase are given in Table 7.

### 5.3.2 *K-feldspar*

K-feldspar is present in every sample, the majority shows perthitic or mesoperthitic exsolutions (Figure 7 A). A microcline twinning lattice is less common. Size ranges from small, 100  $\mu\text{m}$  grains up to 4 mm in leucosomes (Figure 8 D) but tends to be smaller compared to plagioclase and the modal abundance is lower.

K-feldspar as inclusion in garnet is rare and like plagioclase restricted to the core. K-feldspar in garnet symplectites along with cordierite biotite and spinel occurs occasionally in mafic granulites e.g. sample S21. Occurrence with textures with plagioclase - quartz intergrowth, adjacent mesoperthites and cordierite - plagioclase intergrowth is common (Figure 7 D).

The chemical composition of k-feldspar is homogeneous within samples, ranging from  $X_{Or} = 0.83 - 0.97$ ,  $X_{alb} = 0.03 - 0.17$  and  $X_{an} < 0.01$ . K-feldspar as exsolution in anti-perthites or as host in mesoperthites and anti-perthites does not show any significant chemical difference or trend compared to the ones in the matrix. No chemical zoning can be observed. Barium content is usually low with  $< 0.3$  wt%. Representative analyses for k-feldspars are given in Table 7.

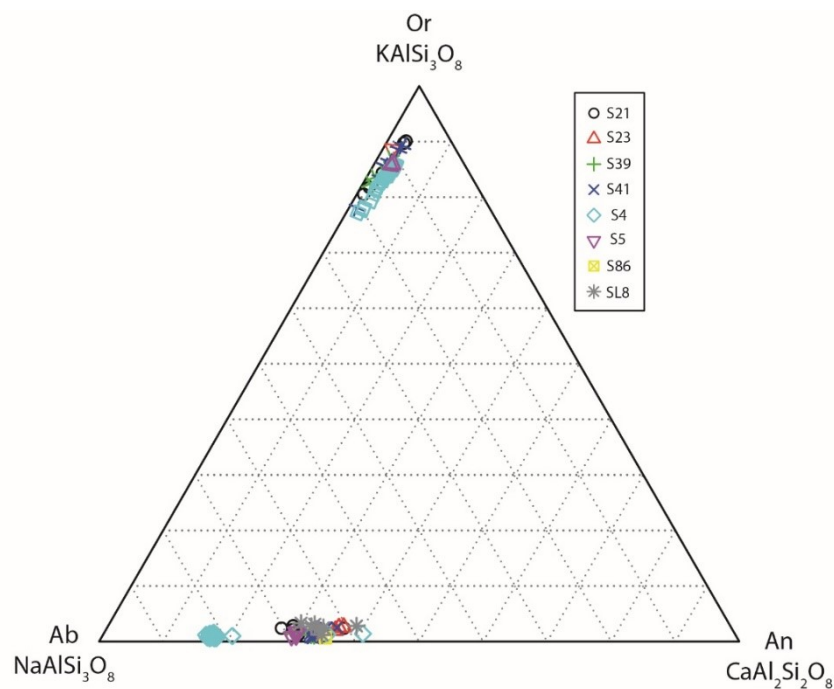


Figure 41: Ternary feldspar diagram with the endmembers anorthite (An), albite (Ab) and orthoclase (Or). All plagioclase is andesine except in S4 (oligoclase). All K-feldspars is sanidine.

### 5.3.3 *Feldspar exsolutions*

The composition of plagioclase in mesoperthites does not differ from the one in the matrix. Re integration of mesoperthites allows to determine the composition of the original ternary feldspar. Within the same sample the size of the exsolved feldspars can vary significantly from 20-100  $\mu\text{m}$  for lamellae shaped and 100-100  $\mu\text{m}$  for grain like shaped exsolutions (Figure 7 A, B). This limits the application for feldspar thermometry and suitable samples have to be selected carefully. Most samples have perthites with volumetric k-feldspar/plagioclase ratios of around 90/10. Sample S41 from Figure 7 B has a slightly lower ratio with 96/4. Anti-perthite with k-feldspar/plagioclase ratios of  $\sim 40/60$  is most common (Figure 7 A) but ratios can vary considerably. The chemical composition of plagioclase and k-feldspar in perthites, anti-perthites and mesoperthites especially in or adjacent to myrmekitic quartz-cordierite or quartz-plagioclase intergrowth is homogenous and is given in Table 7.

*Table 7: Representative k-feldspar and plagioclase analyses occurring in matrix and perthites (per).*

Sample	s86rpl3	s4Pl28per	s5pl1	s41pl7per	sl8pl7	s41kf5per	s39kf1	s23kf1	s21kf1	s4kf31
Mineral	plg	plg	plg	plg	plg	kf	kf	kf	kf	kf
SiO <sub>2</sub>	47.84	63.98	60.53	59.77	57.25	64.45	63.96	63.45	63.31	64.44
Al <sub>2</sub> O <sub>3</sub>	33.14	22.30	25.24	25.52	26.94	18.99	18.50	18.42	19.02	18.64
Fe <sub>2</sub> O <sub>3</sub>	<0.05	<0.05	<0.05	<0.05	0.25	<0.05	0.10	<0.05	<0.05	<0.05
CaO	16.08	3.55	6.32	7.07	8.07	0.15	<0.05	<0.05	<0.05	<0.05
BaO	<0.05	<0.05	<0.05	<0.05	<0.05	<0.05	0.82	0.73	0.87	0.26
Na <sub>2</sub> O	2.41	9.75	7.94	7.80	6.71	1.87	1.05	0.47	0.38	1.23
K <sub>2</sub> O	<0.05	0.13	0.17	0.12	0.48	14.34	15.39	16.19	16.49	15.39
Total	99.47	99.71	100.20	100.28	99.70	100.52	99.82	99.26	100.07	99.96
Si	2.202	2.832	2.686	2.658	2.575	2.965	2.977	2.977	2.954	2.981
Al	1.798	1.163	1.320	1.338	1.428	1.030	1.015	1.018	1.046	1.016
Fe <sub>3</sub>	0.000	0.000	0.000	0.000	0.008	0.000	0.004	0.000	0.000	0.000
Ca	0.793	0.168	0.301	0.337	0.389	0.007	0.000	0.000	0.000	0.000
Ba	0.000	0.000	0.000	0.000	0.000	0.013	0.015	0.013	0.016	0.005
Na	0.215	0.837	0.683	0.673	0.585	0.167	0.095	0.043	0.034	0.110
K	0.000	0.007	0.010	0.007	0.028	0.842	0.914	0.969	0.981	0.908
SumCat	5.007	5.008	5.000	5.012	5.013	5.024	5.018	5.020	5.031	5.020
XNa	0.213	0.826	0.688	0.662	0.584	0.829	0.906	0.958	0.966	0.892
XCa	0.787	0.166	0.303	0.331	0.388	0.164	0.094	0.042	0.034	0.108
XK	0.000	0.007	0.010	0.007	0.028	0.007	0.000	0.000	0.000	0.000

## 5.4 Cordierite

Four different types of cordierite can be observed regarding their shape, size and occurrence.

- 1.) Large euhedral grains up to 5 mm in size with slight pronounced pinitisation are part of the matrix along with plagioclase, k-feldspar and quartz (Figure 8 D). Approximate equal grain sizes and equal modal abundances indicate an equilibrated matrix. This type of cordierite occurs mainly in felsic granulites or leucosomes with high SiO<sub>2</sub> content (>65 wt% - e.g. sample S86).
- 2.) A thin corona of cordierite (20-50 µm thick) around garnet is the product of an incipient garnet decomposition. The thin corona shows intergrowth with quartz resulting in a mesh like texture. This type can be observed in sample S21 and more mafic samples (Figure 8 A).
- 3.) As sub-euhedral to euhedral grains around relictic garnet along with biotite, magnetite and Zn-bearing spinel. This represents the most common type of cordierite found in the majority of samples (Figure 7 E, F and Figure 8 F).
- 4.) Cordierite in myrmekitic intergrowth with quartz in the matrix at sub-mm scale (Figure 7 D and Figure 8 F).

Cordierite as inclusion in garnet is observed although it occurs along with biotite in symplectitic enclaves in large xenomorphic garnet which mistakenly be interpreted as inclusions.

The chemical composition of cordierite is independent from the textural type but varies between samples with  $X_{Fe}$  (Fe/Mg+Fe+Mn) = 0.123 – 0.306,  $X_{Mg}$  (Mg/Mg+Fe+Mn)= 0.694-0.860 and  $X_{Mn}$  (Mn/Mg+Fe+Mn) <0.01. There is no significant chemical variation within each sample. Samples which display cordierite in presence with high modal abundances of garnet (e.g. samples S4, S5, S18) show a higher  $X_{Fe}$  compared to samples with few or without garnet (e.g. sample S86 - Table 8). Locally, a slight positive  $X_{Fe}$  trend in cordierite can be observed with progressing garnet breakdown. Representative analyses of cordierite are given in Table 8.

*Table 8: representative analyses for different types of cordierite. Large cordierite in the matrix along with plagioclase and quartz (sample S86), type 3 as euhedral to subhedral grains around relictic garnet (samples S23, S5, S21), middle grained in the matrix with plagioclase, k-feldspar, quartz and biotite (sample S41) and in fine intergrowth with quartz (samples S39 and S4).*

Sample	s39cd4	s86cd3	s4cd6	s23cd4	s21cd3	s5cd8	s41cd1
Mineral	crd						
SiO <sub>2</sub>	49.77	49.89	48.50	49.04	50.06	48.81	49.59
Al <sub>2</sub> O <sub>3</sub>	34.14	33.83	32.59	34.05	34.27	33.23	34.08
FeO	4.10	2.92	6.96	4.94	4.27	5.80	4.09
MnO	0.11	0.39	<0.05	0.24	<0.05	<0.05	<0.05
MgO	11.14	11.43	8.86	10.65	10.99	10.18	11.08
Na <sub>2</sub> O	<0.05	0.21	<0.05	<0.05	<0.05	<0.05	<0.05
K <sub>2</sub> O	<0.05	<0.05	<0.05	<0.05	<0.05	<0.05	<0.05
Total	99.26	98.67	96.91	98.92	99.59	98.02	98.84
Si	4.976	5.000	5.028	4.946	4.988	4.981	4.976
Al	4.023	3.996	3.982	4.047	4.024	3.996	4.031
Fe <sub>2</sub>	0.343	0.245	0.603	0.417	0.356	0.495	0.343
Mn	0.009	0.033	0.000	0.021	0.000	0.000	0.000
Mg	1.661	1.708	1.369	1.601	1.632	1.549	1.658
Na	0.000	0.041	0.000	0.000	0.000	0.000	0.000
K	0.000	0.000	0.000	0.000	0.000	0.000	0.000
SumCat	11.012	11.022	10.982	11.031	11.000	11.021	11.008
XFe	0.170	0.123	0.306	0.204	0.179	0.242	0.172
XMg	0.825	0.860	0.694	0.786	0.821	0.758	0.828
XMn	0.005	0.017	0.000	0.010	0.000	0.000	0.000

## 5.5 Oxides

Magnetite occurs in every sample (20  $\mu\text{m}$  - 200  $\mu\text{m}$  size) typically accumulated around garnet (Figure 8 B) or in garnet pseudomorphs with up to 1 mm in diameter. Garnet bearing samples display intergrowth of Zn-bearing spinel with magnetite, with a grain size up to 300  $\mu\text{m}$  in diameter as well as small exsolution lamellae throughout the whole grain. Only samples SL2, SL3 and S3 contain Zn - spinel although they do not contain garnet. Spinel without magnetite is rather rare. Sample S21 displays 50  $\mu\text{m}$  big grains around garnet symplectites. Spinel contains 2.12-9.31 wt% Zn but displays no distinct trend. Spinel composition is  $X_{\text{spl}}$  (spinel) = 0.249 – 0.462,  $X_{\text{hc}}$  (hercynite) = 0.478-0.619,  $X_{\text{ghn}}$  (gahnite) = 0.044 – 0.195 and  $X_{\text{chr}}$  (chromite) = 0.000 – 0.014. Ilmenite is present in all samples and shows extensive Ti-hematite exsolution lamellae (Figure 23) with  $X_{\text{Ti}}$  = 0.6-0.8 and  $X_{\text{Ti}} \sim 0.1$  for the hematite exsolution. Representative analyses for spinel are shown in Table 9.

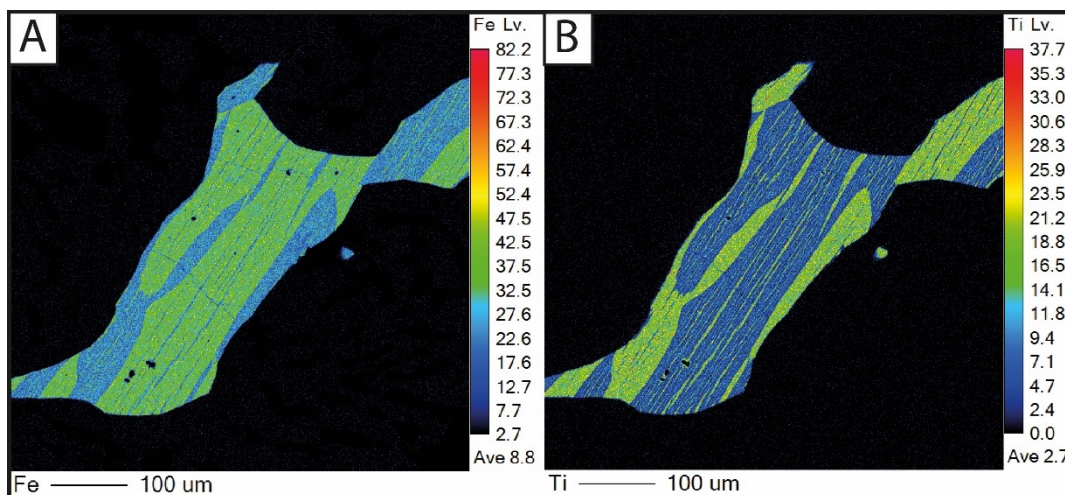


Figure 42: EMPA element distribution map of an ilmenite in matrix with hematite exsolution showing Fe (A) and Ti (B). Fe rich areas represent the hematite. Sample S39.

Table 9: Representative analyses for spinel.

Sample	s5sp1	sl8sp3	s39sp2	s21sp3	s42sp1	s23sp1
Mineral	sp	sp	sp	sp	sp	sp
SiO2	<0.05	<0.05	0.18	<0.05	<0.05	<0.05
TiO2	<0.05	<0.05	0.14	<0.05	<0.05	<0.05
Al2O3	59.26	58.20	63.23	57.29	58.95	59.07
Cr2O3	<0.05	<0.05	0.48	1.93	0.10	0.13
FeO	23.17	30.03	21.44	27.56	27.24	26.43
MnO	<0.05	0.22	0.17	0.43	0.43	0.85
MgO	6.40	7.21	11.49	6.09	8.57	7.29
ZnO	9.31	2.99	2.64	4.94	2.12	4.32
Total	98.23	98.65	99.77	98.24	97.41	98.09
Si	0.000	0.000	0.005	0.000	0.000	0.000
Ti	0.000	0.000	0.003	0.000	0.000	0.000
Al	1.982	1.925	1.990	1.926	1.947	1.959
Cr	0.000	0.002	0.010	0.044	0.002	0.003
Fe3	0.018	0.074	0.000	0.031	0.051	0.038
Fe2	0.532	0.631	0.479	0.627	0.588	0.584
Mn	0.002	0.005	0.004	0.010	0.010	0.020
Mg	0.271	0.302	0.457	0.259	0.358	0.306
Zn	0.195	0.062	0.052	0.104	0.044	0.090
SumCat	3.000	3.001	3.000	3.001	3.000	3.000
Xspl	0.270	0.296	0.462	0.255	0.356	0.308
Xhc	0.531	0.619	0.483	0.618	0.585	0.589
Xchr	0.000	0.001	0.003	0.014	0.001	0.001
Xghn	0.195	0.061	0.053	0.103	0.044	0.090

## 5.6 Orthopyroxene

Samples S41, SL 307 and SL 308 are the only samples containing small amounts of mainly strongly altered orthopyroxene with a homogenous chemical composition:  $X_{En} = 0.613 - 0.640$ ,  $X_{Fs} = 0.359 - 0.387$  and  $X_{Wo} = 0.000$ .  $Al_2O_3$  content and CaO content is 7.28 - 8.61 wt% and below detection limit, respectively. Mineral chemistry of the single sample S41 are given in Table 10.

Table 10: Representative orthopyroxene analyses.

Sample	s41op2	s41op3
Mineral	opx	opx
SiO <sub>2</sub>	48.74	47.35
TiO <sub>2</sub>	<0.05	0.24
Al <sub>2</sub> O <sub>3</sub>	7.28	8.61
Cr <sub>2</sub> O <sub>3</sub>	<0.05	0.11
FeO	20.90	22.36
MnO	0.35	0.47
MgO	21.27	20.30
CaO	<0.05	<0.05
Na <sub>2</sub> O	<0.05	<0.05
Total	98.54	99.44
Si	1.825	1.768
Ti	0.000	0.007
Al	0.321	0.379
Cr	0.000	0.003
Fe <sub>2</sub>	0.627	0.630
Fe <sub>3</sub>	0.028	0.068
Mn	0.011	0.015
Mg	1.188	1.130
Ca	0.000	0.000
Na	0.000	0.000
SumCat	4.000	4.000
X <sub>Wo</sub>	0.000	0.000
X <sub>En</sub>	0.640	0.613
X <sub>Fs</sub>	0.359	0.387

## 6. Th-U-Pb Monazite Dating

### 6.1 Introduction

Chemical U-Th-Pb monazite and U-Pb zircon age data from the south-western part of Sri Lanka around the WC/HC border defining the metamorphic overprint are rare. Recent work in this area was done by Wanniarachchi & Akasaka, (2016) who subdivided their obtained ages into 4 groups (1788-1766 Ma, 676-559 Ma, 533-507 Ma and 481-434 Ma - Figure 24) but not necessarily relating the age to the textural position of monazite and their internal texture. Kitano et al., (2018) obtained metamorphic ages from zircons varying between 600 to 490 Ma from samples close to our study area (Figure 24). Additional monazite ages were obtained around the KC and HC by Malaviarachchi & Takasu, (2011) and Sajeev et al., (2010). Wanniarachchi & Akasaka (2016) categorized monazites according to their internal texture into four types: (1) inherited core bearing monazite, (2) complexly zoned monazite, (3) oscillatory zoned monazite and (4) core rim zoned monazite based on BSE images. This nomenclature was also taken in this study to describe the monazite appearance. However, BSE images show only limited information of the chemical composition and therefore X-ray compositional maps of U, Th, Pb and Y were obtained to document the detailed chemical information and zoning in monazite. Zircon U-Pb concordia lower intercept ages of 590 - 540 Ma are consistent with the high grade Pan – African metamorphic event in the HC (Burton & O’Nions, 1990; Kröner et al., 2003; Hölzl et al., 1994). Ages on a common regression with concordia intercepts from arrested charnockites in a granitic/tonalitic host rock are interpreted by Baur et al. (1991) as intrusion age (771 Ma) and metamorphic age (563 Ma). Charnockitization is also dated using zircons at 535 Ma (Burton et al., 1990), which suggests a post-peak metamorphism process controlled by fluid influx (K. V. W. Kehelpannala et al., 1999). Zircon U-Pb isotope ages from Santosh et al., (2014) obtained from meta-granodiorites lead to the assumption for an emplacement age at 805 Ma, for a thermal event at 734 Ma and for metamorphism at 546 Ma. This sample came from a

quarry located near Kurunegala, which is far north of this study's area. The lithology consists of hornblende bearing meta-granodiorite in contrast to the in this study investigated cordierite bearing, hornblende absent metapelites and metabasites.

Age data from cordierite bearing assemblages are rare. Only LA-ICP-MS U-Pb zircon (Kitano et al., 2018) and EPMA CHIME (Chemical Th-U-Pb Isochron Method) monazite ages (Wanniarachchi et al., 2016) of 5 garnet-biotite-sillimanite-cordierite gneisses were analyzed in recent years. Location of dated samples are shown in Figure 24. It is notable that only 2 out of 6 analyzed samples from (Wanniarachchi et al., 2016) contain cordierite and their suggested age groups do not distinguish between cordierite or non-cordierite bearing rocks. If regarded individually, sample 23-32Co, a garnet-biotite-cordierite gneiss with abundant cordierite cluster at around  $525 \pm 10$  Ma and  $470 \pm 20$  Ma while sample 14-21GB, a garnet-biotite gneiss with only minor traces of cordierite shows additionally ages from inherited cores of around 1.6 Ga. Non-cordierite bearing assemblages along the WC/HC boundary area have almost similar results. Zircon ages range from 640-490 Ma, with some irregular cluster (e.g. 540-520 Ma, 630-510 Ma, 640-620 Ma.) (Kitano et al., 2018) as well as weighted means of  $806 \pm 12$  Ma,  $734 \pm 5$  Ma and  $546 \pm 6$  Ma (Santosh et al., 2014). Malaviarachchi et al., (2011) dated one garnet-biotite-sillimanite-cordierite gneiss sample southwest of Kandy as part of the HC on separated monazites, yielding 3 age groups with clusters at  $594 \pm 58$  Ma (group1),  $694 \pm 60$  Ma,  $644 \pm 58$  Ma (group2) and  $473 \pm 56$ ,  $497 \pm 57$  (group3) (weighted means). All previous dated samples are shown in Figure 24.

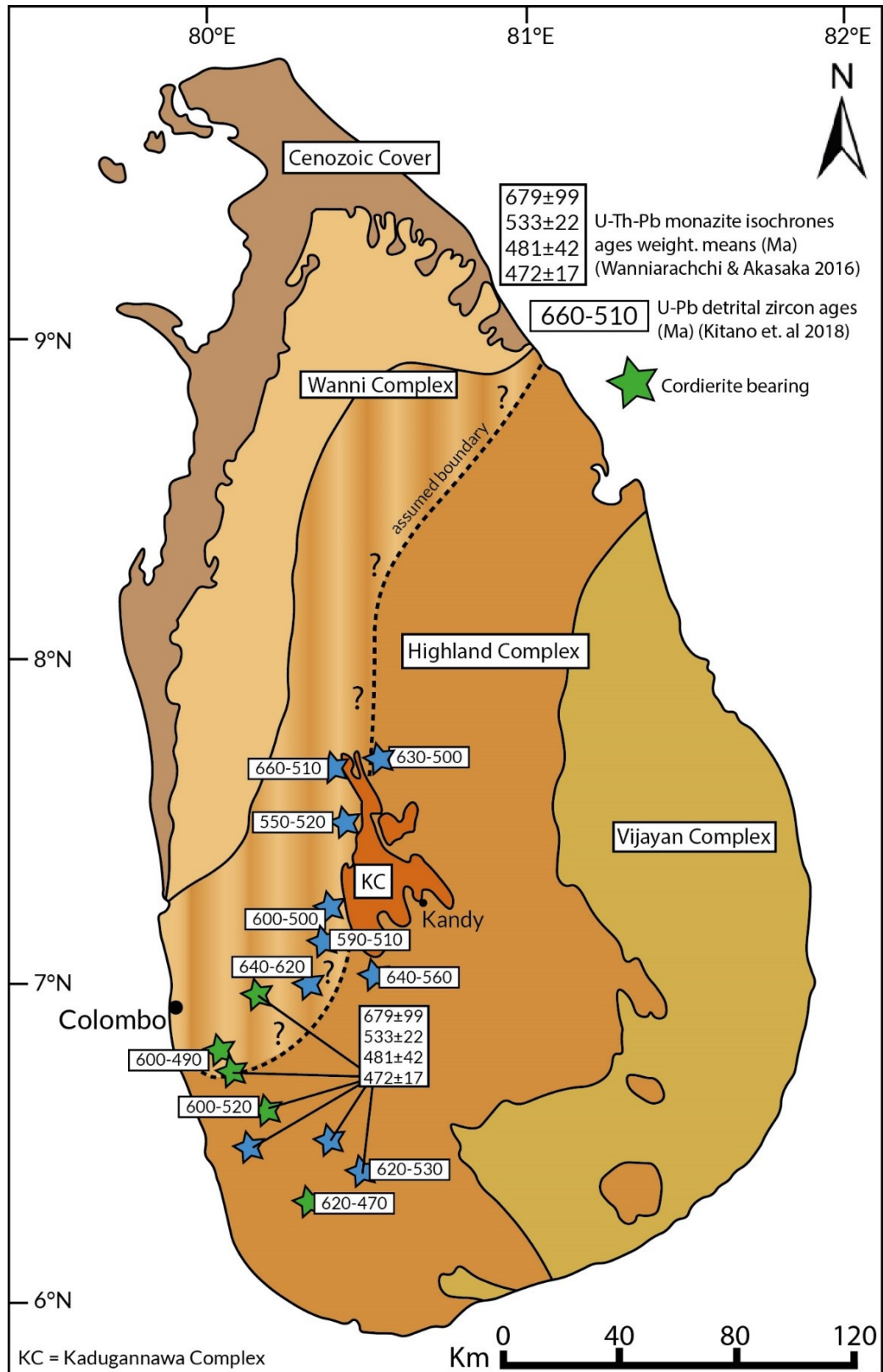


Figure 45: Location of previous dated samples in the HC/WC boundary area with their respective U-Th-Pb monazite and U-Pb detrital zircon ages in Ma. Green stars mark cordierite bearing samples. Map after Cooray 1994.

## 6.2 Method

Electron microprobe (EPMA) chemical Th-U-Pb monazite dating was performed on samples S4, S5, S21, S23, S41 and SL8 from 3 different locations. Suitable samples were chosen after careful petrographic examination, depending on monazite size, texture and abundance, sample location and relations to previous age dating. Since only 17 out of 32 cordierite bearing samples contain garnet, monazites as inclusion in garnet was rare compared to monazites in matrix. Further, most of the grains were unsuitable for EPMA analysis due to inclusions, small size (~10-20 microns) and garnets cracks which could have possibly led to fluid infiltration and monazite modification. 38 grains were analyzed with at least 4 up to 10 spots each, depending on grain texture and size. To ensure the reliability of the analysis, only measurements with 98 to 102 total wt% were used for further age calculations. Ages were calculated after Montel et al. (1996). Weighted means were calculated with IsoplotR (Vermeesch, 2018) and a 2-sigma error range. Polished thin sections with around 30 microns thickness were coated with carbon. Analysis was conducted with a JEOL JXA-8530FPlus HyperProbe Electron Probe Microanalyzer at the NAWI Graz Geocenter – Institute of Earth Sciences (University of Graz) equipped with an energy-dispersive (ED) and five wavelength-dispersive (WD) spectrometers. Beam settings are 15 kV acceleration voltage and 200 nA probe current with a diameter of 5 microns. Following standards were used for Th, U and Pb: Th - metal, U - metal and natural crocoite. Precision and reproducibility was tested by regular measurements of the following monazite age standards: Elk Mountain monazite (Peterman et al., 2012); RW-1 monazite (Ling et al., 2016); detrital monazite, Sri Lanka (in-house); Gföhl gneiss monazite (Friedl et al., 2004); ekanite, Sri Lanka (Nasdala et al., 2017). Typical counting time for Pb was 260 s on peak and background, 100 s and 30 s for U and Th respectively.

Major, trace and rare earth elements were analyzed simultaneously.

### 6.3 Chemical Composition of Monazite

Monazite is a light-rare-earth element (LREE) bearing phosphate with the formula (Ce, LREE (primarily La, Nd, Th), Y) PO<sub>4</sub>) which is present in many metamorphic or igneous rocks. Additionally, traces of U, Ca and Si are incorporated in naturally occurring monazite. Th is present by the huttonite- ( $\text{Th}^{4+} + \text{Si}^{4+} = \text{REE}^{3+} + \text{P}^{5+}$ ) and the cheralite substitution vectors ( $\text{Th}^{4+} + \text{Ca}^{2+} = 2\text{REE}^{3+}$ ), named after the end members huttonite  $\text{Th}^{4+}\text{SiO}_4$  and cheralite  $\text{CaTh}(\text{PO}_4)_2$ . Analysed monazite contains significant amounts of Th and U (in this study up to 18 wt% and 3 wt%, respectively) and neglectable amounts of common lead. This and the fact that diffusion of major and trace elements is very low makes it a useful tool not only to obtain precise age data but also information about the chemical and metamorphic history of the host rock (Parrish, 1990). Closure temperatures for Pb in naturally monazite is reported to be between 650 and 740 °C (Grove et al., 1999), experiments with synthetic monazite resulted in much higher temperatures (1150-1350 °C) (Cherniak et al., 2004). Loss of radiogenic lead produced by Th and U tends to be low in monazite and is neglectable for age calculations (Grove et al., 1999). The internal chemical zoning and texture of monazite can be complex. BSE pictures display dark and light patches within the monazites, mostly irregular, rare oscillatory or core-rim like arranged. They represent chemical zoning mainly controlled by Th and Y content. Y content ranges from 0.06 to 5.47 wt% replacing elements on the HREE<sup>3+</sup> sites, Th from 0.14 - 18.5 wt%, replacing REE<sup>3+</sup> sites (Williams et al., 2007).

The Y content in monazite is considered to reflect the whole rocks Y concentration – mainly influenced by the presence of garnet or xenotime, as they are the major Y reservoirs in metapelitic rocks (Bea et al., 1999). The implementation of Y in monazite during growth can therefore reflect the coexistence, absence, growth of garnet. One can assess the metamorphic stage in which the zone of the monazite grew by following the prograde garnet history of formation and breakdown. Prior to the formation of garnet, a growing monazite will display zones with high contents of Y. As garnet starts to form, Y is partitioned into the garnet. Monazite growing during this stage are depleted in Y. The Y liberated during garnet breakdown after peak metamorphism would lead again to Y enriched monazite zones (Bea et al., 1999; Pyle et al., 2001). Although several zones with Y

enrichment or depletion are present in every monazite, no correlation or trend with the obtained age data can be found. The Y content within one grain can vary with different absolute values for each sample. Therefore, each monazite had to be interpreted individually. Correlate Y zoning with garnet growth or breakdown and dating individual metamorphic stages is therefore difficult. Yttrium dispersion and range of absolute values for monazites in the matrix or as inclusion garnet is similar.

The monazites of this study clearly display mainly cheralite substitution with a small huttonite vector contribution (Figure 25), seen in the Th + Si + U vs. REE + Y + P plot (Figure 26). It is notably that no distinct trend can be observed whether the monazite is an inclusion in garnet or occurring in the matrix, nor any trend related to actual ages. However, the monazite chemistry of each sample tends to cluster occasionally, e.g. as shown by sample S4 in Figure 27 B. The incorporation of Ca and Si varies. Monazites in garnet tend to have slightly higher Si and Ca contents relative to Nd (representing LREE) and Y (representing HREE) content than in the matrix (Figure 27 A, B). LREEs display a negative trend with Y and Th (Figure 28 A, B) which can be explained by the similar behavior of Y and HREEs and the incorporation of Th by the cheralite substitution. Th and Y does not show any systematic behavior (Figure 28 C). HREE/LREE ratios plotted against age or Th does not show neither any significant correlation.

Typically, brighter BSE zones contain elevated Th contents while Y is enriched in darker ones. However, zones with elevated Y content can appear bright in the BSE image as well, depending on the varying Th and U content. The  $Y_2O_3$  vs.  $ThO_2$  contents are plotted in Figure 28 C. La and Nd, the most abundant LREEs in monazite cannot be related to the zoning as their content is relatively constant within one monazite grain. The absolute abundances for Ce, La and Nd vary between 32 - 24 wt%, 15 – 9 wt% and 15 – 8 wt%, respectively. An x-ray elemental distribution map for U, Th, Pb and Y for a monazite from sample S21 displays a core-rim relation, especially defined by the Y and Th content. Related zoning patterns not visible on a BSE image can be observed here, although this is not representative for most monazites. A Y enriched mantle relative to the core area is

surrounded by a Y depleted rim, negatively correlated with the Th content (Figure 30). Although this might indicate a growth history in presence or absence of garnet related to the Y content, a correlation between actual ages and these zones could not be achieved. EPMA analyses for monazites are shown in Table 11.

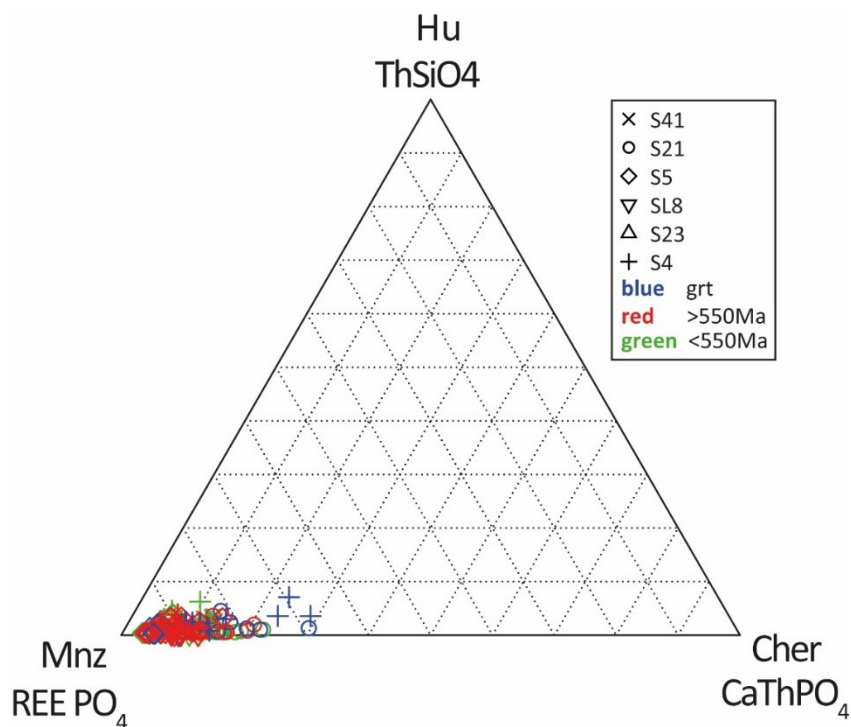


Figure 48: Ternary modal plot including the endmembers monazite, huttonite and cheralite. All samples are monazites although the cheralite substitution can be observed (e.g. S4).

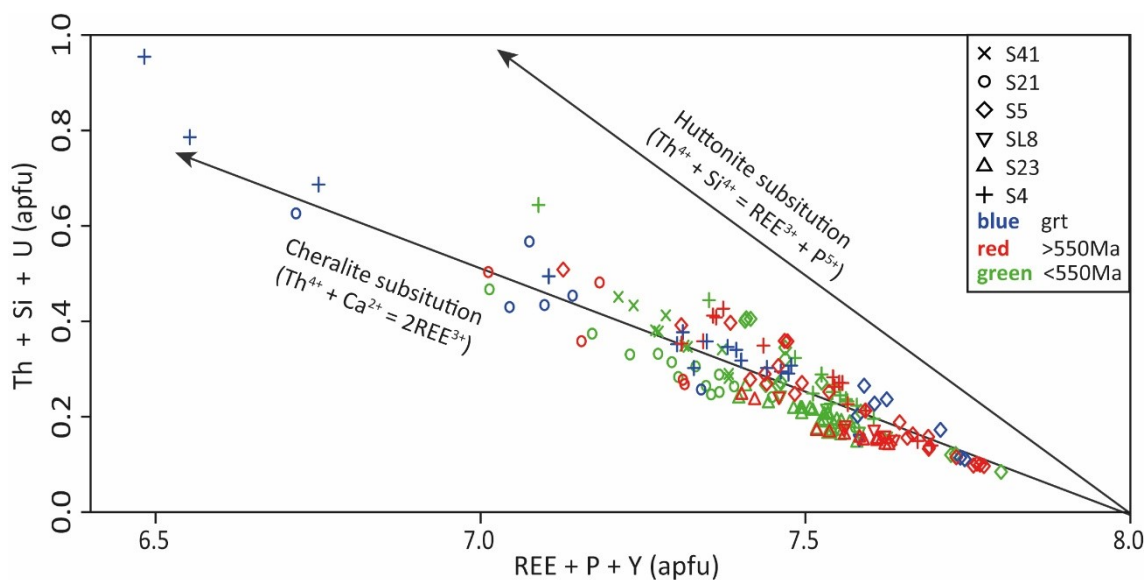


Figure 51: Plot illustrating the ratio of  $Th+Si+U/REE+P+Y$  representing the cheralite and huttonite substitution. Arrows indicate the respective substitution vector for cheralite and huttonite. All samples plot predominantly along the cheralite vector. Blue = monazites in garnet, red = age >550Ma, green = age <550Ma. In apfu.

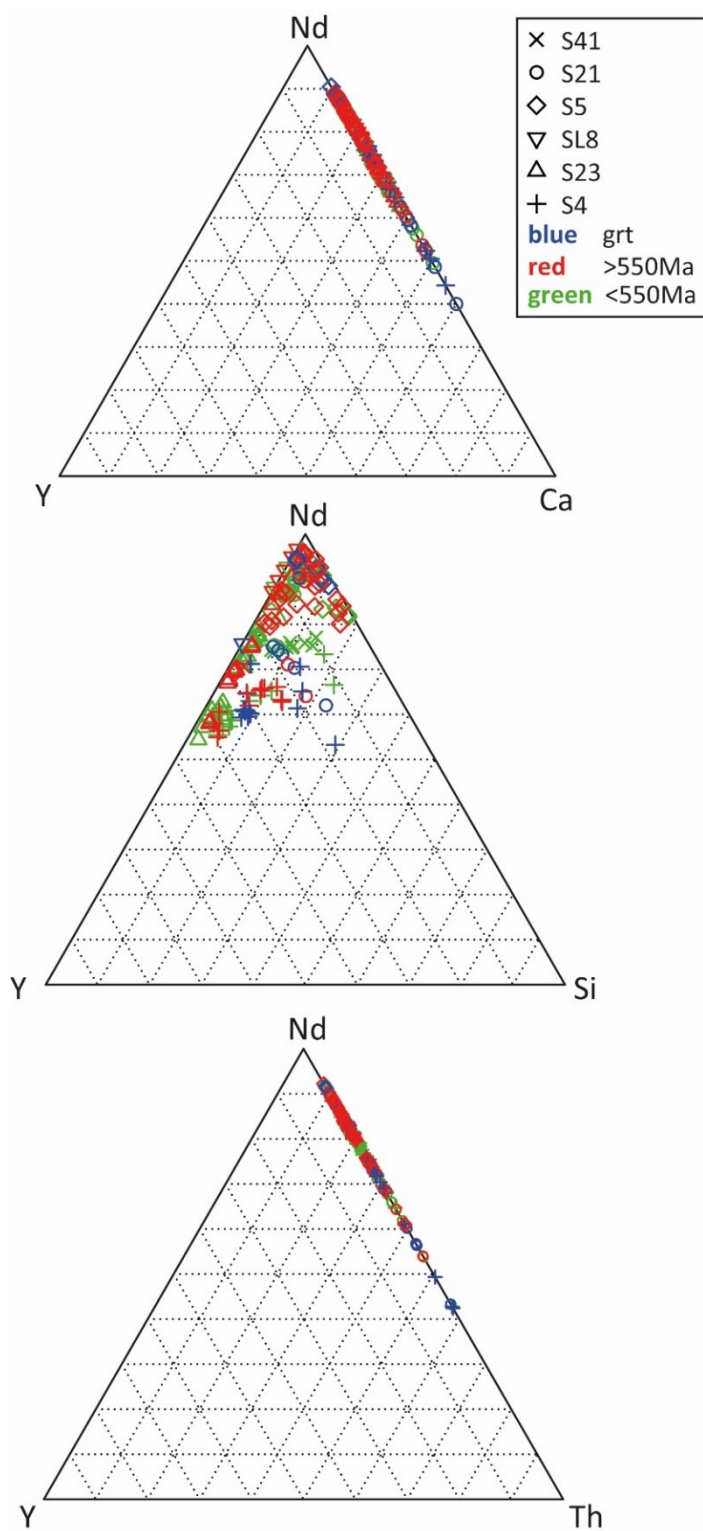


Figure 52: ternary modal plots for Y-Nd-Ca, Y-Nd-Si and Y-Nd-Th representing the cheralite and huttonite substitution. In apfu.

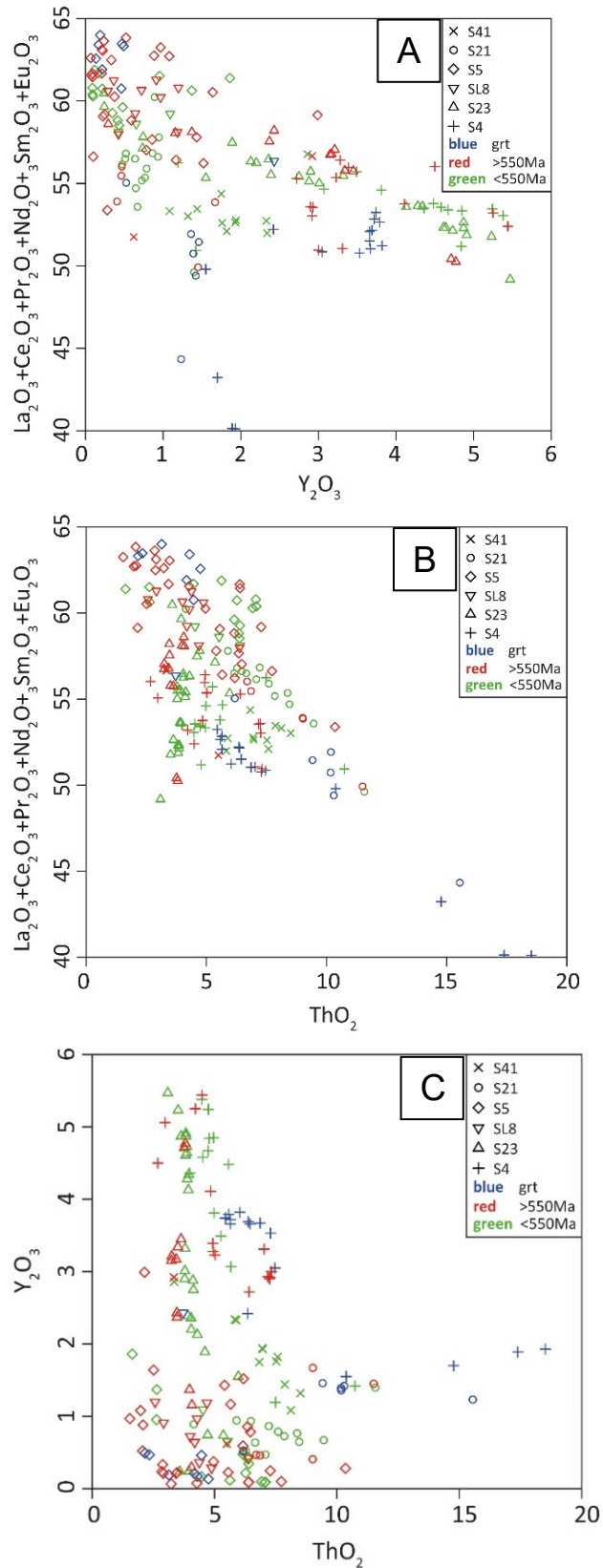


Figure 53: A & B.) LREEs plotted against Y and Th. A negative trend for Th and Y can be observed. C.) Y plotted against Th, indicating no distinct correlation between these two elements.

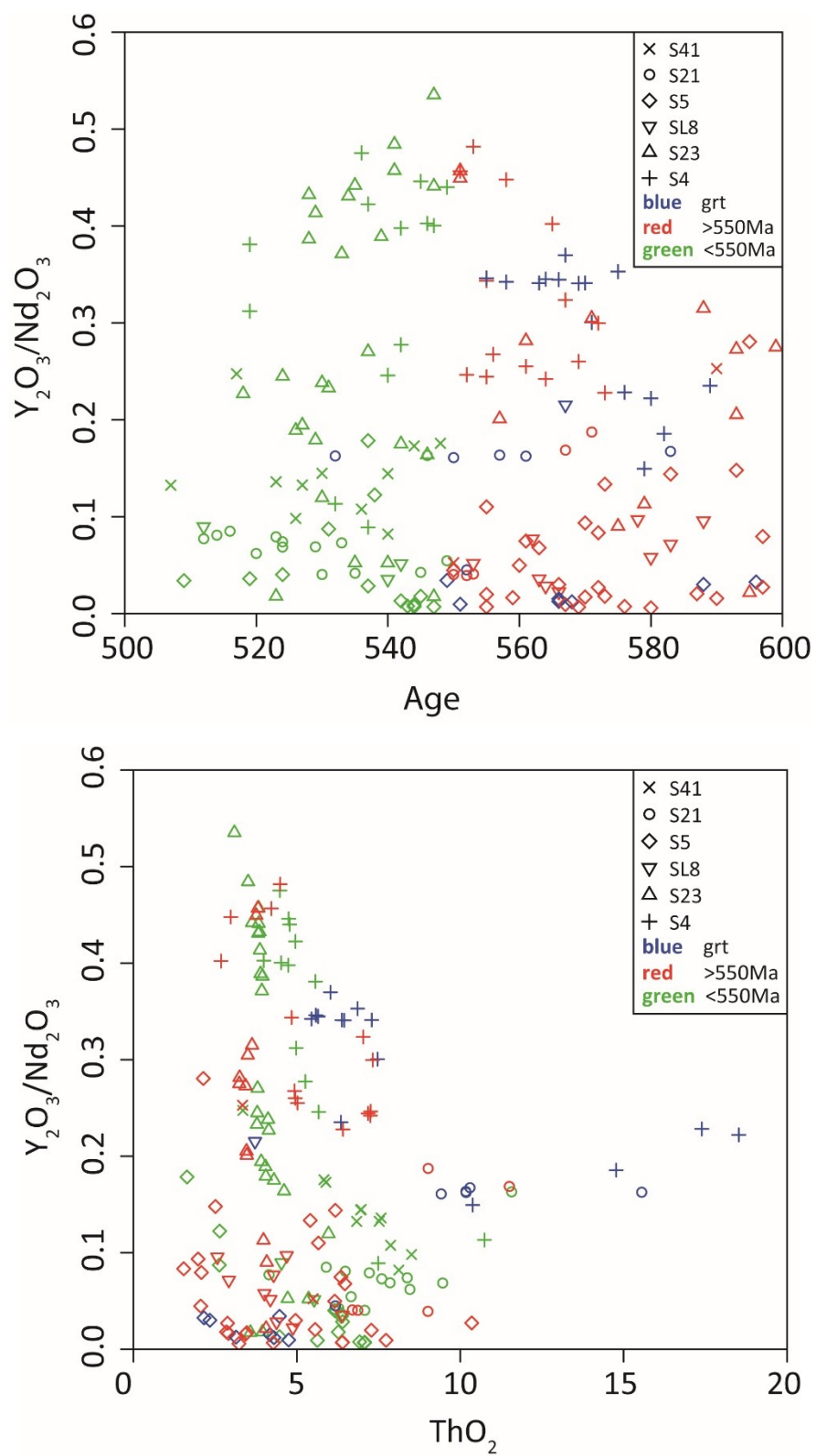


Figure 55: HREE/LREE ratio, represented by Y and Nd respectively, against age and Th.

Table 11: Representative analyses, age and error of selected monazites as inclusion in garnet and in the matrix, subdivided in &gt;550Ma and &lt;550Ma. In wt%.

	Sample	SiO <sub>2</sub>	Y <sub>2</sub> O <sub>3</sub>	P <sub>2</sub> O <sub>5</sub>	ThO <sub>2</sub>	CaO	La <sub>2</sub> O <sub>3</sub>	Ce <sub>2</sub> O <sub>3</sub>	Pr <sub>2</sub> O <sub>3</sub>	Nd <sub>2</sub> O <sub>3</sub>	Sm <sub>2</sub> O <sub>3</sub>	Gd <sub>2</sub> O <sub>3</sub>
<b>In garnet</b>	S4_mnz8_4	0.349	3.000	30.390	7.320	1.650	11.450	24.920	2.780	10.010	1.670	1.830
	S21_mnz4_4	0.479	1.450	30.440	11.500	2.630	12.710	24.990	2.570	8.600	0.851	0.678
	S21_mnz6_1	0.218	0.407	30.930	9.010	2.990	12.580	26.610	2.860	10.370	1.400	0.818
	S23_mnz2_2	0.166	4.710	31.080	3.760	1.990	10.570	24.330	2.680	10.480	2.130	2.040
<b>&gt;550Ma</b>	S4_mnz6_3	0.848	1.700	29.770	14.770	2.780	9.510	21.030	2.270	9.160	0.972	1.960
	S21_mnz2_1	0.253	1.420	30.400	10.300	2.990	12.510	24.810	2.470	8.480	0.938	0.661
	S4_mnz6_2	0.859	1.890	29.790	17.390	3.470	8.780	19.380	2.250	8.280	1.220	1.810
	S21_mnz1_2	1.109	1.360	29.080	10.180	1.900	13.820	26.130	2.570	8.370	0.800	0.685
<b>&lt;550Ma</b>	S41_mnz2_1	0.636	1.760	29.150	7.520	2.190	8.840	24.590	3.130	13.270	2.640	2.140
	S23_mnz3_3	0.181	4.340	31.270	3.950	1.290	11.160	25.770	2.960	11.230	2.240	2.200
	S21_mnz7_1	0.187	0.671	31.110	9.460	2.560	12.830	26.590	2.870	9.780	1.410	0.881
	SL8_mnz2_4	0.013	0.653	30.150	5.530	1.290	11.930	28.240	3.310	12.710	2.340	1.250

Table 12: Table 11 continued.

	Sample	FeO	Er2O3	Yb2O3	Dy2O3	PbO	UO2	Eu2O3	Lu2O3	SO3	Sum	Age	Error
<b>In gar- net</b>	S4_mnz8_4	0.109	0.137	0.039	0.912	0.265	1.110	0.128	0.029	0.000	98.097	<b>572</b>	13
	S21_mnz4_4	0.124	0.000	0.000	0.316	0.325	0.659	0.198	0.000	0.000	98.5206	<b>567</b>	10
	S21_mnz6_1	0.082	0.000	0.000	0.133	0.230	0.302	0.087	0.000	0.000	99.0273	<b>552</b>	14
	S23_mnz2_2	0.003	0.283	0.018	1.250	0.290	2.580	0.223	0.093	0.646	99.322	<b>551</b>	11
<b>&gt;550Ma</b>	S4_mnz6_3	0.457	0.010	0.000	0.731	0.408	0.597	0.284	0.000	0.000	97.2605	<b>582</b>	8
	S21_mnz2_1	0.053	0.067	0.000	0.281	0.306	0.667	0.195	0.000	0.000	96.8006	<b>583</b>	11
	S4_mnz6_2	0.281	0.099	0.000	0.771	0.485	0.823	0.226	0.232	0.000	98.0431	<b>576</b>	7
	S21_mnz1_2	0.137	0.050	0.000	0.267	0.294	0.703	0.237	0.038	0.000	97.7287	<b>561</b>	11
<b>&lt;550Ma</b>	S41_mnz2_1	0.034	0.012	0.000	0.658	0.175	0.133	0.136	0.071	1.020	98.1059	<b>527</b>	18
	S23_mnz3_3	0.000	0.202	0.000	1.170	0.178	1.210	0.249	0.044	0.146	99.7893	<b>528</b>	17
	S21_mnz7_1	0.039	0.000	0.000	0.194	0.241	0.462	0.099	0.000	0.000	99.3837	<b>524</b>	13
	SL8_mnz2_4	0.068	0.000	0.000	0.178	0.165	0.516	0.075	0.000	0.030	98.4602	<b>542</b>	19

## 6.4 Monazite Texture

Subdividing the zones after BSE color or rather Th content and correlate them with ages or LREE patterns with increasing Y does not show any trends or significant correlations. Patchy textures (e.g. Figure 32 C) are the result of replacement and intergrowth of the zones during prograde metamorphism, partial melting and retrograde reactions resulting in an irregular growth behavior of monazite (Hermann et al., 2006). Core-rim relations, in sense of older core and younger rim, can be distinguished in some cases although some difficulties have to be considered: 1.) the complex growth pattern of monazite can lead to delusive core-rim relations where an older rim encompass a younger core. A partially consumed monazite is overgrown by a younger rim not necessarily in a concentric pattern resulting in partially entangled younger rims by older cores, depending on the cut. This can lead to misinterpretations. 2.) The error range of single analyses can reach approximately  $\pm 25$  Ma. Therefore, core-rim relations with an age dispersion less than  $\sim 25$  Ma cannot be separated.

The monazites from this study area were subdivided in 4 groups according to their internal chemical zoning observed in BSE images as suggested by Wanniarachchi et al., (2016): (1) *oscillatory zoned*, (2) *inherited core bearing*, (3) *complexly zoned* and (4) *core rim zoned* (Figure 31 and Figure 32). Three types are documented throughout all samples, although monazites occurring as inclusion in garnet do not show complex zoning. (1) *Oscillatory zoned* monazites are not present in this study area which are usually considered to be of igneous origin. Core - rim relations like in sample S21 Mnz 8 (Sample S21 monazite grain 8) may be misleadingly taken for oscillatory zoning. (2) *Inherited core bearing* monazites have a sometimes euhedral, sometimes anhedral, occasionally Th rich core which has a sharp boundary to adjacent zones. As shown by Figure 31 A, the irregular shape of the core indicates a partial resorption of the primary monazite, contoured by later overgrowth of younger monazites. (3) *Complexly zoned* monazites are usually anhedral in shape and characterized by numerous patchy zones, in some cases framed by a Y poor rim as shown in Figure 31 B and Figure 32 B. They are absent in monazites which occur as inclusion in garnet. Obtained

ages from Y poor rims (with varying Th content) are not systematically younger than the other zones. (4) *Core-rim zoned* monazites display core-rim arranged zones with varying Y and Th distribution. Although the majority shows a decreasing age from core to rim, complex monazite intergrowth may cause older ages towards the rim Figure 32 B. Therefore, a complexly zoned monazite can misleadingly be taken for a core-rim zoned monazite. No trend or systematic correlation could be observed for Y or Th enrichment/depletion for certain age domains. Core-rim zoned monazites show a smaller chemical variation compared to complexly zoned or inherited core bearing monazites. Some monazites are almost homogeneous, showing only one or two chemical zones, are small (30-50  $\mu\text{m}$ ) and occur only as inclusions in garnet (Figure 31 C and Figure 32 C). They are significantly older (600 - 1100 Ma) and can be correlated with zircon crystallization ages in the study area and are most likely inherited (Hölzl et al., 1994; Kitano et al., 2018). Chemical composition and zoning of monazites from each analyzed sample along with their occurrence in the mineral assembly is described in detail below, for a detailed discussion of obtained ages see the chapter 6.6.

Monazites and their age have been subdivided into 2 groups according to their textural occurrence in the sample: 1.) monazite occurs as inclusion in subhedral to xenomorphic poikilitic Garnet (in core and outer core) along with inclusions of zircon, xenotime, apatite, magnetite, spinel, quartz, plagioclase, sillimanite and +/- pyrite. Due to their small size, narrow zoning, and especially their rare occurrence, only 13 suitable grains in 4 samples (S4, S5, S21, SL8) could be found and measured. 2.) monazite is a common constituent within a cordierite/quartz or plagioclase/k-feldspar matrix and occurs as inclusion in cordierite and biotite as well as along garnet rims (Figure 33). Obtained ages were separated into two clusters: (1) older than 550 Ma prevailing in monazites from garnet inclusions and (2) younger than 550 Ma, mainly found in matrix monazites. See chapter 6.6 for further discussion.

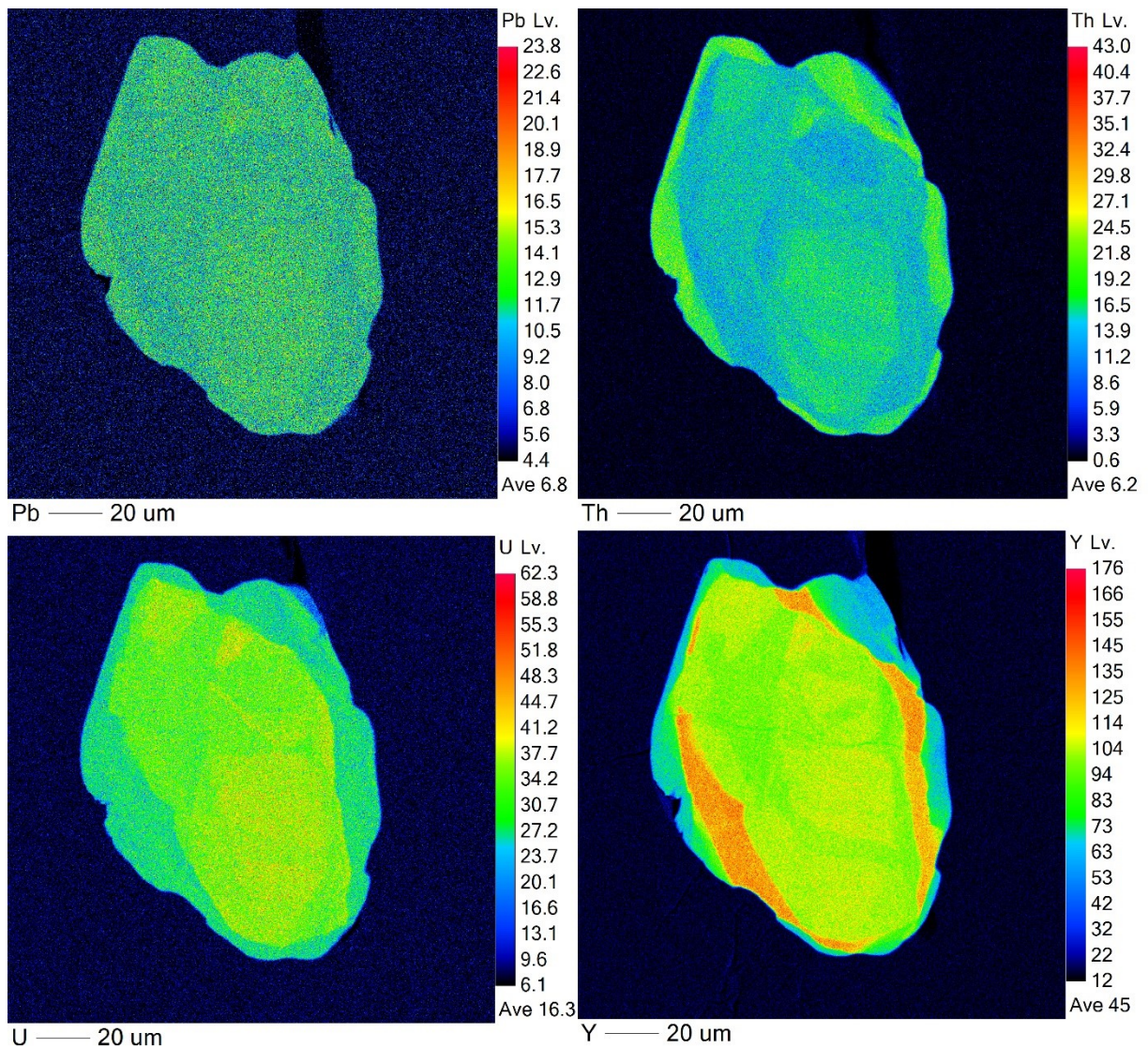


Figure 56: X-ray elemental distribution map for Pb, Th, U and Y of a matrix monazite from sample S21. This monazite display a core-rim like internal texture with a Y enriched rich mantle compare to the core area and a Y poor rim. The Th content decreases with decreasing Y as shown especially at the rim. This pattern is not common for monazites of this study (Figure 27 C). U enrichment in the core correlates with the suggested core-rim structure. Pb shows only weak zoning but correlates positive with the Th content.

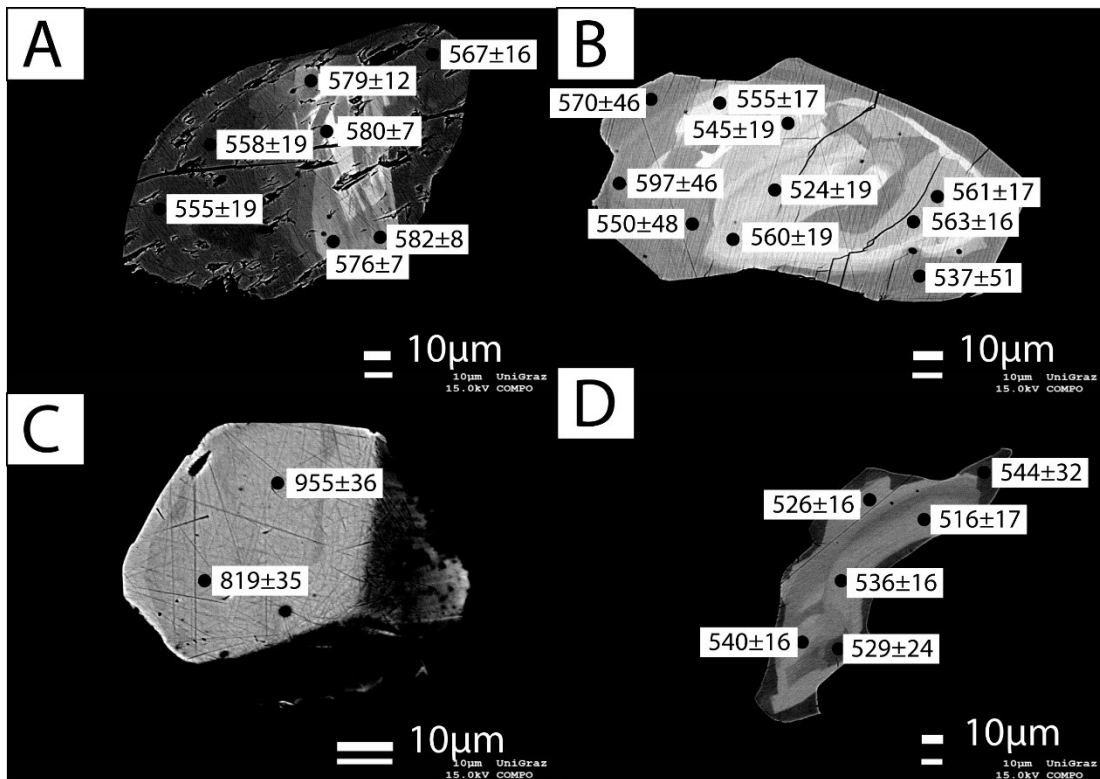


Figure 59: BSE images of monazites with analyzed spots and their respective age and error in Ma. A.) inherited core bearing monazite with a bright Th rich core which tends to be older than Th poor, younger domains (S4 mnz 6). Inclusion in garnet. B.) Core-rim zoned monazite, displaying younger core domains and older, slightly Y and Th poorer rim domains. This inverse sequence let suggest a complex garnet growth as mentioned in the text. (S5 Mnz 5) C.) Almost completely homogenous monazite with a weak zoning. This monazites pre-dates the pan-African orogeny. Inclusion in garnet (S4 mnz 3). D.) core-rim zoned monazite displaying an age range within the error. Dark rim represents Y poorer chemistry (S41 mnz 3).

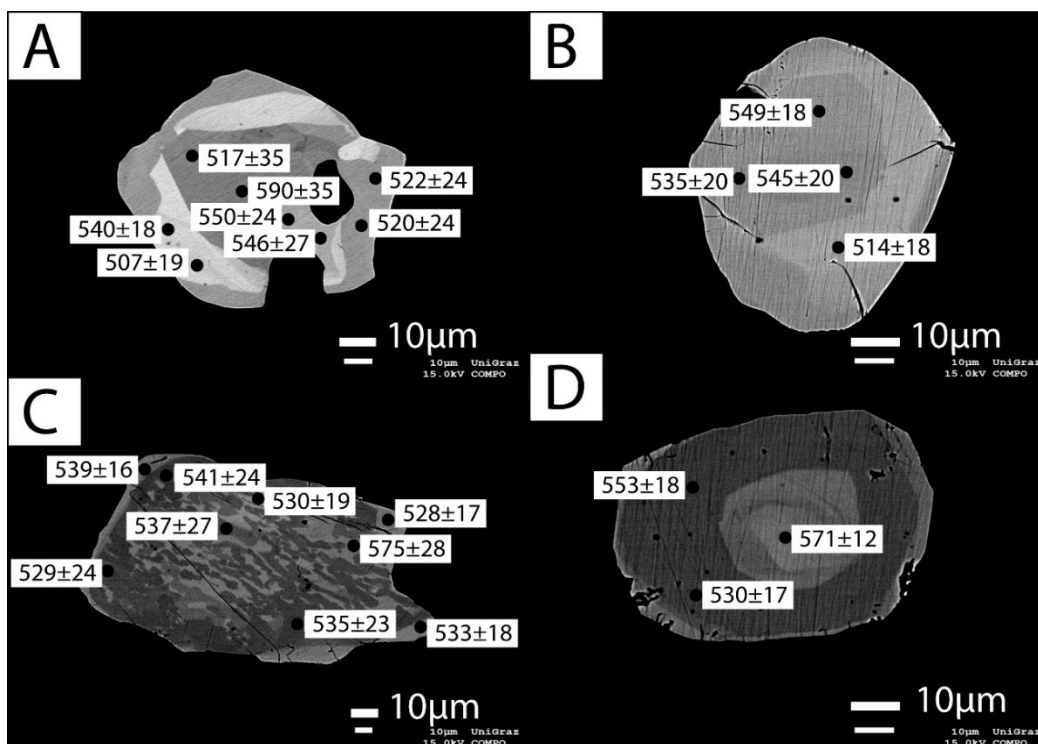


Figure 60: BSE images of monazites with analyzed spots and their respective age and error in Ma. A.) Core rim zoned monazite (S41 mnz 1). B.) Almost homogeneous monazite with weak chemical zoning and similar ages in each domain (S21 mnz 9). Inclusion in garnet. C.) Complexly zoned monazite with a slight Th rich rim (S23 mnz 3.) D.) core rim zoned monazite (S21 mnz 8).

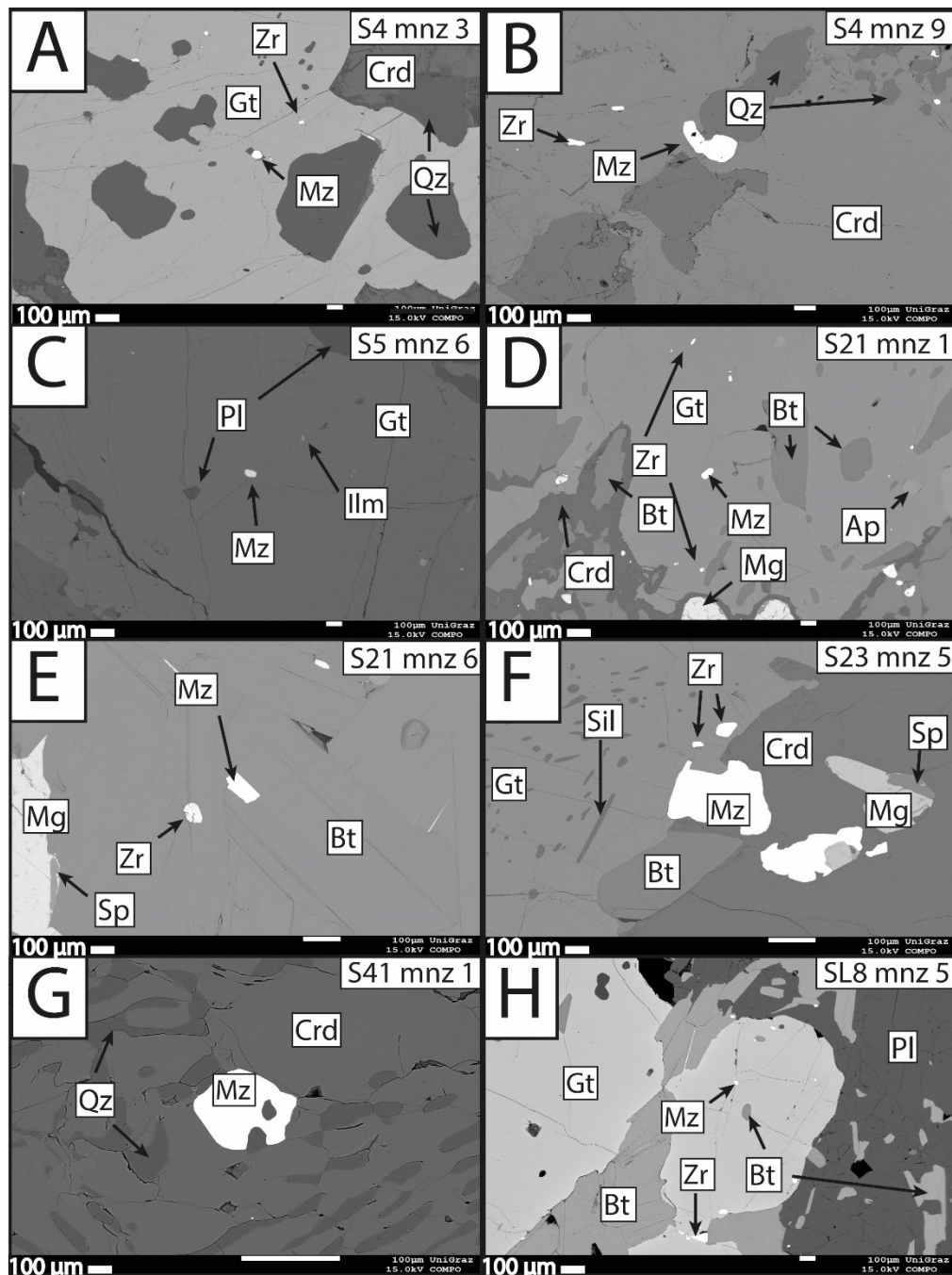


Figure 63: BSE images of different types of monazites. A.) Monazite inclusion in symplectitic garnet along with quartz and zircon, surrounded by cordierite (sample S4 mnz 3). B.) Monazite in a cordierite-quartz matrix (sample S4 mnz 9). C.) Monazite inclusion in garnet along with small amounts of plagioclase and ilmenite (sample S5 mnz 6). D.) Monazite inclusion in symplectitic and poikiloblastic garnet which displays a thin cordierite corona. Biotite occurs in the corona along with magnetite with spinel intergrowth or as inclusion in the garnet, along with zircon and apatite (sample S21 mnz 1). E.) Monazite and Zircon inclusion in Biotite, adjacent to magnetite with spinel intergrowth (sample S21 mnz 6). F.) Monazite at the rim of a poikiloblastic and symplectitic garnet along with cordierite, biotite and magnetite with spinel intergrowth (sample S23 mnz 5). G.) Monazite in a matrix which consists of quartz and cordierite intergrowth (sample S41 mnz 1). G.) Monazite inclusion in garnet along with biotite and zircon surrounded by biotite and plagioclase (sample SL8 mnz 5). Mineral abbreviations: Gt=garnet, Bt=biotite, Crd=cordierite, Pl=plagioclase, Kf=k-feldspar, Mg=magnetite, Sp=spinel, Mz=monazite, Zr=zircon

## 6.5 Description of Monazite Bearing Samples

### 6.5.1 Sample S4

Sample S4 is a felsic leucosome with large symplectitic garnet porphyroblasts. Garnet size reaches up to 1 cm with an advanced stage of garnet breakdown. Sillimanite inclusions are observed in the mantle while ilmenite, quartz, monazite, zircon and small amounts of plagioclase and cordierite seem arbitrarily distributed within the garnet grain. The matrix consists of large (5 mm) cordierite, quartz and feldspars. K-feldspar and plagioclase occur mainly as perthites, anti-perthite and mesoperthite. Finer grained cordierite with quartz intergrowth occurs around garnet and in melt textures, together with plagioclase and biotite. Monazites occur as inclusions in garnet, cordierite, at garnet rims and within the cordierite-quartz matrix ranging in shape from euhedral to xenomorph. Ten monazite grains between 50 and 150  $\mu\text{m}$  in size were analyzed with at least 3 to 9 spots on each grain.

**Monazite as inclusion in garnet:** Grains S4 mnz 1-3 are euhedral, concentric zoned monazites within a xeno- to hyp-idioblastic garnet which occur together with zircon, sillimanite, quartz and  $\pm$  xenotime (e.g. Figure 33 A). They show unusual old ages compared to all other monazites ranging from 955 Ma in the monazite core and significantly younger ages from 819 Ma to 641 Ma at the rim (e.g. Figure 31 C). Yttrium content varies from the Y richer core to the Y poorer rim (from 4.23 wt% to 1.92 wt%), respectively. These monazites were more unstable under the 200 nA electron beam resulting in a higher analytical error compared to all other analyses. Grains S4 mnz 5-7 are hyp-idioblastic and more complex zoned and are found together with sillimanite, zircon and quartz within garnet or within the former garnet rim which is now a quartz cordierite corona around the remaining garnet grain. Rim zones have lower Y contents compared to monazite core compositions. Grain S4 mnz 6 shows very fine complex zoning with sharp boundaries with a very Th rich (16.27 wt%) core.

**Monazites within the matrix:** These monazites are subhedral in shape, complexly zoned within a cordierite-quartz (e.g. (e.g. Figure 33 B) or plagioclase-k-feldspar matrix, except grain S4 mnz 8 with a Th rich inherited core which yield

ages >680 Ma. Due to the complex zoning, a core/rim relationship is not developed. A correlation between the Y and Th content and a particular age is not given except for significant older, high Th bearing inherited cores.

### 6.5.2 *Sample S5*

Sample S5 is a rather mafic granulite with clear visible migmatitic textures. It contains large sub-anhedral poikiloblastic garnet porphyroblasts (~5 mm) with biotite, plagioclase, k-feldspar, ilmenite, apatite, monazite and zircon inclusions, mainly in the core and mantle. Smaller euhedral garnets display the same inclusions only at the central parts of the core, indicating more than one generation of garnet growth. Major parts of the matrix consist of cordierite and biotite as product of garnet breakdown, along with perthitic/anti-perthitic plagioclase/k-feldspar and quartz. The grain size differs from micron to mm size, depending on the amount of garnet breakdown and degree of melting. Myrmekitic textures and “fibrous” intergrowth of cordierite and quartz in presence of biotite can be found commonly within the matrix. Ilmenite is primarily found in garnet core and mantle and is only minor represented in the matrix, along with magnetite. Spinel occurs not only intergrown with magnetite but also as anhedral grain conglomerates within symplectites, which can only be observed in sample S5. Subhedral to anhedral monazites occur as inclusions in garnet, biotite and in a cordierite-quartz or plagioclase-feldspar matrix.

**Monazite as inclusion in garnet:** the three monazite grains S5 mnz 6, 7 and 9 which were analysed are around 100 µm in size, euhedral with a concentric to complex zoning in the core of hyp-idioblastic garnet (e.g. Figure 33 C). Biotite, plagioclase, apatite, ilmenite and zircon occur as inclusions in the garnet core but are usually not in direct contact with the monazite. Monazites show a Th richer core and a Th rich and Y poor rim domain. Very Th rich rims and ages >600 Ma in grain S5 mnz 6 suggests that the alleged rim is an inherited core. Yttrium content in general is low (<1.12 wt%) while Th contents reach up to 9 wt%.

**Monazite within the matrix:** six euhedral to anhedral monazites with complex to concentric zoning. Th rich, oscillatory arranged domains do not display younger ages towards the rim. There is neither a significant chemical nor an age difference

between monazite which occur as inclusion in biotite, in a cordierite-quartz-plagioclase matrix or at a garnet rim.

### 6.5.3 *Sample S21*

Sample S21 exhibit large amounts of biotite and garnet. Garnet occurs as subhedral or anhedral up to 2 mm large poikilitic porphyroblasts. Biotite, k-feldspar, plagioclase, apatite, ilmenite occur as large inclusions in garnet. Sillimanite is rarely observed. All garnets show incipient decomposition by a ~50  $\mu\text{m}$  wide cordierite corona (Figure 33 D), not only at the garnet rim but also around magnetite and biotite inclusions. The matrix consists of anti-perthitic plagioclase, k-feldspar and quartz. Large abundances of biotite are concentrated around decomposing garnet, with monazite and zircon inclusions. Cordierite is restricted as corona around garnet. In the matrix magnetite with spinel intergrowth and ilmenite are main accessory phases with minor amounts of apatite, monazite, pyrite and zircon.

**Monazite as inclusion in garnet:** three 50-100  $\mu\text{m}$  large subhedral to euhedral monazites occur in core and outer core of a poikilitic subhedral garnet along with biotite, apatite, pyrite, zircon, magnetite (e.g. (e.g. Figure 33 D). While one monazite is more complex zoned with a varying Th content between 5 and 15.7 wt%, the other two grains represent a homogenous chemistry, with approximately constant Th and Y content throughout the grain. Although no clear differences between the monazite core and rim can be recognized, it has to be mentioned that younger ages occur always nearer to the rim.

**Monazite within the matrix:** six concentric to oscillatory zoned subhedral monazites, around 100  $\mu\text{m}$  in diameter occur as inclusion in biotite along with zircon and apatite (Figure 33 E), around garnet symplectites, in a cordierite matrix in contact with apatite and in a plagioclase-biotite-k-feldspar matrix. The zoning pattern shows sections up to 20  $\mu\text{m}$  in diameter where Y and Th vary around 1 and 5 wt%, respectively. The Th content shows a weak negative correlation with decreasing age, whereas Y increases with decreasing Th.

#### 6.5.4 *Sample S23*

Sample S23 is a felsic migmatitic granulite which contains few and small anhedral to subhedral garnet porphyroblasts. Most of the garnet is already decomposed and surrounded by extensive cordierite-magnetite-biotite symplectites. Biotite, quartz, apatite, ilmenite, sillimanite and zircon occur as inclusion in garnet. A distinct core-rim relation in monazite grains is not given, only sillimanite is restricted to the garnet mantle. The matrix consists of up to 3mm large cordierite along with plagioclase, k-feldspar and quartz. Myrmekitic textures can be observed throughout the sample with quartz/cordierite and plagioclase intergrowth. Biotite occurs in rather small flakes around decomposed garnet but is less abundant than e.g. in sample S5 or S21. Magnetite with spinel but also rare corundum intergrowth as product of the garnet breakdown is frequently distributed around symplectites. Accessory minerals like ilmenite, pyrite, zircon and  $\pm$  xenotime occur in the matrix or as biotite inclusion.

**Monazites within the matrix:** five monazites grains with 100-200  $\mu\text{m}$  in diameter and a subhedral to anhedral shape were measured, with a variety of internal textures. A.) In a cordierite-quartz matrix displaying extensive melt textures monazites have distinct internal core-rim zones and high Y contents (3.6 – 4.3 wt%) and a moderate but rather homogenous Th content (3.7 – 4.3 wt%) (e.g. grain S23 mnz3). B.) S23 mnz 1, 4 and 5 occur at garnet rims with magnetite, spinel together with cordierite (e.g. Figure 33 F). They show a complex zoning with increasing Y and decreasing Th contents. C.) In a quartz-plagioclase matrix in contact with apatite, S23 mnz 3 shows a very complex zoning with narrow domains encircled by Y rich annuli.

#### 6.5.5 *Sample S41*

Sample S41 represents a migmatitic cordierite and orthopyroxene bearing gneiss. Only small amounts of xenomorphic garnet are present and no monazites as inclusions in garnet can be observed. The homogeneous equigranular matrix consists of cordierite, plagioclase/k-feldspar, anti-perthite/perthite and quartz. Orthopyroxene occurs as small altered grains (0.5 mm) in the matrix. Melt textures like myrmekites can be observed throughout the sample. Magnetite with spinel

intergrowth, sillimanite, ilmenite, monazite and zircon are the accessory minerals in decreasing abundance.

**Monazite within the matrix:** Monazites (S41 mnz 1 and 3) occur in a cordierite-quartz matrix (e.g. Figure 33 G), show a core – rim like zoning, have a subhedral to anhedral shape and show a wide range in Th (2.9 - 7.1 wt%) and Y (0.5 - 2.5 wt%) content. In contrast, grain S41 mnz 2 is an euhedral, chemical homogenous monazite in a plagioclase-k-feldspar matrix in contact with magnetite.

#### 6.5.6 *Sample SL8*

Sample SL8 contains large (~3 mm), partial elongated subhedral garnet porphyroblasts with plagioclase, quartz, sillimanite, biotite, magnetite, hercynitic spinel, zircon and monazite inclusions. Most inclusions are restricted to the core and in contrast but compared other samples sillimanite is found in primary in the core and only minor amounts in the mantle or rim of the garnet. The matrix is dominated by biotite and cordierite as product of garnet breakdown along with plagioclase and quartz. Additionally, cordierite can be found as thin corona (~50 µm) around garnet together with large abundances of biotite. About 30 percent of the matrix is covered by extensive melt textures with plagioclase-quartz-biotite intergrowth and myrmekites. Ilmenite, magnetite with spinel exsolution, monazite, apatite and zircon can be found as accessory minerals in the matrix.

**Monazite as inclusion in garnet:** One small (~20 µm diameter) homogeneous grain with moderate Y and Th content (1.9 and 3.2 wt%, respectively) as inclusion in garnet was suitable for EPMA analyses (sample SL8 mnz 5 - Figure 33 H).

**Monazites within the matrix:** Three subhedral to anhedral monazites (SL8 mnz 1, 2 and 3) occurring as inclusions in biotite along with zircon, plagioclase and close to garnet rims were measured. They show large scale zoning which tend to become Y poorer (from ~ 1.2 to 0.2 wt%) and Th richer (from 2.2 to 5.6 wt%) towards the rim.

## 6.6 Age Results

Monazites as inclusions in garnet and in the matrix display different weighted mean ages. Internal age variation recorded in each monazite can be up to 50 Ma, in inherited core bearing textures 100 Ma, in the average ~30 Ma. Almost homogenized monazites can show age ranges of <10 Ma or <10 Ma, which falls within the error range. Typical errors in the range of up to  $\pm 35$  Ma per single spot measurement makes it difficult to correlate age trends with chemical zoning, e.g. Y enrichment or depletion to absolute ages within one grain. Therefore, deciphering complex growth pattern and define core-rim relations is limited to monazites with small error ranges and sufficient age differences.

Taking this into account, all obtained ages were subdivided in 3 age clusters: 1.) monazites in garnet results in a significant older weighted mean age compared to results from matrix monazites:  $572 \pm 3$  Ma. Matrix monazites show a large age distribution, from ~510 – 590 Ma. Therefore, these analyses were subdivided in 2.) a  $>550$  Ma ( $565 \pm 3$  Ma) and 3.) a  $<550$  Ma weighted mean cluster ( $534 \pm 2$  Ma) (Figure 34).

Few ages older than 600 Ma can be found in all types of monazite. They are interpreted to represent detrital monazite relicts. Hence, the meaning of the age is difficult to interpret but is clearly unrelated to the Pan-African metamorphic overprints. Weighted means are shown in Figure 34, weighted means for each sample are listed in

Table 13.

*Table 13: weighted means for each sample, including ages  $>600$ Ma if present. X = did not occur in this sample.*

<b>Sample</b>	<b>In Garnet</b>	<b><math>&gt;550</math>Ma</b>	<b><math>&lt;550</math>Ma</b>	<b><math>&gt;600</math> Ma</b>
S4	$575 \pm 3$	$563 \pm 6$	$535 \pm 24$	$685 \pm 12 / 641 \pm 19$
<b>S5</b>	$567 \pm 8$	$569 \pm 4$	$538 \pm 7$	$610 \pm 9$
S21	$553 \pm 6$	$562 \pm 8$	$530 \pm 4$	x
<b>S23</b>	x	$564 \pm 7$	$536 \pm 4$	$642 \pm 25 / 600 \pm 28$
S41	x	$563 \pm 10$	$536 \pm 6$	x
<b>SL8</b>	$567 \pm 24$	$568 \pm 10$	$533 \pm 7$	$605 \pm 35$

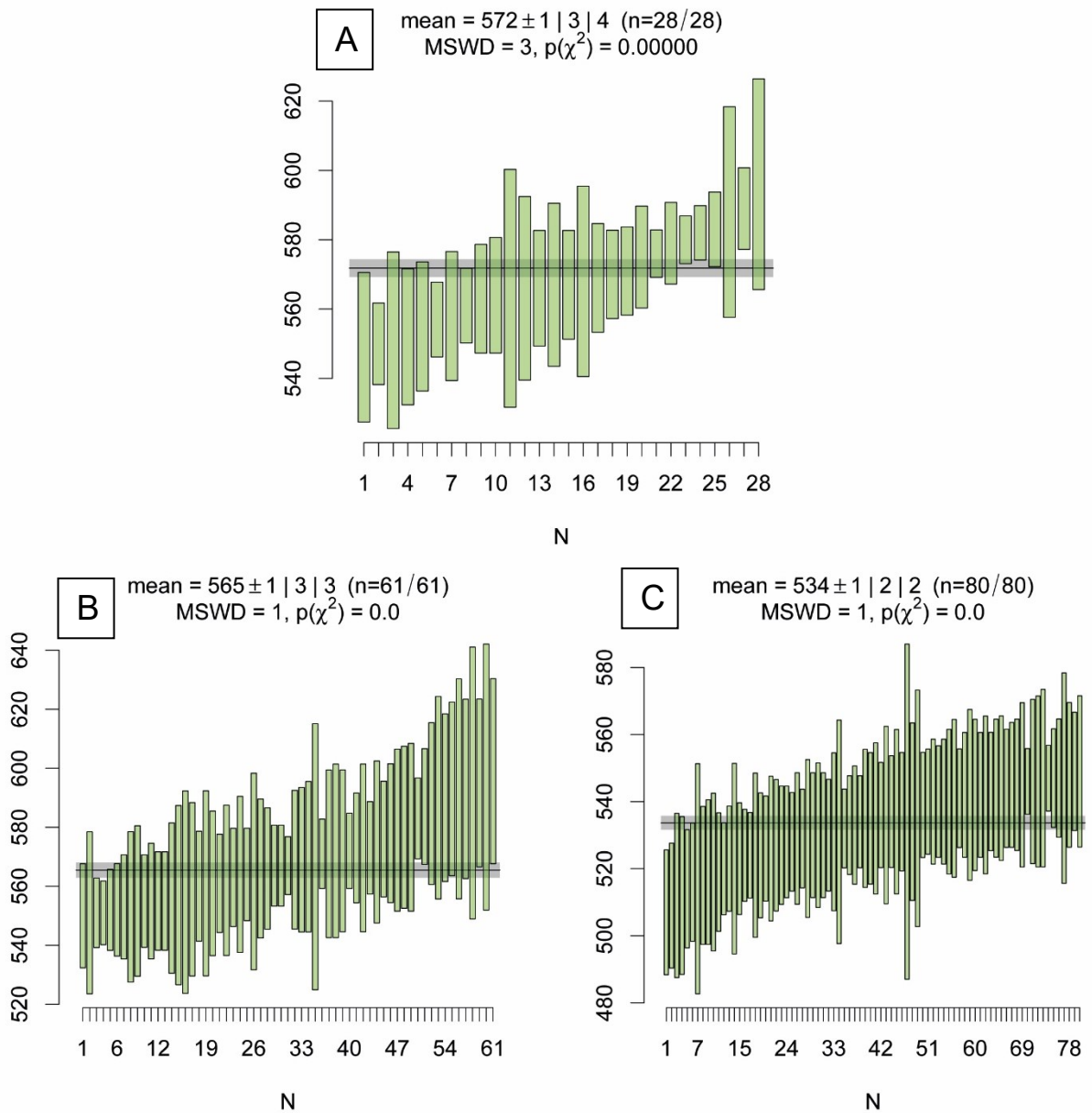


Figure 66: weighted means for all 3 age groups. A.) weighted mean for monazite as garnet inclusion. B.) weighted means for >550Ma in the matrix. C.) weighted means for <550 Ma in the matrix.

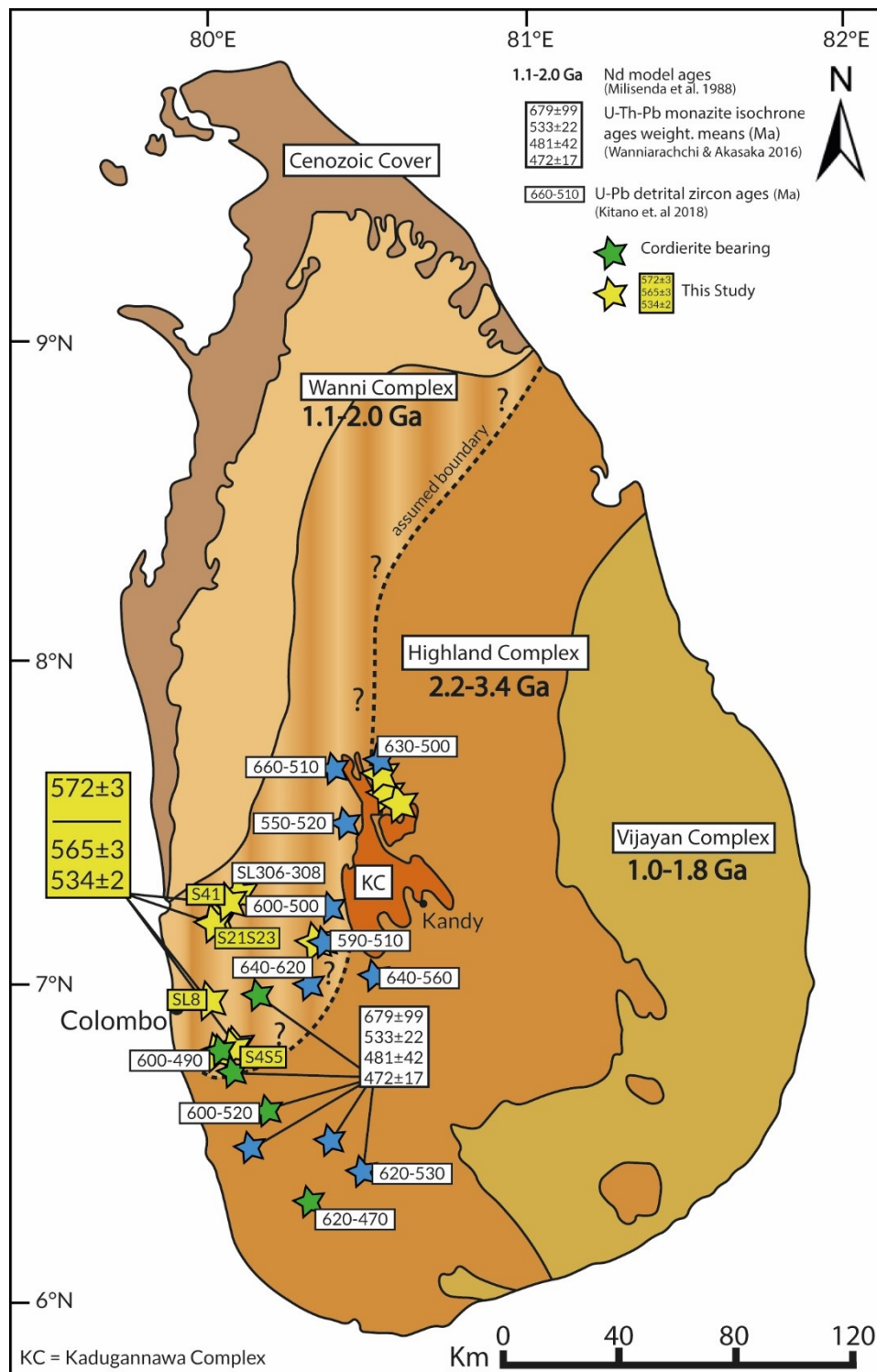


Figure 67: Locations of previous and in this study dated samples in the HC/WC boundary area with their respective U-Th-Pb monazite and U-Pb detrital zircon ages in Ma. Green stars mark cordierite bearing samples. Yellow stars mark samples from this study. The yellow box represents weighted mean age results from this study. Map after Cooray 1994.

## 7. Estimates by Conventional Thermobarometry

### 7.1 Metamorphic Evolution

Two different P-T paths for the southern area of the Highland Complex - Wannai Complex boundary were postulated in the past. Peak conditions of 650-850 °C and 5-7 kbar followed by a decrease of both temperature and pressure were suggested by Hiroi et al., (1994). Dharmapriya et al. (2014) on the other hand suggested peak metamorphism at 7.5 - 8.5 kbar and 870 - 900 °C followed by isobaric cooling and isothermal decompression, derived from khondalites south of Colombo. To constrain the metamorphic P-T conditions, both conventional geothermobarometers and pseudosection modelling were applied on selected samples including those on which Chemical Th-U-Pb monazite dating was performed.

### 7.2 Garnet-Cordierite Thermometer

The garnet-cordierite Fe-Mg exchange reaction ( $1/3 \text{Fe}_3\text{Al}_2\text{Si}_3\text{O}_8 + 1/2\text{Mg}_2\text{Al}_4\text{Si}_5\text{O}_{18} = 1/3 \text{Mg}_3\text{Al}_2\text{Si}_3\text{O}_{12} + 1/2 \text{Fe}_2\text{Al}_4\text{Si}_5\text{O}_{18}$ ) was used as thermometer and performed on garnet core composition or mantle/rim compositions not affected by retrograde diffusional zoning and large cordierites from the matrix. Activities were calculated using AX62 with activity and mixing models for both garnet and cordierite from White et al. (2014) at 5 - 7 kbar and 750 °C. The single reaction was calculated using "friendly" from the PerpleX 6.8.6 suite together with Holland and Powell 6.2 dataset (T. J. B. Holland et al., 2011). The mineral chemistry for both types of garnet and cordierites ranges from  $X_{\text{GrtMg}}$  0.2 - 0.37,  $X_{\text{GrtFe}}$  0.52-0.7,  $X_{\text{CrdMg}}$  0.7 - 0.86,  $X_{\text{CrdFe}}$  0.12 - 0.3. Except the minor zonation of garnets and retrograde diffusional zoning patterns, no significant trend of XMg and XFe distribution in both types of cordierite is notable. Results range from 780°C – 820°C and are listed in Table 14.

### 7.3 Two Feldspar Thermometry

Two feldspar thermometry after (Benisek et al., 2004) was performed additionally on suitable samples, mostly using perthites. The original K-feldspar composition was calculated by reintegrating host and lamellae modal ratio and chemical composition. The majority of samples show rather mesoperthitic textures with approximately 50/50 host-lamellae ratios which lead to clearly definable ternary feldspar compositions when reintegrated and cause numerical instabilities during the calculation. Additionally, matrix plagioclase is not present in every sample which furthermore limits suitable samples. Calculations were performed with pressure conditions between 5 and 8 kbar according to barometric calculations. Obtained temperatures range from 800 - 900 °C.

### 7.4 Ti in Biotite Thermometer

The Ti in biotite thermometer after Henry et al. (2005) was applied, based on the temperature and  $X_{Mg}$  dependent content of Ti in biotite. It is calibrated for graphitic low to medium pressure (4 – 6 kbar) peraluminous metapelites with an improving accuracy for temperatures >700 °C ( $\pm 25$ ). As required, the presence of ilmenite as Ti-saturating phase was ensured, retrogressed biotite (“green” Ti-poor zones) was avoided. Biotite replacing garnet or cordierite show higher  $X_{Mg}$  and lower Ti values compared biotite not related to this reaction, which may lead to underestimated temperatures (Ikeda, 1998). Graphite was not present in all samples. Its absence can lead to moderate underestimations with larger standard deviations (Henry et al., 2005) – results from samples without graphite have to be interpreted carefully. Results range from 750-830 °C and are listed for each sample in Table 14.

### 7.5 GASP Barometer

The garnet-alumosilicate-quartz-plagioclase barometer which is based on the reaction  $\text{anorthite} = \text{grossular} + 2 \text{ sillimanite} + \text{quartz}$  (Koziol et al., 1988) was applied to the samples listed in Table 14. The presence of plagioclase and quartz



Table 14: Results of the conventional geothermobarometry.

Sample	Grt-Crd (°C)	Fsp- Thermo	Ti in Bt (°C) ± 25	GASP (kbar)	TWQ
<b>S4</b>	800-820	-	780-790	7.5-8.5	7kbar/750°C
<b>S5</b>	790-810	-	810-820	4-6	7kbar/750°C
<b>S21</b>	780-800	-	780-800	5.5-6.5	7kbar/730°C
<b>S23</b>	-	-	810	5-6	7kbar/750°C
<b>S41</b>	800-820	900°C	815	4.5-6	8kbar/950°C
<b>S42</b>	890-920	-	800-810	6.5-8	-
<b>SL8</b>	890-900	-	790-800	5-6	7kbar/800°C

## 8. P-T Pseudosection Modelling

### 8.1 Introduction

Pseudosections in the MnO-Na<sub>2</sub>O-CaO-K<sub>2</sub>O-FeO-MgO-Al<sub>2</sub>O<sub>3</sub>-SiO<sub>2</sub>-H<sub>2</sub>O-TiO<sub>2</sub>-O<sub>2</sub> (MnNCKFMASHTO) system were computed using PerpleX Version 6.8.6. and the Holland and Powell 6.2. dataset (T. J. B. Holland et al., 2011). Chemistry for selected basic and acidic samples with the mineral assembly garnet + biotite + plagioclase + k-feldspar + cordierite + spinel + quartz + magnetite ± sillimanite ± ilmenite, apatite as accessory minerals and clear evident melt textures are given in table 10-15. Following solid-solution models were used: clinopyroxene (Holland, 2001), melt (White et al., 2014b), spinel (White et al., 2002), garnet (White et al., 2014b) orthopyroxene (White et al., 2014b) Mica (White et al., 2014b), chloritoid (White et al., 2014b), staurolite (White et al., 2014b), biotite (White et al., 2014b), cordierite (White et al., 2014b) feldspar (T. Holland et al., 2003) ilmenite (White, Powell and Holland 2014) and sapphirine (Wheller & Powell 2014). H<sub>2</sub>O content was assumed individually for each sample and 15% Fe<sup>3+</sup> of Fe<sub>Total</sub> was assumed according to petrographical observations. Compositional isopleths and isomodes for garnet, cordierite, biotite, plagioclase and melt were calculated with Werami. Due to the non-implementation of ZnO in the MnNCKFMASHT system, the stability field of spinel does not match petrographical observations. According to microprobe analysis, spinel contains a gahnitic

component of  $X_{\text{gahn}}$  (0.05 - 0.19) but only the hercynite and Mg-spinel endmember could be considered in the calculations. According to Tajčmanová et al., (2009) hercynite and Mg-spinel stabilize at higher temperatures thus the incorporation of ZnO in the KFMZnASH system expands the spinel stability field towards lower temperatures and higher pressures.

Peak temperature conditions were assumed by matching the stability field of the peak mineral assemblage and were further constrained by compositional  $X_{\text{prp}}$  and  $X_{\text{grs}}$  garnet isopleth intersections. The calculated field of the peak-metamorphic mineral assemblages are partly consistent with the GASP and multi-equilibrium barometer and deviate only minor from Ti-biotite and garnet cordierite thermometer. Garnet compositions are mostly homogeneous as shown in Figure 16, except retrograde diffusional zoning patterns in contact with e.g. biotite can be observed. Therefore, interpretations based on compositional isopleths of garnet are made with caution. Sillimanite inclusions in some garnet rims indicate growth within the stability of sillimanite and could represent the actual prograde mantle. Furthermore, missing preserved prograde zonation impedes the exact determination of a P-T path. The primarily pressure dependent reaction  $\text{Melt} + \text{Grt} + \text{Sil} + \text{Qtz} = \text{Crd} + \text{Sp} + \text{Bt}$  is documented in every sample indicating an isothermal decompression after peak-metamorphism, which is constant with previous work (e.g. Dharmapriya et al., 2014). P-T Pseudosections for S4, S5, S23 and SL8 covering the vast range of bulk rock chemistry are discussed in detail below. More detailed description of the samples in chapter 3 and 6.5.

Peak metamorphic temperatures  $>800^{\circ}\text{C}$  and clearly visible migmatitic structures in outcrops at meter scale or cm scale in hand specimens indicate supra solidus P-T conditions that could have led to melt extraction. Prograde heating or decompression are mainly responsible for melt production and the subsequent loss which effects the bulk chemistry (Whitney et al., 2004). While temperature is linear positive related to melt production independent of the bulk chemistry (Vielzeuf et al., 1988), the effect of pressure is more related to the bulk chemistry but still matter of discussion (Clemens et al., 1987). The measured WR chemistry represents the composition at peak metamorphic conditions, where melt has already been removed from the system. Melt re-integration after Korhonen et al. (2013)

was applied on several samples (e.g. S5, S23) but no further conclusions could be drawn with changing prograde topology. Anyway, given the peak P-T conditions melt extraction was likely.

## 8.2 P-T Pseudosections

### 8.2.1 Sample S4

For sample S4 (Figure 37), 15%  $\text{Fe}^{3+}/\text{Fe}_{\text{total}}$  and 0.6 wt%  $\text{H}_2\text{O}$  was assumed for initial calculations. A detailed sample description was made in chapter 6.5.1. Peak metamorphic conditions were estimated using the observed mineral assemblage as garnet inclusion, plagioclase + quartz + cordierite + biotite in the core and abundant sillimanite in the mantle. Measured  $X_{\text{prp}}$ ,  $X_{\text{alm}}$ , and  $X_{\text{grs}}$  compositions matched with modelled isopleths indicate lower pressures (5-6 kbar) and slightly higher temperatures (830 - 900 °C) in biotite absent stability field. It has to be mentioned that almost complete chemical re-equilibration of the garnet may have provoked an underestimation of P-T conditions and further constrains about prograde and retrograde history using garnet could not be made. The garnet breakdown reaction  $\text{Melt} + \text{Grt} + \text{Sil} + \text{Qtz} = \text{Crd} + \text{Bt} \pm \text{Sp}$  is well documented by petrographic observations. According to modelled isomodes, additional cordierite growths at the expense of garnet is achieved either by isothermal decompression or extensive isobaric heating.  $X_{\text{Mg}}$  of cordierite is between 0.69-0.76, exceeding the maximum of modelled isopleths. Melt inclusions in the garnet core indicate garnet growth during the presence of melt. Considering the GASP barometry (7.5 - 8.5 kbar) and the stability field of the observed mineral assemblage, peak metamorphic conditions of 7,5 kbar and 800°C are proposed for this sample.

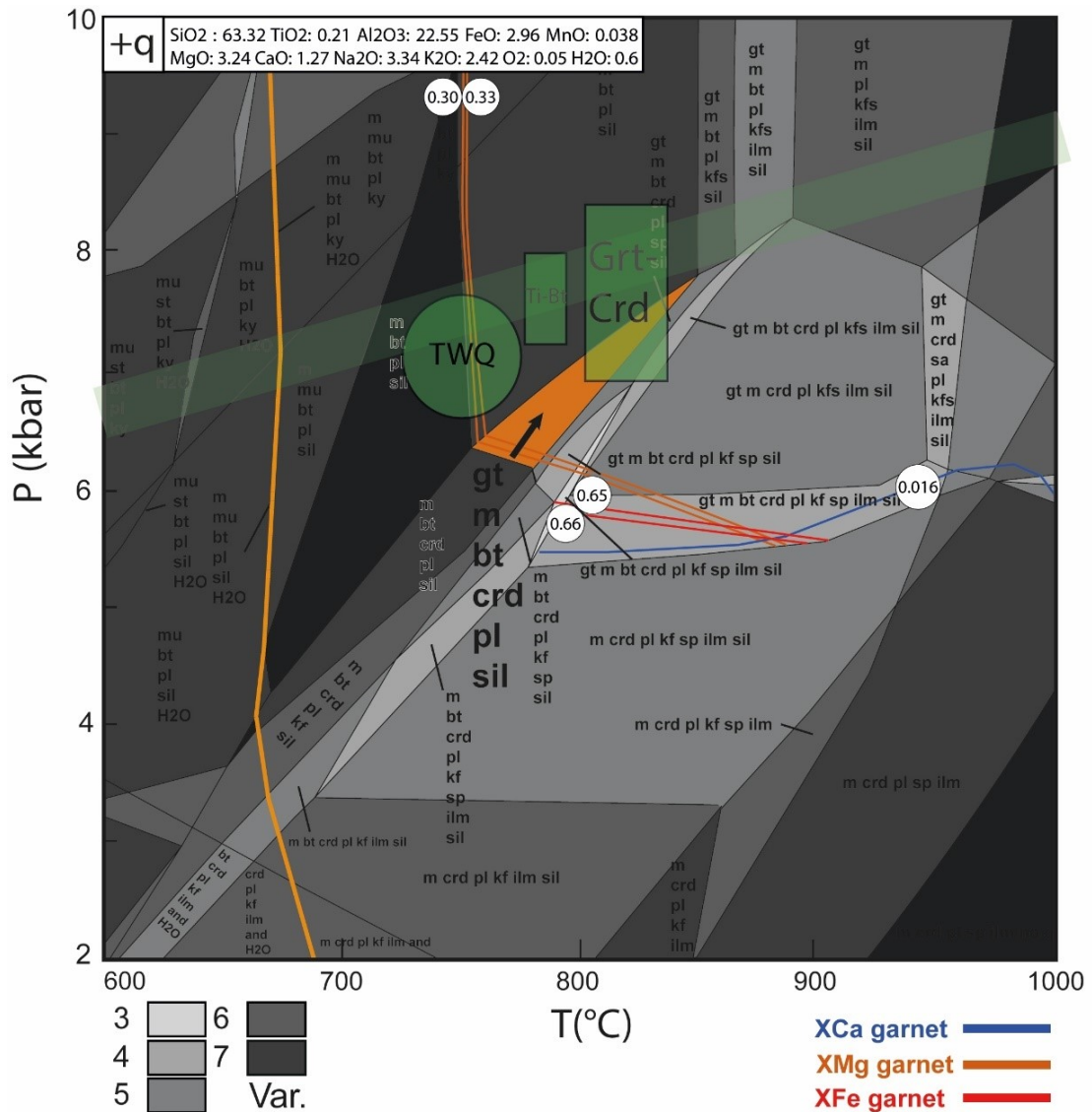


Figure 72: P-T Pseudosection for sample S4 calculated with 15% Fe<sup>3+</sup>/Fe<sub>total</sub> and 0.6 wt% H<sub>2</sub>O. Mineral assembly + Quartz. Variance coloured after legend. Orange dashed line = melt in. Coloured isopleths for X<sub>Ca</sub>, X<sub>Mg</sub> and X<sub>Fe</sub> of garnet with their respective composition for the endmembers X<sub>grs</sub>, X<sub>prp</sub> and X<sub>alm</sub>. Green dashed line = GASP Barometer (7.5-8.5 kbar). Green Boxes(circle): GTB results for the garnet cordierite (800-820 °C), Ti-in biotite (780-79 °C) and multi equilibrium thermometer/barometer (TWQ=7 kbar/750 °C). Orange stability field marks the peak mineral assemblage (bold). White dashed arrow = suggested P-T Path. Mineral abbreviations: gt=garnet m=melt bt=biotite crd=cordierite pl=plagioclase kf=k-feldspar ilm=ilmenite sp=spinel sil=sillimanite ky=kyanite and=andalusite st=staurolithe mu= muscovite.

### 8.2.2 Sample S5

For sample S5 (Figure 38), 0.8 wt% H<sub>2</sub>O and 15% Fe<sup>3+</sup>/Fe<sub>total</sub> was assumed for initial calculations. Peak P-T conditions were constrained by the stability field of the observed mineral assemblage garnet+biotite+cordierite+plagioclase+k-feldspar+ilmenite+magnetite+quartz (810-820°C, 5-6.5kbar). The results from conventional geothermometry are within the same range; the GASP barometer yields 4 – 6 kbar, Ti- in biotite and garnet cordierite thermometer 810 - 820 °C and 790 – 810 °C, respectively. The diffusional modifications in garnet and the uncertainty in the original chemical composition due to potential melt loss makes the application of calculated mineral composition for further constraining P-T conditions highly uncertain. Hence the garnet endmember isopleths ( $X_{\text{prp}} = 0.31 - 0.33$  and  $X_{\text{grs}} = 0.037 - 0.038$ ) intersect at lower T and slightly higher P while the calculated composition of cordierite does not match the observed ones. Abundant retrograde biotite and cordierite indicate an isothermal decompression after peak P-T conditions.

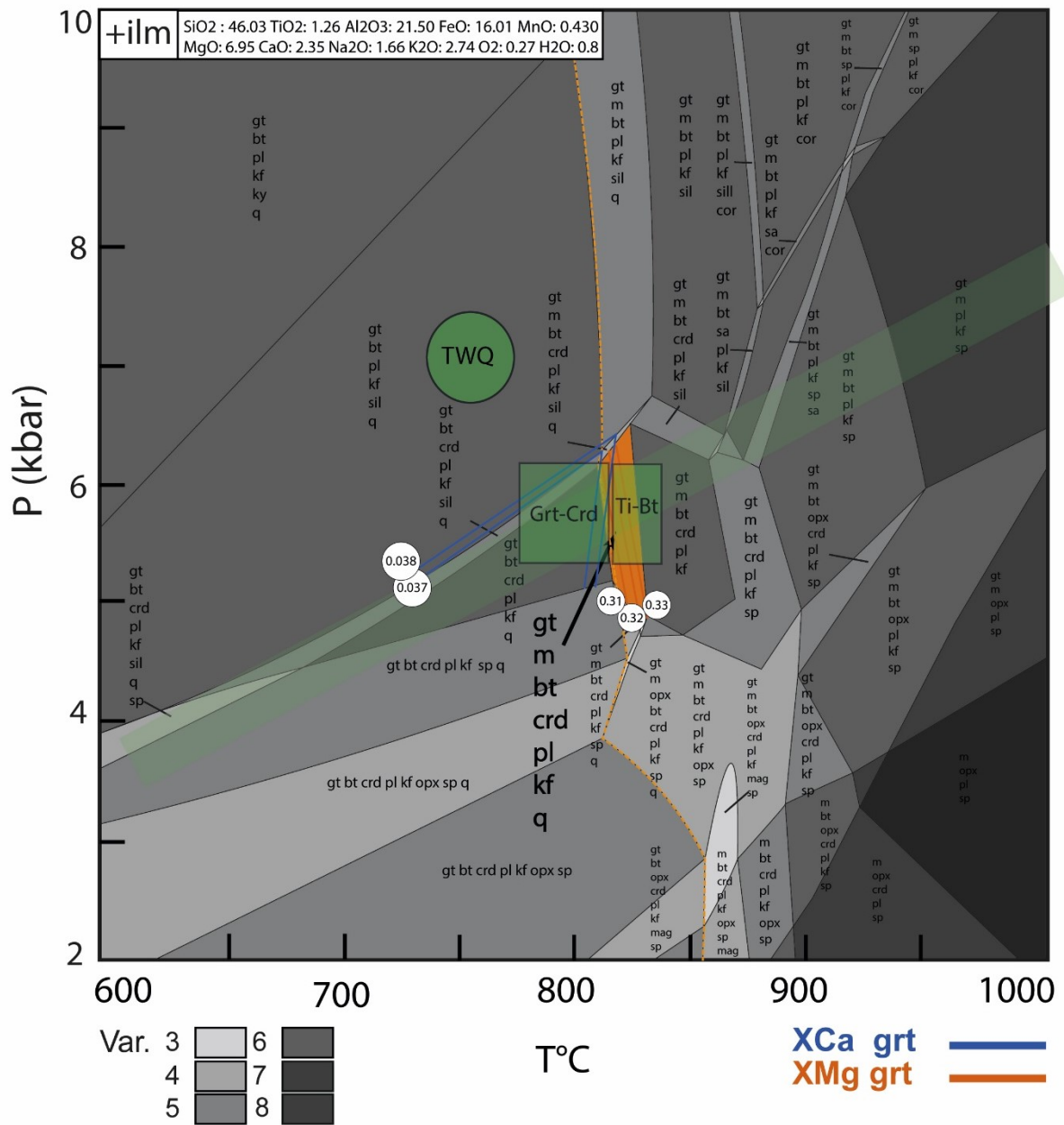


Figure 73: P-T Pseudosection for sample S5 assuming 0.8 wt% H<sub>2</sub>O and 15% Fe<sup>3+</sup>/Fe<sub>total</sub>. Mineral assembly + Ilmenite. Variance coloured after legend. Orange dashed line = melt in. Coloured isopleths for X<sub>Mg</sub> and X<sub>Ca</sub> garnet with their respective composition for the endmembers X<sub>prp</sub> and X<sub>grs</sub>. Green dashed line = GASP Barometer (4-6 kbar). Green Boxes/circle: GTB results for the garnet cordierite (790 - 810 °C), Ti-in biotite (810 - 820 °C) and multi equilibrium thermometer/barometer (TWQ = 7 kbar / 750 °C). Thick green transparent line = GASP barometer. Orange stability field marks the peak mineral assemblage (bold). Mineral abbreviations: gt=garnet m=melt bt=biotite crd=cordierite pl=plagioclase kf=k-feldspar ilm=ilmenite sp=spinel sil=sillimanite ky=kyanite and=andalusite st=staurolithe mu= muscovite.

### 8.2.3 Sample S23

For sample S23, 0.8 wt% H<sub>2</sub>O and 15% Fe<sup>3+</sup>/Fe<sub>total</sub> was assumed for P-T pseudosection calculation (Figure 39). Peak P-T conditions were constrained by the stability field of the peak mineral assemblage garnet+biotite+cordierite+plagioclase+k-feldspar+sillimanite+ilmenite+quartz+melt. Spinel and magnetite occurrence is related to garnet symplectites. Melt inclusions in the garnet core indicate garnet growth during the presence of melt. Sillimanite is present in the mantle or rim of the garnet. X<sub>grs</sub> (0.032 - 0.033) and X<sub>prp</sub> (0.24 - 0.28) garnet core isopleths intersect at 790 – 830 °C and 5-6 kbar. X<sub>an</sub> (0.36) of plagioclase coincide with the peak mineral assemblage stability field at 790-820 °C and 5.5 – 6.5 kbar. Measured X<sub>Mg</sub> of cordierite (0.77 - 0.82) exceeds the modelled maximum isopleths (0.68). Retrograde growth of cordierite by decompression is indicated by the reaction melt + Grt + Qtz + Sil = Crd + Bt ± Sp which matches with petrographic observations and modelled isomodes. The Ti in biotite thermometer yields 810-830°C for biotite as inclusion in garnet cores and 750 – 790 °C for matrix biotite. Due to the absence of graphite in sample S23 and retrograde diffusional Fe-Mg exchange of biotite, the temperatures may be underestimated (Henry et al., 2005). Multi equilibrium thermobarometry (TWQ) yields higher pressures and lower temperatures with 7.5 kbar and 750 °C, respectively. The garnet-cordierite thermometer yields significant lower temperatures (700 – 750 °C). The GASP barometer yields 5-6kbar, which is in agreement with constraints from mineral isopleths and peak mineral assemblage. Peak P-T conditions are estimated at 5-6 kbar and 800 - 820°C. First melt occurs at ~680 °C between 5 – 6 kbar. The retrograde growth of cordierite and biotite at the expense of garnet and sillimanite and the actual absence of sillimanite in the matrix suggests decompression and cooling after peak metamorphism. (Hiroi et al., 1994) suggested a similar P-T path for cordierite bearing gneisses from a near location of sample S4.

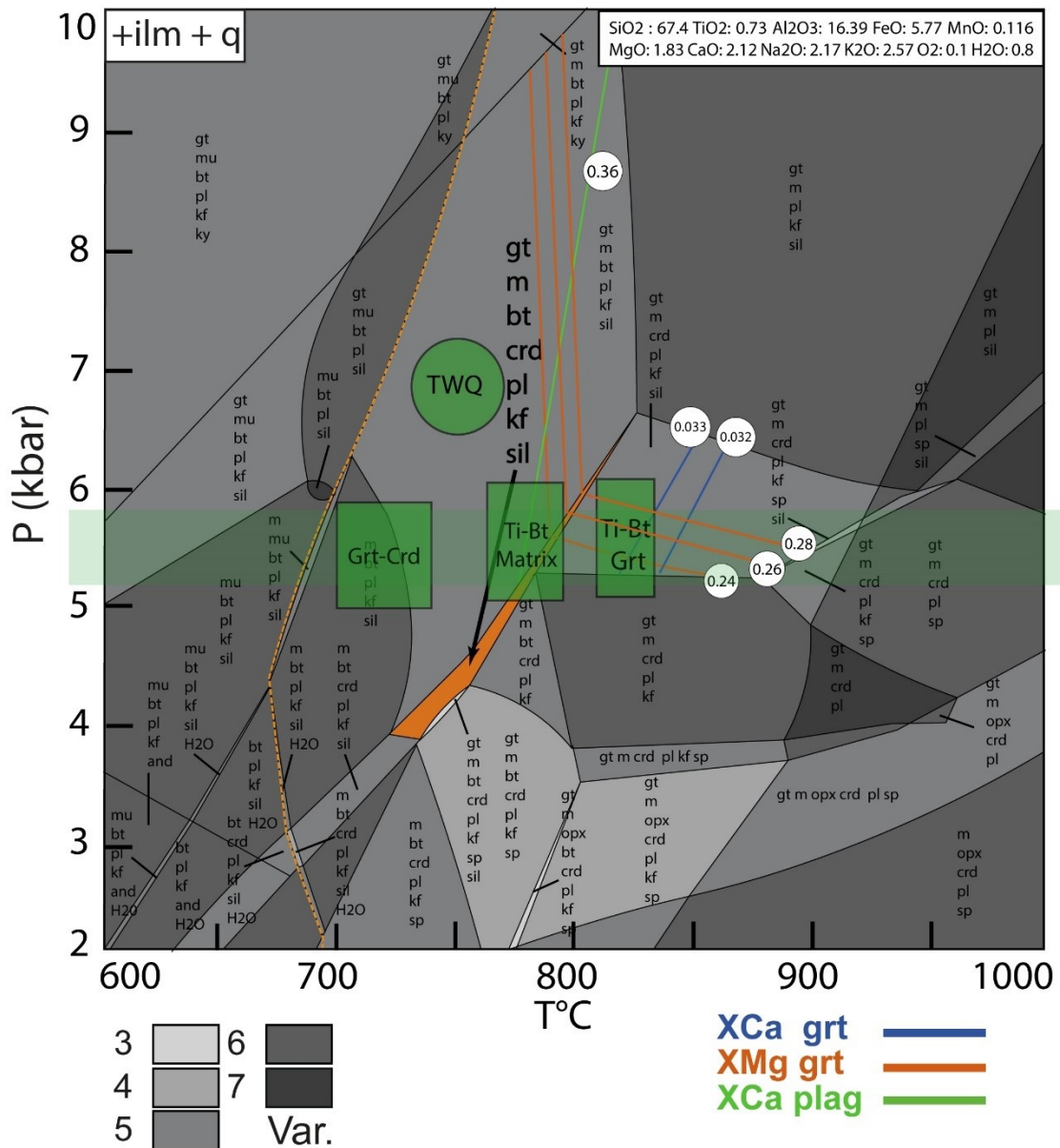


Figure 74 A : P-T Pseudosection for sample S23 assuming 0.8 wt% H<sub>2</sub>O and 15% Fe<sup>3+</sup>/Fe<sub>total</sub>. Bulk chemistry is given in wt%. all mineral assemblys + quartz and + ilmenite. Variance coloured after legend. Orange dashed line = melt in. Coloured isopleths for XMg and XCa garnet and X<sub>Ca</sub> plagioclase with their respective composition. Thick green transparent line = GASP Barometer (5-6 kbar). Green boxes/circle: GTB results for the garnet cordierite (690-710 °C), multi equilibrium thermometer/barometer (TWQ=7 kbar/750 °C) and Ti-in biotite (~780 °C for matrix biotite and ~810 °C as inclusion in garnet). S23 is the only sample with a significant T discrepancy for biotite as inclusion in garnet or in the matrix. Orange stability field marks the peak mineral assemblage (bold). Mineral abbreviations: gt=garnet m=melt bt=biotite crd=cordierite pl=plagioclase kf=k-feldspar ilm=ilmenite sp=spinel sil=sillimanite ky=kyanite and=andalusite st=staurolithe mu= muscovite.

#### 8.2.4 Sample SL8

For sample SL8 (Figure 40), 15%  $\text{Fe}^{3+}/\text{Fe}_{\text{total}}$  and 0.8 wt%  $\text{H}_2\text{O}$  was assumed for initial calculations. A detailed sample description was made in chapter 6.5.6. Peak metamorphic conditions were estimated using the peak mineral assemblage garnet + plagioclase + quartz + cordierite + biotite + k-feldspar + sillimanite + quartz + ilmenite defining a peak P-T field of 790 – 820 °C and 5.5 - 6.5 kbar. The Ti in biotite thermometer and GASP barometer yield consistent results with 790-800°C and 5-6kbar, respectively. The garnet – cordierite thermometer yields significant higher temperatures (890-900°C). Melt inclusions, biotite, plagioclase, sillimanite and quartz occur as inclusion in garnet although sillimanite is restricted to the garnet outer mantle or rim.  $X_{\text{grs}}$ ,  $X_{\text{prp}}$  and  $X_{\text{alm}}$  isopleths of garnet intersect in the small stability field of the peak mineral assemblage, shown in Figure 40. The garnet-cordierite thermometer yields significant higher temperatures up to 900°C and also the TWQ multi-equilibrium thermometry indicates higher temperatures. Like the other samples, SL8 shows petrographical evidence for extensive garnet breakdown and retrograde biotite, cordierite and magnetite growth suggesting isothermal decompression after peak P-T conditions.

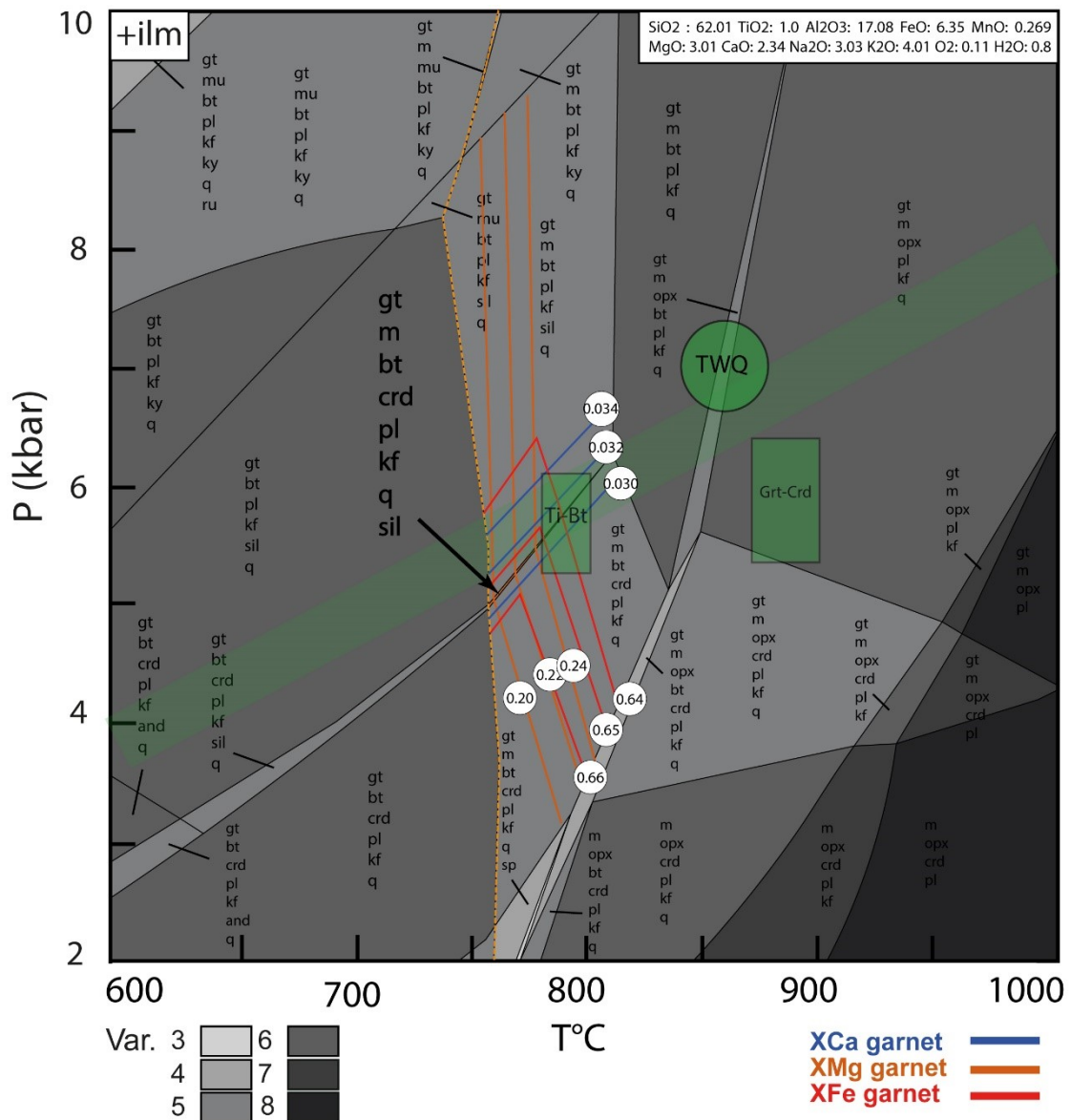


Figure 75: P-T Pseudosection for sample SL8 assuming 0.8 wt% H<sub>2</sub>O and 15% Fe<sup>3+</sup>/Fe<sub>total</sub>. Mineral assembly + Ilmenite. Variance coloured after legend. Coloured isopleths for X<sub>Ca</sub>, X<sub>Mg</sub> and X<sub>Fe</sub> of garnet with their respective composition. Orange dashed line = melt in. Green boxes(circle): GTB results for the garnet cordierite (890-900 °C), Ti-in biotite (790-800 °C) and multi equilibrium thermometer/barometer (TWQ=7 kbar / 800 °C). Thick green transparent line = GASP Barometer (5-6 kbar). orange stability field marks the peak mineral assemblage (bold). Mineral abbreviations: gt=garnet m=melt bt=biotite crd=cordierite pl=plagioclase kf=k-feldspar ilm=ilmenite sp=spinel sil=sillimanite ky=kyanite and=andalusite st=staurolite mu= muscovite.

## 9. Discussion

Cordierite bearing gneisses represent a minor, meta-sedimentary rock-type in the Wannu Complex and is only found in southwestern Sri Lanka along the assumed WC/HC boundary area (Figure 6). Cordierite is only observed in this meta-sedimentary migmatitic gneisses with the mineral assemblage garnet + biotite + cordierite + plagioclase + k-feldspar + quartz + magnetite + spinel + ilmenite + sillimanite. P-T conditions of this cordierite bearing gneisses were constrained with  $850 \pm 50^\circ\text{C}$  at  $6 \pm 1$  kbar and are in agreement with previous P-T estimations in the southwestern WC of 7.5 - 8.5 kbar and  $870 - 900^\circ\text{C}$  (Dharmapriya et al., 2014) and 5 -7 bar and  $650 - 850^\circ\text{C}$  (Hiroi et al., 1994). Monazites in garnets yield with  $572 \pm 3$  Ma clearly older ages than the younger monazites in the matrix ( $534 \pm 2$  Ma). The older age cluster for monazites in the matrix of  $565 \pm 3$  Ma is close to the age of the monazites enclosed in garnet. Based on monazite inclusions in garnet a polymetamorphic history is envisaged. We assume simultaneous monazite and garnet growth at a first metamorphic phase at  $\sim 570$  Ma which is constrained by the weighted mean of monazite inclusions in garnet and the older age group in the matrix. The formation of cordierite at the expense of garnet, which is documented by petrographic observations in almost all samples indicates isothermal decompression after the first long lasting metamorphic event. Dharmapriya et al., (2015) also suggested isothermal decompression preceded by isobaric cooling. The decompressive breakdown of garnet is accompanied by new monazite growth (or overgrowth of existing matrix monazite) which is indicated by the weighted mean ages from the matrix monazites, displaying an age of  $534 \pm 2$  Ma. Similar U-Pb ages were described by Sajeev et al. (2010) at zircon and monazites rims interpreted as metamorphic overgrowth from UHT granulites ( $1050^\circ\text{C}$ , 9 kbar) located in the central highland complex near the WC/HC boundary. Two generations were distinguished, at  $569 \pm 5$  and  $551 \pm 7$  Ma for zircons and  $547 \pm 7$  Ma for monazites. The metamorphic event around  $551 \pm 7$  Ma as defined by Sajeev et al. (2010) may be hidden in our data, but no clear metamorphic texture is related to this event. In contrast to the HC rocks where no metamorphic event  $< 550$  Ma is documented, the cordierite bearing gneisses from the

southwestern WC experienced extensive migmatitization and cordierite crystallization due LP/HT final metamorphic overprint. Although the retrograde evolution is supported by petrographic textures no reliable information is preserved about the prograde evolution. Garnets are well equilibrated, showing only retrograde diffusional zoning, which contributes to the deviation of modelled endmember isopleths from actual observations. REE patterns indicate a core, mantle and rim section in garnets, and preserved weak zoning of Y and P can be observed (Figure 14 and Figure 15). Further research has to be done to relate these preserved element patterns with garnet inclusions and phosphate growth (monazite, apatite, xenotime etc...) to get more information about the prograde history of these rock types.

Although other authors already described the P-T conditions and age of cordierite metamorphism, we are the first to clearly demonstrate that this unit experienced a metamorphic overprint contemporaneously with the HC complex at 570 Ma. Although temperatures of up to ~950 °C are reported in the WC/HC boundary area, it is still unclear if the cordierite bearing unit underwent the same UHT conditions like the HC or “only” HT conditions. The (U)HT garnet bearing mineral assemblage garnet – sillimanite – biotite - ternary feldspar – ilmenite ± orthopyroxene ± spinel was replaced by a decompressional isothermal event at ~ 530 Ma leading to the mineral assemblage cordierite - biotite – magnetite/spinel – ilmenite - k-feldspar – plagioclase ± garnet.

## 10. References

- Baur, N., Kroner, A., Liew, T. C., Todt, W., Williams, I. S., & Hofmann, A. W. (1991). U-Pb isotopic systematics of zircons from prograde and retrograde transition zones in high-grade orthogneisses, Sri Lanka. *Journal of Geology*. <https://doi.org/10.1086/629515>
- Bea, F., & Montero, P. (1999). Behavior of accessory phases and redistribution of Zr, REE, Y, Th, and U during metamorphism and partial melting of metapelites in the lower crust: An example from the Kinzigite Formation of Ivrea-Verbano, NW Italy. *Geochimica et Cosmochimica Acta*. [https://doi.org/10.1016/S0016-7037\(98\)00292-0](https://doi.org/10.1016/S0016-7037(98)00292-0)
- Benisek, A., Kroll, H., & Cemič, L. (2004). New developments in two-feldspar thermometry. *American Mineralogist*. <https://doi.org/10.2138/am-2004-1018>
- Berman, R. G., & Aranovich, L. Y. (1996). Optimized standard state and solution properties of minerals. *Contributions to Mineralogy and Petrology*. <https://doi.org/10.1007/s004100050232>
- Berman, Robert G. (1991). Thermobarometry Using Multi-Equilibrium Calculations: a New Technique, With Petrological Applications. *Canadian Mineralogist Vol.*
- Braun, I., & Kriegsman, L. M. (2003). Proterozoic crustal evolution of southernmost India and Sri Lanka. *Geological Society, London, Special Publications*, 206(1), 169–202. <https://doi.org/10.1144/GSL.SP.2003.206.01.10>
- Burton, K. W., & O'Nions, R. K. (1990). The timescale and mechanism of granulite formation at Kurunegala, Sri Lanka. *Contributions to Mineralogy and Petrology*, 106(1), 66–89. <https://doi.org/10.1007/BF00306409>
- Cherniak, D. J., Watson, E. B., Grove, M., & Harrison, T. M. (2004). Pb diffusion in monazite: A combined RBS/SIMS study. *Geochimica et Cosmochimica*

- Acta*. <https://doi.org/10.1016/j.gca.2003.07.012>
- Clemens, J. D., & Vielzeuf, D. (1987). Constraints on melting and magma production in the crust. *Earth and Planetary Science Letters*. [https://doi.org/10.1016/0012-821X\(87\)90227-5](https://doi.org/10.1016/0012-821X(87)90227-5)
- Collins, A. S., & Pisarevsky, S. A. (2005). Amalgamating eastern Gondwana: The evolution of the Circum-Indian Orogens. *Earth-Science Reviews*. <https://doi.org/10.1016/j.earscirev.2005.02.004>
- Cooray, P. G. (1994). The precambrian of Sri Lanka: a historical review. *Precambrian Research*, 66(1–4), 3–18. [https://doi.org/10.1016/0301-9268\(94\)90041-8](https://doi.org/10.1016/0301-9268(94)90041-8)
- Dachs, E. (1998). Petrological Elementary Tools (PET). *Computers & Geosciences*, 24(3), 219–235. [http://www.unisalzburg.at/portal/page?\\_pageid=805,259394&\\_dad=portal&\\_schema=PORTAL](http://www.unisalzburg.at/portal/page?_pageid=805,259394&_dad=portal&_schema=PORTAL)
- Deer, W. A., Howie, R. A., & Zussman, J. (1992). An introduction to the rock-forming minerals. Second edition. *An Introduction to the Rock-Forming Minerals. Second Edition*.
- Dharmapriya, P. L., Malaviarachchi, S. P. K., Galli, A., Su, B. X., Subasinghe, N. D., Dissanayake, C. B., Nimalsiri, T. B., & Zhu, B. (2014). P-T evolution of a spinel+quartz bearing khondalite from the Highland Complex, Sri Lanka: Implications for non-UHT metamorphism. *Journal of Asian Earth Sciences*. <https://doi.org/10.1016/j.jseaes.2014.05.003>
- Dharmapriya, P. L., Malaviarachchi, S. P. K., Santosh, M., Tang, L., & Sajeev, K. (2015). Late-Neoproterozoic ultrahigh-temperature metamorphism in the Highland Complex, Sri Lanka. *Precambrian Research*, 271, 311–333. <https://doi.org/10.1016/j.precamres.2015.10.010>
- Fritz, H., Abdelsalam, M., Ali, K. A., Bingen, B., Collins, A. S., Fowler, A. R., Ghebreab, W., Hauzenberger, C. A., Johnson, P. R., Kusky, T. M., Macey, P., Muhongo, S., Stern, R. J., & Viola, G. (2013). Orogen styles in the East

- African Orogen: A review of the Neoproterozoic to Cambrian tectonic evolution. In *Journal of African Earth Sciences*.  
<https://doi.org/10.1016/j.jafrearsci.2013.06.004>
- Fuhrman, M. L., & Lindsley, D. H. (1988). Ternary-feldspar modeling and thermometry. *American Mineralogist*.
- Grove, M., & Harrison, T. M. (1999). Monazite Th-Pb age depth profiling. *Geology*. [https://doi.org/10.1130/0091-7613\(1999\)027<0487:MTPADP>2.3.CO;2](https://doi.org/10.1130/0091-7613(1999)027<0487:MTPADP>2.3.CO;2)
- He, X. F., Santosh, M., Tsunogae, T., & Malaviarachchi, S. P. K. (2016). Early to late Neoproterozoic magmatism and magma mixing-mingling in Sri Lanka: Implications for convergent margin processes during Gondwana assembly. *Gondwana Research*, 32(29), 151–180.  
<https://doi.org/10.1016/j.gr.2015.02.013>
- He, X. F., Santosh, M., Tsunogae, T., Malaviarachchi, S. P. K., & Dharmapriya, P. L. (2016). Neoproterozoic arc accretion along the “eastern suture” in Sri Lanka during Gondwana assembly. *Precambrian Research*, 279, 57–80.  
<https://doi.org/10.1016/j.precamres.2016.04.006>
- Henry, D. J., Guidotti, C. V., & Thomson, J. A. (2005). The Ti-saturation surface for low-to-medium pressure metapelitic biotites: Implications for geothermometry and Ti-substitution mechanisms. *American Mineralogist*.  
<https://doi.org/10.2138/am.2005.1498>
- Hermann, R. G., Buick, I. A. N. S., & Rubatto, D. (2006). *Temperature and Bulk Composition Control on the Growth of Monazite and Zircon During Low-pressure Anatexis (Mount Stafford, Central Australia)*. 47(10), 1973–1996.  
<https://doi.org/10.1093/petrology/egl033>
- Hiroi, Y., Ogo, Y., & Namba, K. (1994). Evidence for prograde metamorphic evolution of Sri Lankan pelitic granulites, and implications for the development of continental crust. *Precambrian Research*, 66(1–4), 245–263.  
[https://doi.org/10.1016/0301-9268\(94\)90053-1](https://doi.org/10.1016/0301-9268(94)90053-1)

- HOLLAND, T. (2001). Calculation of Phase Relations Involving Haplogranitic Melts Using an Internally Consistent Thermodynamic Dataset. *Journal of Petrology*. <https://doi.org/10.1093/petrology/42.4.673>
- Holland, T. J. B., & Powell, R. (2011). An improved and extended internally consistent thermodynamic dataset for phases of petrological interest, involving a new equation of state for solids. *Journal of Metamorphic Geology*. <https://doi.org/10.1111/j.1525-1314.2010.00923.x>
- Holland, T., & Powell, R. (2003). Activity-compositions relations for phases in petrological calculations: An asymmetric multicomponent formulation. *Contributions to Mineralogy and Petrology*. <https://doi.org/10.1007/s00410-003-0464-z>
- Hölzl, S., Hofmann, A. W., Todt, W., & Köhler, H. (1994). UPb geochronology of the Sri Lankan basement. *Precambrian Research*, 66(1–4), 123–149. [https://doi.org/10.1016/0301-9268\(94\)90048-5](https://doi.org/10.1016/0301-9268(94)90048-5)
- Ikeda, T. (1998). Progressive sequence of reactions of the Ryoke metamorphism in the Yanai district, southwest Japan: The formation of cordierite. *Journal of Metamorphic Geology*. <https://doi.org/10.1111/j.1525-1314.1998.00060.x>
- JAROSEWICH, E., NELEN, J. A., & NORBERG, J. A. (1980). Reference Samples for Electron Microprobe Analysis. *Geostandards Newsletter*. <https://doi.org/10.1111/j.1751-908X.1980.tb00273.x>
- Kehelpannala, K. V. W., & Ratnayake, N. P. (1999). Evidence for Post-Metamorphic Metasomatism of High-Grade Orthogneisses from Sri Lanka. *Gondwana Research*. [https://doi.org/10.1016/S1342-937X\(05\)70141-6](https://doi.org/10.1016/S1342-937X(05)70141-6)
- Kehelpannala, K. V. W. V. W. (2016). Structural evolution of the middle to lower crust in Sri Lanka—a review. *Journal of Geological Society of Sri Lanka*, 11(January 2003), 45–85.
- Kelsey, D. E., White, R. W., Holland, T. J. B., & Powell, R. (2004). Calculated phase equilibria in. *Journal of Metamorphic Geology*, 22(6), 559–578. <https://doi.org/10.1111/j.1525-1314.2004.00533.x>

- Kitano, I., Osanai, Y., Nakano, N., Adachi, T., & Fitzsimons, I. C. W. (2018). Detrital zircon and igneous protolith ages of high-grade metamorphic rocks in the Highland and Wannai Complexes, Sri Lanka: Their geochronological correlation with southern India and East Antarctica. *Journal of Asian Earth Sciences*, 156(February), 122–144. <https://doi.org/10.1016/j.jseaes.2018.01.017>
- Kleinschrodt, R. (1994). Large-scale thrusting in the lower crustal basement of Sri Lanka. *Precambrian Research*, 66(1–4), 39–57. [https://doi.org/10.1016/0301-9268\(94\)90043-4](https://doi.org/10.1016/0301-9268(94)90043-4)
- Kleinschrodt, R., Voll, G., & Kehelpannala, W. (1991). A layered basic intrusion, deformed and metamorphosed in granulite facies of the Sri Lanka basement. *Geologische Rundschau*. <https://doi.org/10.1007/BF01803701>
- Korhonen, F. J., Brown, M., Clark, C., & Bhattacharya, S. (2013). Osumilite-melt interactions in ultrahigh temperature granulites: Phase equilibria modelling and implications for the P-T-t evolution of the eastern ghats province, India. *Journal of Metamorphic Geology*, 31(8), 881–907. <https://doi.org/10.1111/jmg.12049>
- Koziol, A. M., & Newton, R. C. (1988). Redetermination of the anorthite breakdown reaction and improvement of the plagioclase-garnet-Al<sub>2</sub>SiO<sub>5</sub>-quartz geobarometer [Erratum to document cited in CA108(16):135085a]. *Am. Mineral.*
- Kriegsman, L. M. (1994). Evidence for a fold nappe in the high-grade basement of central Sri Lanka: terrane assembly in the pan-african lower crust? *Precambrian Research*, 66(1–4), 59–76. [https://doi.org/10.1016/0301-9268\(94\)90044-2](https://doi.org/10.1016/0301-9268(94)90044-2)
- Kriegsman, L. M. (1995). The Pan-African event in East Antarctica: a view from Sri Lanka and the Mozambique Belt. *Precambrian Research*, 75(3–4), 263–277. [https://doi.org/10.1016/0301-9268\(95\)80010-F](https://doi.org/10.1016/0301-9268(95)80010-F)
- Kröner, A., Kehelpannala, K. V. W., & Hegner, E. (2003). Ca. 750-1100 Ma

- magmatic events and Grenville-age deformation in Sri Lanka: Relevance for Rodinia supercontinent formation and dispersal, and Gondwana amalgamation. *Journal of Asian Earth Sciences*.  
[https://doi.org/10.1016/S1367-9120\(03\)00060-9](https://doi.org/10.1016/S1367-9120(03)00060-9)
- Kröner, A., Kehelpannala, K. V. W. W., & Kriegsman, L. M. (1994). Origin of compositional layering and mechanism of crustal thickening in the high-grade gneiss terrain of Sri Lanka. *Precambrian Research*, 66(1–4), 21–37.  
[https://doi.org/10.1016/0301-9268\(94\)90042-6](https://doi.org/10.1016/0301-9268(94)90042-6)
- Kröner, A., Rojas-Agramonte, Y., Kehelpannala, K. V. W., Zack, T., Hegner, E., Geng, H. Y., Wong, J., & Barth, M. (2013). Age, Nd-Hf isotopes, and geochemistry of the Vijayan Complex of eastern and southern Sri Lanka: A Grenville-age magmatic arc of unknown derivation. *Precambrian Research*, 234, 288–321. <https://doi.org/10.1016/j.precamres.2012.11.001>
- Kroner, A., & Williams, I. S. (1993). Age of Metamorphism in the High-Grade Rocks of Sri Lanka. *The Journal of Geology*, 101(4), 513–521.  
<https://doi.org/10.1086/648243>
- Kröner, A., Williams, I. S., Compston, W., Baur, N., Vitanage, P. W., Perera, L. R. K., & A. KRONER, I. S. WILLIAMS, W. COMPSTON, N. BAUR, P. W. VITANAGE, L. R. K. P. (1987). Zircon Ion Microprobe Dating of High-Grade Rocks in Sri Lanka. *The Journal of Geology*, 95(6), 775–791.  
<https://doi.org/10.1098/ROYAL/>
- Liew, T. C., Milisenda, C. C., & Hofmann, A. W. (1994). Pb isotopic discrimination of crustal domains within the highgrade basement of Sri Lanka. *Precambrian Research*, 66(1–4), 111–121. [https://doi.org/10.1016/0301-9268\(94\)90047-7](https://doi.org/10.1016/0301-9268(94)90047-7)
- Malaviarachchi, S. P. K., & Takasu, A. (2011). Electron microprobe dating of Monazites from Sri Lanka : implications on multiple thermal events related to Gondwana. *Journal of the Geological Society of Sri Lanka*, 14(July), 81–90.  
<https://doi.org/10.13140/2.1.3994.4648>

- Mathavan, V., Prame, W. K. B. N. B. N., & Cooray, P. G. (1999). Geology of the High Grade Proterozoic Terrains of Sri Lanka and the Assembly of Gondwana: An Update on Recent Developments. *Gondwana Research*, 2(2), 237–250. [https://doi.org/10.1016/S1342-937X\(05\)70148-9](https://doi.org/10.1016/S1342-937X(05)70148-9)
- Milisenda, C. C., Liew, T. C., Hofman, A. W., & Kroner, A. (1988). Isotopic Mapping of Age Provinces in Precambrian High-Grade Terrains : Sri Lanka. *The Journal of Geology*, 96(5), 608–615. <https://doi.org/10.1086/629256>
- Milisenda, C. C., Liew, T. C., Hofmann, A. W., & Köhler, H. (1994). Nd isotopic mapping of the Sri Lanka basement: update, and additional constraints from Sr isotopes. *Precambrian Research*, 66(1–4), 95–110. [https://doi.org/10.1016/0301-9268\(94\)90046-9](https://doi.org/10.1016/0301-9268(94)90046-9)
- Montel, J. M., Foret, S., Veschambre, M., Nicollet, C., & Provost, A. (1996). Electron microprobe dating of monazite. *Chemical Geology*, 131(1–4), 37–53. [https://doi.org/10.1016/0009-2541\(96\)00024-1](https://doi.org/10.1016/0009-2541(96)00024-1)
- N. Baur, A. Kröner, T. C. Liew, W. Todt, I. S. W. and A. W. H. (1991). U-Pb Isotopic Systematics of Zircons from Prograde and Retrograde Transition Zones in High-Grade Orthogneisses, Sri Lanka. *The Journal of Geology*, 99(4), 527–545.
- Osanai, Y., Sajeev, K., Owada, M., Kehelpannala, K. V. W., Prame, W. K. B., Nakano, N., & Jayatileke, S. (2006). Metamorphic evolution of high-pressure and ultrahigh-temperature granulites from the Highland Complex, Sri Lanka. *Journal of Asian Earth Sciences*, 28(1), 20–37. <https://doi.org/10.1016/j.jseaes.2004.09.013>
- Parrish, R. R. (1990). U-Pb dating of monazite and its application to geological problems. *Canadian Journal of Earth Sciences*. <https://doi.org/10.1139/e90-152>
- Petschnig, P. (2015). *Petrology of Granulite Facies Rocks from Sri Lanka by December*.
- Pohl, J. R., & Emmermann, R. (1991). Chemical composition of the Sri Lankan

- Precambrian basement. *The Crystalline Crust of Sri Lanka, Part, 1*, 94–124.
- Pyle, J. M., Spear, F. S., Rudnick, R. L., & McDonough, W. F. (2001). *Monazite – Xenotime – Garnet Equilibrium in Metapelites and a New Monazite – Garnet Thermometer*. *42*(11), 2083–2107.
- Raase, P., & Schenk, V. (1994). Petrology of granulite-facies metapelites of the Highland Complex, Sri Lanka: implications for the metamorphic zonation and the P-T path. *Precambrian Research*, *66*(1–4), 265–294. [https://doi.org/10.1016/0301-9268\(94\)90054-X](https://doi.org/10.1016/0301-9268(94)90054-X)
- Sajeev, K., & Osanai, Y. (2004). Ultrahigh-temperature metamorphism (1150°C, 12 kbar) and multistage evolution of Mg-, Al-rich granulites from the central Highland Complex, Sri Lanka. *Journal of Petrology*, *45*(9), 1821–1844. <https://doi.org/10.1093/petrology/egh035>
- SAJEEV, K., & Osanai, Y. (2004). Osumilite and spinel+quartz from Sri Lanka: Implications for UHT conditions and retrograde P-T path. *Journal of Mineralogical and Petrological Sciences*, *99*(5), 320–327. <https://doi.org/10.2465/jmps.99.320>
- Sajeev, K., Osanai, Y., Connolly, J. A. D. A. D., Suzuki, S., Ishioka, J., Kagami, H., & Rino, S. (2007). Extreme Crustal Metamorphism during a Neoproterozoic Event in Sri Lanka: A Study of Dry Mafic Granulites. *The Journal of Geology*, *115*(5), 563–582. <https://doi.org/10.1086/519778>
- Sajeev, K., Williams, I. S., & Osanai, Y. (2010). Sensitive high-resolution ion microprobe U-Pb dating of prograde and retrograde ultrahigh-temperature metamorphism as exemplified by Sri Lankan granulites. *Geology*, *38*(11), 971–974. <https://doi.org/10.1130/G31251.1>
- Santosh, M., Tsunogae, T., Malaviarachchi, S. P. K., Zhang, Z., Ding, H., Tang, L., & Dharmapriya, P. L. (2014). Neoproterozoic crustal evolution in Sri Lanka: Insights from petrologic, geochemical and zircon U-Pb and Lu-Hf isotopic data and implications for Gondwana assembly. *Precambrian Research*, *255*(P1), 1–29. <https://doi.org/10.1016/j.precamres.2014.09.017>

- Steward, D. B., Walker, G. W., Wright, T. L., & Fahey, J. J. (1966). Physical Properties of calcic Labradorite from Lake County, Oregon. *American Mineralogist*, 51, 177–197.
- Tajčmanová, L., Konopásek, J., & Košler, J. (2009). Distribution of zinc and its role in the stabilization of spinel in high-grade felsic rocks of the Moldanubian domain (Bohemian Massif). *European Journal of Mineralogy*. <https://doi.org/10.1127/0935-1221/2009/0021-1899>
- Vermeesch, P. (2018). IsoplotR: A free and open toolbox for geochronology. *Geoscience Frontiers*, 9(5), 1479–1493. <https://doi.org/10.1016/j.gsf.2018.04.001>
- Vielzeuf, D., & Holloway, J. R. (1988). Experimental determination of the fluid-absent melting relations in the pelitic system. *Contributions to Mineralogy and Petrology*. <https://doi.org/10.1007/bf00375178>
- Wanniarachchi, D. N. S., & Akasaka, M. (2016). Internal texture and U–Th–total Pb isochron ages of monazite in metamorphic rocks from the Southwestern Highland Complex, Sri Lanka. *Journal of Mineralogical and Petrological Sciences*, 111(5), 351–362. <https://doi.org/10.2465/jmps.160121>
- White, R. W., Powell, R., & Clarke, G. L. (2002). The interpretation of reaction textures in Fe-rich metapelitic granulites of the Musgrave Block, Central Australia: Constraints from mineral equilibria calculations in the system. *Journal of Metamorphic Geology*, 20(1), 41–55. <https://doi.org/10.1046/j.0263-4929.2001.00349.x>
- White, R. W., Powell, R., Holland, T. J. B., Johnson, T. E., & Green, E. C. R. (2014a). New mineral activity-composition relations for thermodynamic calculations in metapelitic systems. *Journal of Metamorphic Geology*, 32(3), 261–286. <https://doi.org/10.1111/jmg.12071>
- White, R. W., Powell, R., Holland, T. J. B., Johnson, T. E., & Green, E. C. R. (2014b). New mineral activity-composition relations for thermodynamic calculations in metapelitic systems. *Journal of Metamorphic Geology*.

---

<https://doi.org/10.1111/jmg.12071>

- Whitney, D. L., Teyssier, C., & Fayon, A. K. (2004). Isothermal decompression, partial melting and exhumation of deep continental crust. *Geological Society Special Publication*. <https://doi.org/10.1144/GSL.SP.2004.227.01.16>
- Wilbert Kehelpanala, K. V. (1997). Deformation of a High-Grade Gondwana Fragment, Sri Lanka. *Gondwana Research*. [https://doi.org/10.1016/s1342-937x\(05\)70005-8](https://doi.org/10.1016/s1342-937x(05)70005-8)
- Williams, M. L., Jercinovic, M. J., & Hetherington, C. J. (2007). *Microprobe Monazite Geochronology: Understanding Geologic Processes by Integrating Composition and Chronology*. <https://doi.org/10.1146/annurev.earth.35.031306.140228>
- Young, E. J., Myers, A. T., Munson, E. L., & Conklin, N. M. (1969). Mineralogy and geochemistry of fluoapatite from Cerro de Mercado, Durango, Mexico. *Geological Survey Research 1969 - Professional Paper 650*.